ALMA MATER STUDIORUM
UNIVERSITÀ DI BOLOGNA

DOTTORATO DI RICERCA IN

SCIENZE E TECNOLOGIE DELLA SALUTE

Ciclo 36

**Settore Concorsuale:** 09/C2 - FISICA TECNICA E INGEGNERIA NUCLEARE

**Settore Scientifico Disciplinare:** ING-IND/11 - FISICA TECNICA AMBIENTALE

# APPLICATION OF ACOUSTIC METAMATERIALS IN BIOMEDICAL AND AUDIO FIELDS

**Presentata da:** Matteo Cingolani

**Coordinatore Dottorato**

Igor Diemberger

**Supervisore**

Massimo Garai

**Co-supervisore**

Claudio Borghi

Esame finale anno 2024

# Abstract

In recent decades, noise has become increasingly present in people's daily lives. The effects of noise have taken center stage in discussions, and progressively stringent regulations seek to limit people's exposure to high noise levels. Acoustic absorption is a fundamental concept when addressing noise control and is defined as the dissipation of acoustic energy associated with an emission. Nowadays, the most commonly used sound-absorbing materials are fibrous and porous materials, which find applications in room acoustics and environmental acoustics and are generally included in the design of electronic devices to reduce unwanted sound emissions. Traditional absorbing materials dissipate sound energy through viscous friction, providing significant absorption in the medium to high- frequency range. They are economical, easy to manufacture, and effective in numerous applications. However, traditional materials do not provide good absorption in the low-frequency range, require maintenance, and may, in some cases, pose risks due to deterioration, making them unsuitable in critical contexts. In recent years, innovative materials have entered the discussion of sound absorption and noise control—acoustic metamaterials (AMM). AMMs are engineered structures whose acoustic properties depend on geometries rather than the materials they are made of. This fact allows them to be made with a specific material based on requirements, whether hygiene, sustainability, cost-effectiveness, or low maintenance. Furthermore, they generally do not require thicknesses on the order of a quarter wavelength, typical of traditional materials, potentially achieving optimal performance even for low-frequency absorption through compact structures. Despite their technological innovation value, metamaterials have had few applications in real-world contexts. This thesis aims to develop a rigorous method for designing and engineering a specific class of acoustic metamaterials consisting of resonant elements: Quarter Wavelength Resonators (QWR) and Helmholtz Resonators (HR) have been used to design innovative solutions in two different contexts. The first involves the development of a passive sound absorber for noise control in hospital environments. The second entails using acoustic metamaterials for unwanted noise

control in loudspeakers and audio systems. The common thread is to reduce noise emissions by overcoming the limitations and inefficiencies of traditional materials. The method begins with analytical models and uses numerical modeling as a tool for design optimization. Various 3D printing techniques are examined in detail to achieve a prototyping method correlated with acoustic performance, verified through experimental measurements in the impedance tube. Finally, validation methods have been adopted to assess the specific effectiveness. In hospital environments, the application involved the development of a broadband absorption metamaterial, which helped reduce reverberation time and sound pressure levels inside a hospital room. A structure of twenty parallel Helmholtz resonators was developed to achieve absorption in the frequency range between 450 and 1200 Hz. Loudspeaker applications were conducted in collaboration with the *Research and Development department* of RCF, an Italian speaker company. It involved two different case studies. The first focused on absorbing rear radiation emitted by a tweeter, for which a metamaterial consisting of fourteen parallel quarter-wavelength resonators was designed for broadband absorption between 700 and 20000 Hz. The second aimed at reducing mid-low frequency resonances of a vented-port loudspeaker caused by the generation of standing waves inside the cabinet, for which two different AMMs based on quarter-wavelength resonators were developed. The results demonstrate how the application of acoustic metamaterials may serve as a solid alternative to traditional materials in various fields, enhancing absorption performance and adapting to stringent requirements. The thesis serves as a starting point for designing acoustic metamaterials, providing theoretical insights and practical considerations for their physical realization.

# Sommario

Negli ultimi decenni, il rumore è diventato sempre più presente nella vita quotidiana delle persone. Gli effetti dell'esposizione al rumore sono al centro di dibattito e normative sempre più stringenti cercano di limitare l'esposizione delle persone ad elevati livelli di rumore. L'assorbimento acustico è un concetto fondamentale quando si affronta il tema del controllo del rumore, ed è definito come la dissipazione dell'energia acustica associata ad un'emissione. Ad oggi, i materiali fonoassorbenti più utilizzati sono i tradizionali materiali fibrosi e porosi, che trovano applicazioni nell'acustica ambientale, nella room acoustics, e vengono generalmente inclusi nel design di dispositivi elettronici per ridurne le emissioni sonore indesiderate. I materiali tradizionali dissipano l'energia sonora attraverso l'attrito viscoso e forniscono un'assorbimento significativo nel range delle medio-alte frequenze. Sono economici, di facile realizzazione ed efficaci in numerose applicazioni. Tuttavia, risultano carenti nell'assorbimento a bassa frequenza, richiedono manutenzione e possono, in alcuni casi, comportare rischi dovuti al deterioramento, rendendoli inadatti in contesti critici. Negli ultimi anni, una nuova classe di materiali innovativi è entrata nel dibattito dell'assorbimento e il controllo del rumore: i metamateriali acustici (AMM). Gli AMM sono strutture ingegnerizzate le cui proprietà acustiche dipendono dai parametri geometrici piuttosto che dai materiali di cui sono costituiti. Questa proprietà permette che siano realizzati con un determinato materiale in base ad esigenze specifiche, che esse siano di igiene, sostenibilità, costo contenuto o di ridotta manutenzione. Inoltre, generalmente non necessitano di spessori dell'ordine di un quarto d'onda, tipici dei materiali tradizionali, permettendo di ottenere prestazioni ottimali anche per l'assorbimento a basse frequenze attraverso strutture compatte. Nonostante il loro straordinario valore di innovazione tecnologica, i metamateriali, fino ad oggi, hanno poche applicazioni in contesti reali. Questa tesi ha come obiettivo lo sviluppo di un metodo rigoroso per il design e la progettazione di una specifica classe di metamateriali acustici formati da elementi risonanti: risonatori a quarto di lunghezza d'onda (QWR) e risonatori di Helmholtz (HR) sono stati utilizzati

al fine di progettare soluzioni innovative in due contesti differenti. Il primo è lo sviluppo di un fonoassorbente passivo per il controllo del rumore negli ambienti ospedalieri. Il secondo coinvolge l'uso di metamateriali acustici per il controllo del rumore indesiderato negli altoparlanti e nei sistemi audio. Il filo conduttore è quello di ridurre l'emissione di rumore superando le limitazioni e l'inefficienza dei materiali tradizionali. Il metodo parte dai modelli analitici e si avvale della modellazione numerica come strumento di ottimizzazione del design. Diverse tecniche di stampa 3D sono esaminate nel dettaglio al fine di ottenere un metodo di prototipazione correlato alle prestazioni acustiche, verificate tramite misure sperimentali nel tubo d'impedenza. Infine, sono stati adottati metodi di validazione per verificarne l'efficacia nei vari contesti. L'applicazione in ambiente ospedaliero ha previsto lo sviluppo di un metamateriale per assorbimento broadband, che ha contribuito a diminuire il tempo di riverberazione e i livelli di pressione sonora all'interno di una camera di degenza. Una struttura di venti risonatori di Helmholtz in parallelo è stata sviluppata al fine di ottenere un assorbimento nel range in frequenza tra i 450 e i 1200 Hz. Le applicazioni in ambito loudspeaker sono state effettuate in collaborazione con il *Dipartimento di Ricerca e Sviluppo* di RCF, un'azienda italiana di altoparlanti. Ha riguardato due casi studio differenti. Il primo focalizzato all'assorbimento della radiazione posteriore emessa da un tweeter, per cui è stato progettato un metamateriale formato da quattordici risonatori a quarto di lunghezza d'onda in parallelo per un assorbimento broadband nel range tra i 700 e i 20000 Hz. Il secondo ha previsto la riduzione delle risonanze in medio-bassa frequenza di un subwoofer dovute alla generazione di onde stazionarie all'interno del cabinet, per cui sono stati sviluppati due AMM differenti basati su risonatori a quarto di lunghezza d'onda. I risultati presentati in questa tesi dimostrano come l'applicazione di metamateriali acustici possa rappresentare una valida alternativa ai materiali tradizionali negli ambiti più disparati, aumentando le performance di assorbimento e adattandosi a requisiti stringenti. La tesi rappresenta un punto di partenza per il design di metamateriali acustici, fornendo approfondimenti teorici e considerazioni pratiche per la loro realizzazione fisica.

# Table of contents

# List of figures

# List of tables

# Introduction

In the contemporary world, the concept of acoustic well-being has undoubtedly emerged as a pivotal concern that resonates deeply in our daily lives [2]. Noise, omnipresent in urban environments, has claimed a central role in influencing our comfort, productivity, stress, and mental health [3, 4]. It has become a key element of our daily experiences, whether in the workplace, during study sessions, or in our leisure moments. Over the past decades, acoustic well-being has gained prominence in controlling noise in work, study, and leisure environments and reducing emissions from electronic devices, ultimately enhancing the performance of audio reproduction systems. In the pursuit of noise mitigation, engineers and researchers have delved into defining objective parameters to quantify it, investigating subjective responses from those who experience it, and thoroughly scrutinizing the construction methods of materials that shape the acoustic environment. This evolution parallels the rapid advancements in technology, an upswing in research activities, and growing investments aimed at surpassing and redefining established norms and technological limits.

However, a substantial challenge remains the persistent tendency to overlook the importance of acoustics and noise control in the design of environments, home user products, and industrial goods. These crucial aspects are often relegated to a secondary status compared to other contemporary needs. Despite this, many studies have convincingly established the profound impact of sound on the mental and physical well-being of individuals who are subjected daily to a wide variety of noise sources [4, 5]. Workplaces and educational institutions have been subjects of extensive research for decades to assess the influence of acoustics on learning and work efficiency. As critical settings for patient recovery, hospitals have yet to meet the acoustic standards defined by numerous studies, which affirm that noise levels are excessive, hindering necessary rest for patients and the tranquility essential for staff and effective communication [6, 7]. Enhancing such environments is a perennial

challenge, requiring adherence to construction regulations, safety standards, and compliance with diverse criteria. The objective is to balance practical applicability, cost-effectiveness, and operational conditions harmoniously. In modern acoustics, this quest for equilibrium has been achieved by following conventional methods and materials considered as standards, which, however, have become outdated and technologically limited.

The most commonly used materials for controlling sound waves have been fibrous and porous materials for decades, with extensive literature comprising studies, analytical models, simulations, and real-world applications [8–11]. Due to their favorable acoustic properties, they have undeniably become the most widely employed material types. These properties are complemented by well-established manufacturing processes, low production costs, and predictability in their performance across various applications. Analytical models describing these materials are robust, having evolved over the decades, characterized by relatively simple parameters and easily measurable and predictable quantities. These models are typically analytical, empirical or semi-empirical [12–17], allowing designers to tailor their usage to specific application needs. However, the used fibrous or porous materials exhibit numerous limitations regarding applicability and from an ecological, sustainable, and maintenance perspective. These materials are subject to significant deterioration and can release particles into the air, potentially posing health risks. Moreover, they can be detrimental to the environment in which they are installed, whether it be a road noise barrier, workplace interior, electronic devices, audio reproduction systems, or any lived-in environment. Furthermore, these materials follow the quarter-wavelength absorption mechanism, proving effective for the absorption of mid-to-high frequencies. Consequently, the issue of low-frequency sound control has mainly remained unaddressed for decades[18, 19]. Often, attempts have been made to tackle this problem using alternative methods, which may offer some improvement but fall short of comprehensively addressing the low-frequency comfort and its impact on individuals.

The field of acoustic engineering is experiencing a significant transformation with the emergence of acoustic metamaterials [20–22]. In contrast to traditional fibrous and porous materials, these innovative materials offer numerous advantages. Acoustic metamaterials (AMMs) are innovative, engineered materials designed to manipulate and control sound waves in ways that traditional materials cannot [23]. The acoustic properties of AMMs depend primarily on the geometric parameters

rather than the materials they are made of. Therefore, different structures have emerged, each presenting a unique approach to sound control [24], offering versatile solutions to various acoustic challenges. Among these approaches, it is possible to achieve negative density metamaterials, which, by defying conventional mass laws, yield a negative effective density to exert extraordinary control over sound wave behavior. Periodic arrays, structured with specific geometric arrangements of unit cells, and sonic crystals, composed of periodic scatterer arrangements within a host material, include the creation of band gaps and distinctive dispersion properties [25]. Double-negative acoustic metamaterials operate on the principles of both negative effective mass and negative effective stiffness. Gradient index metamaterials, on the other hand, leverage property gradients to provide unique capabilities, including sound focusing and steering. Some metamaterials can amplify sound, while others possess cloaking abilities, making objects acoustically invisible by diverting sound waves around them [26]. Ultimately, local resonance metamaterials incorporate local resonators, fostering resonance effects that effectively attenuate or enhance specific frequency components in sound. Specifically, they can operate on the principle of Helmholtz resonance [27, 28], and exhibit unique acoustic properties by including subwavelength Helmholz resonators, resonating at specific frequencies [29, 30]. They can absorb or dissipate acoustic energy in a broadband frequency range by tuning the properties of coupled resonant microstructures, providing macroscopic dynamic properties not found in natural materials. One of the most remarkable advantages of acoustic metamaterials is their exceptional control over low-frequency sounds, an area where traditional materials have often fallen short. This capability addresses a critical gap in sound control, particularly in environments where low-frequency noise is a prevalent concern. Another compelling aspect is their versatility, offering compact design, predictable performance, low maintenance, and customizable acoustic features [31–34]. They can be fabricated from a wide range of materials, allowing engineers to select the most suitable material based on factors such as cost-effectiveness, structural compatibility, or environmental considerations. Tunability and efficiency allow for a high level of customization. Their design allows for precise adjustment to meet the specific acoustic requirements of an application. Additionally, AMMs can achieve high performance in a compact form, making them ideal for situations with strict space constraints, such as modern architectural designs and miniaturized electronic devices. Sustainability is another important consideration. AMMs can be designed with environmental impact in mind, minimizing waste,

reducing resource consumption, and offering longer lifespans, promoting more eco-friendly approaches to acoustic engineering [10, 35]. Compared to their traditional counterparts, the remarkable qualities of acoustic metamaterials position them as theoretically superior. In the contemporary landscape, an extensive body of literature meticulously details the analytical models for their design, numerical simulations for optimization, and their application in various acoustic contexts [36, 37].

However, translating these theoretical advantages into practical, real-world scenarios is a significant challenge. This involves identifying specific areas for their application, considering cost-effectiveness, ease of fabrication and installation, maintenance, and other practical advantages [38]. There are few tangible applications of metamaterials as sound-absorbing materials in environments [39–41] and even fewer applications to improve electronic devices, loudspeakers, and electroacoustic equipment [42–44]. The potential of acoustic metamaterials could substantially transform the field of noise control, providing innovative, functional, and tailored solutions due to their extreme customizability in various environments and offering unprecedented advantages compared to traditional materials.

## Thesis motivations and objectives

Nowadays, porous or fibrous materials are commonly employed in the majority of acoustic treatment applications. This is because, in most cases, they ensure a sufficient improvement in acoustic performance, whether required for building environments, electronic devices, or environmental acoustics. The choice of fibrous and porous materials is based on a compromise between good performance, cost-effectiveness, and ease of installation. However, these materials may not be suitable when specific requirements come into play, such as the need for installation in controlled environments or when specific and targeted acoustic properties are demanded. Acoustic metamaterials have been studied and analyzed for decades, and the underlying physical principles are already well-known. The real challenge lies in finding real-world applications for acoustic metamaterials in contexts where physical realization, technological advantages, and cost-effectiveness fall within a favorable application window for developers and users alike.

The purpose of this thesis is to provide the theoretical foundations for a specific class of metamaterials, namely resonance-based metamaterials, and to develop a method for designing, prototyping, and physically realizing these materials in two

specific real-world applications. To achieve this, the theoretical background describing the propagation of waves in homogeneous fluids will be introduced. Additionally, analytical models of two types of metamaterials based on the resonance principle, the Quarter Wavelength Resonator (QWR) and the Helmholtz Resonator (HR), will be presented using the Transfer Matrix Method approach. These analytical models are the initial step for designing and conceptualizing metamaterials for various scenarios. The numerical simulation method for optimizing metamaterials' geometries and acoustic properties will be explicitly outlined. In addition, various 3D prototyping techniques will be explored, along with their advantages and disadvantages. The best printing setups available on the equipment used to achieve the acoustic properties outlined by the models will be studied. Tolerances and printing parameters are explored to define a practical reference for the realization of metamaterials. Furthermore, the characterization techniques for these innovative materials will be described, encompassing measurements in the impedance tube of metamaterial prototypes. Finally, having delineated the utilized methodology, two applications of metamaterials in distinct fields will be presented. The first application involves the development of a new-generation absorptive material to be installed in hospital environments, aiming to improve acoustic conditions and, consequently, enhance acoustic well-being in critical spaces for patients and staff. The second application is focused on enhancing the quality of loudspeakers and audio systems, which have faced unresolved issues for decades. The proposed solutions aim to improve the quality and the subjective listening experience. For each application, methods for validating acoustic materials will be described to verify their true effectiveness in real-world scenarios.

# Overview of the thesis

The present thesis is divided into five chapters, presented hereafter.

## Chapter 1

Chapter 1 provides an overview of the background theory, including the most relevant concepts concerning wave propagation in fluids. The basic equations are stated to understand the context of the thesis. The concept of acoustic absorption is described, involving the methods to achieve it, and traditional porous and fibrous materials used in most applications are discussed, stating the mechanism of energy

dissipation and the analytical models describing their behavior. Additionally, acoustic metamaterials are introduced, including the innovation compared to traditional materials and the technological advantages that result from them. Finally, the focus will be on the specific class of metamaterials used in this thesis, namely, resonance-based metamaterials.

## Chapter 2

Chapter 2 details the adopted method, from the conception and design to the physical realization of metamaterials. Firstly, the Transfer Matrix Method (TMM) is introduced, which is the tool used to analytically model absorption and transmission problems, assuming plane wave propagation. Then, the analytical models of the Quarter Wavelength Resonator (QWR) and the Helmholtz Resonator (HR) are determined, and end corrections and effective parameters are explained. Then, the numerical method employed for optimizing geometries is presented. Specifically, detailed descriptions are provided for the numerical models utilized for acoustic metamaterials' characterization based on the finite element method (FEM). Furthermore, the entire prototyping phase is outlined, encompassing various printing techniques, printing parameters, and materials investigated to determine the optimal settings for 3D printing metamaterial samples. Lastly, the method for characterizing metamaterial samples is reported, including a description of experimental measurements in the impedance tube for the experimental calculation of absorption, reflection, and transmission.

## Chapter 3

Chapter 3 addresses the potential application of acoustic metamaterials to control the acoustic environment within a hospital room. The aim is to reduce the reverberation time and increase the comfort of patients and staff. This section describes the method for the hospital noise characterization through Sound Pressure Level (SPL) monitoring, a reverberation time measurement campaign, and a clustering analysis to quantify the contribution of different sources to the total pressure levels. Once the target spectrum for intervention is defined, the design of an acoustic metamaterial to be applied as a ceiling panel to reduce the reverberation time is shown. A hybrid Finite-Difference Time-Domain (FDTD) and Geometrical Acoustic (GA)

simulation of the considered environment is conducted to assess the improvement of the acoustical conditions with the metamaterial application.

### Chapter 4

Chapter 4 discusses the application of acoustic metamaterials in loudspeakers and audio systems. Specifically, it focuses on two distinct case studies: the first deals with a high-frequency tweeter, aiming to absorb the rear radiation reflected in the enclosure; the second application of metamaterials deals with a vented-port loudspeaker for low frequencies. In the latter, the goal is to eliminate resonances caused by standing waves generated in the bass-reflex box. In both cases, the design and development of metamaterials are examined from analytical, numerical, and experimental perspectives.

### Chapter 5

Chapter 5 focuses on discussing the method developed and explained in Chapter 2 and the two different applications of acoustic metamaterials for different purposes. Moreover, it contains the final remarks and insight into possible future developments.

## Main contributions

The main contributions of this thesis are:

- The proposal of a rigorous method to develop, optimize, and physically make acoustic metamaterials based on Quarter Wavelength Resonators and Helmholtz Resonators.

- The investigation of various 3D printing techniques, with the aim of demonstrating the advantages and disadvantages of each in the prototyping of acoustic metamaterials;

- The study of optimal printing settings to achieve acoustic metamaterials with acoustic properties consistent with those of predictive models.

- A characterization of the environmental noise in the hospital settings through SPL monitoring, a reverberation time measurement campaign, and a clustering analysis of the noise sources.

- The proposal of the application of acoustic metamaterials as passive absorbers within a hospital room to decrease the reverberation time and sound pressure level.

- The design and implementation of an acoustic metamaterial to reduce reflections caused by the enclosure of a high-frequency tweeter.

- The development of two specific metamaterials to reduce resonances generated by standing waves within a loudspeaker cabinet equipped with a vented port.

# Chapter 1

# Theoretical background

This chapter delves into the fundamental mechanisms governing the propagation of acoustic waves in fluids. The equations governing wave physics and the fundamental quantities are presented. Additionally, the concept of acoustic absorption will be introduced, and the modes of acoustic energy dissipation will be explained. Furthermore, traditional materials for acoustic absorption will be introduced: analytical models and characteristic properties of fibrous and porous materials, representing the most commonly used materials in sound absorption today. Finally, acoustic metamaterials will be introduced, starting from their working principles and their main innovative features compared to traditional materials, up to the different concepts of absorption, diffraction, focusing, and cloaking. This chapter will also focus on the fundamental mechanisms of a specific class of metamaterials, resonance-based metamaterials, which allow the control of acoustic waves through resonant interactions. By strategically designing the dimensions and configurations of these resonators, it becomes possible to create materials that can filter out, enhance, or bend sound waves in various ways and for several distinct purposes. This versatility has significant implications in diverse fields, from architectural acoustics for noise reduction to electronic devices.

## 1.1 Wave propagation in homogenous linear fluids

Acoustic waves are characterized as a form of mechanical energy transmission through a medium, for instance, via adiabatic compression and decompression in fluids. This transmission occurs due to particles vibrating around their equilibrium positions, assuming the medium's elasticity (Figure 1.1). Consequently, in an elastic

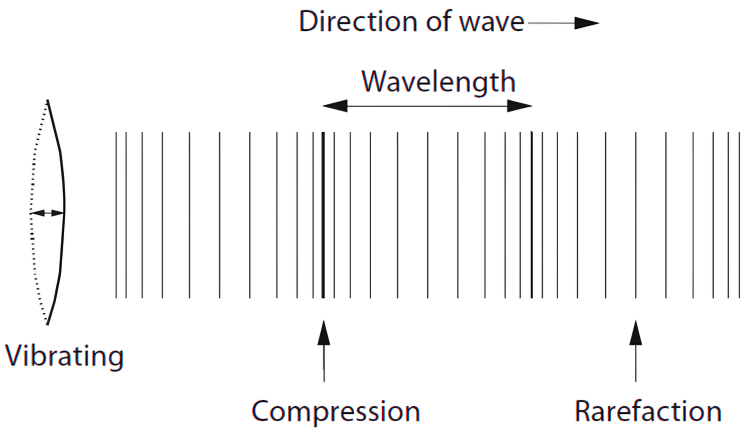


Fig. 1.1 Compression and rarefaction of the air caused by acoustic waves. Credits picture: Barron, M. [45]

transmitting medium, a sound wave induces variations in pressure. Specifically, it causes dynamic pressure deviations within the local ambient or static pressure [46]. For the purpose of this thesis, the wave propagation in air will be discussed. It is, therefore necessary to recall the following properties:

- Air is a homogeneous fluid (i.e., materials whose properties are spatially uniform) and isotropic (i.e., materials whose properties are independent of direction).
- Air is an ideal fluid, inviscid, and lossless, and therefore lacks dissipative effects due to viscosity ($\mu_0 = 0$).
- Pressure and density perturbations are small compared to the average atmospheric pressure and density values [47].
- State changes are adiabatic, meaning that there is no heat interchange between areas of low pressure and areas of high pressure due to the rapid movement of the particles [47].

As a result, the sound pressure at a specific point, at a specific time $t$, can be defined as:

$$p(x,t) = p'(x,t) - p_0 \tag{1.1}$$

where $x$ is the position, $p_0$ is the atmospheric pressure.

### 1.1.1 The wave equation

The comprehensive equation that describes wave propagation can be formulated by combining the equation of state, the continuity equation, also known as the conservation mass law, and Euler's equation of fluid dynamics.

For an ideal gas, the equation of state gives the following thermodynamic relationship [48]:

$$p = r\rho T \tag{1.2}$$

where $p$ is the total pressure, $r$ is a constant that depends on the fluid $\rho$ is the density of the fluid, and $T$ is the absolute temperature. If the thermodynamic process is restricted, it is possible to derive from Eq.1.2 the adiabatic equation of state, considering no exchange of thermal energy between fluid particles [49]:

$$\frac{p}{p_0} = \left(\frac{\rho}{\rho_0}\right)^{\gamma} \tag{1.3}$$

where $p_0$ is the static pressure, $\rho_0$ is the equilibrium density of the fluid, and $\gamma$ is the ratio of specific heats of the fluid.

The continuity equation describes the relation between the particle velocity $v$ due to the compression and expansion of the fluid. It states that the change in time of the mass contained in the volume considered is equal to the mass that passes through the volume:

$$\frac{\partial \rho}{\partial t} = -\rho_0 \nabla \cdot v \tag{1.4}$$

where $\rho_0$ is the instantaneous density of the air. The linear Euler's equation is the second fundamental law, also known as the conservation of momentum [46], and it is defined as:

$$\rho_0 \frac{\partial v}{\partial t} = -\nabla p \tag{1.5}$$

where $\rho_0$ is the static value of the air density, $v(x,t)$ is the vector field particle velocity, $p(x,t)$ is the sound pressure. Assuming the fluid as inviscid, i.e., the rotation effects of the flow can be considered neglected, and assuming the vector particle velocity $v(x,t)$ irrotational, i.e. $v = -\nabla u$ being $u$ the velocity potential, equation 1.5 can be rewritten in the form:

$$p = -\rho_0 \frac{\partial u}{\partial t} \tag{1.6}$$

The combination of equation 1.2, 1.4 and equation 1.5 allows to obtain the so-called wave equation for continuum medium, which describes the propagation of waves in a homogeneous fluid. This equation is a second-order, linear, partial differential equation for mechanical waves, and it can be expressed in its general three-dimensional form as follows:

$$\frac{\partial^2 p}{\partial t^2} = c^2 \nabla^2 p \tag{1.7}$$

where $p$ represents the instantaneous variation in pressure relative to the equilibrium value, $t$ is time, $c$ is the speed of sound in the fluid, $\nabla^2$ is the Laplacian operator, which denotes spatial Laplacian, i.e., the divergence of the gradient. Equation 1.7 is the time-dependent form of the wave equation. Generally, the sound pressure can be assumed as a time-harmonic signal of the type:

$$p(x,t) = P(x)e^{-i\omega t} \tag{1.8}$$

where $P$ is the pressure amplitude and $\omega$ is the angular frequency of the oscillation. Equation 1.8 can be written in its time-independent form:

$$p(x,t) = P(x)e^{-ikx} \tag{1.9}$$

where $kx$ is the scalar product of the scalar coordinate $x$ and the wave number $k$. This plane wave solution describes a harmonic sound wave that does not change in the space on each plane normal to the propagation vector $k$. Combining equations 1.7 and 1.8, it is possible to obtain the so-called Helmholtz equations, defined as:

$$\nabla^2 p = -k^2 p \tag{1.10}$$

The wave number $k$ can be expressed as a function of the speed of sound as:

$$k = \frac{\omega}{c} \tag{1.11}$$

The speed of sound in a medium, in its turn, can be expressed in terms of the bulk modulus ($K$) and mass density ($\rho$), which are two characteristic parameters of the medium:

$$c = \sqrt{\frac{K}{\rho}} \tag{1.12}$$

The bulk modulus $B$ quantifies a material's resistance to changes in volume due to external pressure, while mass density $\rho$ characterizes the amount of mass contained within a given volume of fluid or material. In case of free air, the speed of sound is defined as:

$$c_0 = \sqrt{\frac{K_0}{\rho_0}} \tag{1.13}$$

where $K_0 = 1.42 \cdot 10^9\,[N/m^2]$ and $\rho_0 = 1.204\,[kg/m^3]$ with a temperature of 20° C, in ideal condition. This definition defines the speed of sound as a macroscopic parameter of a specific fluid or material and will be used in this thesis. By defining the speed of sound and the density, it is possible to define the characteristic acoustic impedance, a property of a material's resistance to the incidence of sound waves. In the case of air, the acoustic impedance is defined as:

$$Z_0 = \rho_0 c_0 \tag{1.14}$$

## 1.2 Principle of sound absorption and acoustic energy dissipation

Acoustic absorption is a fundamental aspect of controlling sound waves in various environments. Its primary purpose is to mitigate the reflection and manage the distribution of sound waves within a given space. By strategically incorporating absorbing materials, it is possible to reduce the impact of undesirable effects, such as high noise levels, unwanted resonances, and consequent discomfort, through a wide range of physical mechanisms. A scattering event occurs when acoustic waves encounter a physical material with specific properties (i.e., when the wavelength is comparable with the object's size): part of the energy is scattered back or reflected, and part of the energy is transmitted through the path. If losses are not considered, energy is conserved. This means that the incident wave equals the sum of the reflected and transmitted waves. In a real-world scenario, materials exhibit intrinsic losses, so the material absorbs part of the reflected wave. When a sound wave hits a uniform and infinite surface, some sound energy is reflected with a different amplitude and phase, which depend on the surface characteristic. The characteristic impedance can be described by $Z$, which is a complex quantity, frequency-dependent, defined as the

ratio of the acoustic pressure $p$ and the acoustic volume flow $V$:

$$Z = \frac{p}{V} = \frac{p}{vS} \tag{1.15}$$

where $v$ is the particle velocity, and $S$ is the area of the surface. The surface impedance is defined by the characteristic wavenumber $k$ and characteristic impedance $Z$ as follows:

$$Z_s = -iZ\cot kL \tag{1.16}$$

Note that in the context of sound absorption, impedance matching occurs and involves adapting the impedance of the absorbing material $Z_s$ to that of the surrounding air $Z_0$. Optimal acoustic absorption occurs when two impedances are well-matched. This matching ensures that sound waves can efficiently transfer energy into the absorbing material without significant reflection. Acoustic reflection $R$ can be expressed in terms of impedances as follows:

$$R = \frac{Z_s - Z_0}{Z_s + Z_0} \tag{1.17}$$

Consequently, the absorption coefficient can be defined as:

$$\alpha = 1 - |R|^2 \tag{1.18}$$

## 1.3 Classical sound absorbers: porous and fibrous materials

Porous and fibrous materials [50, 9, 51] are traditional passive sound absorbers that attenuate noise by converting energy into heat. Specifically, they provide absorption through viscous and thermal losses. Thermo-viscous losses refer to the dissipation of sound energy due to the viscosity and thermal conductivity of the medium through which the sound waves propagate. Specifically, when a sound wave propagates through a fluid or a gas, the molecules of the medium are set in motion by the pressure variations of the sound waves. However, due to the viscosity of the medium, some of the kinetic energy associated with this motion is converted into heat, contributing to the dissipation of the energy. The so-called poroelastic materials consist of a solid skeleton and a fluid phase, typically air. The assumption is that the fluid is compressible and capable of flowing relative to the solid, resulting

in friction. Thus, investigating poroelastic materials involves understanding the behavior of the solid phase, the fluid phase, and the interaction between the two. The frequency-dependent nature of their sound dissipation is notable. It performs

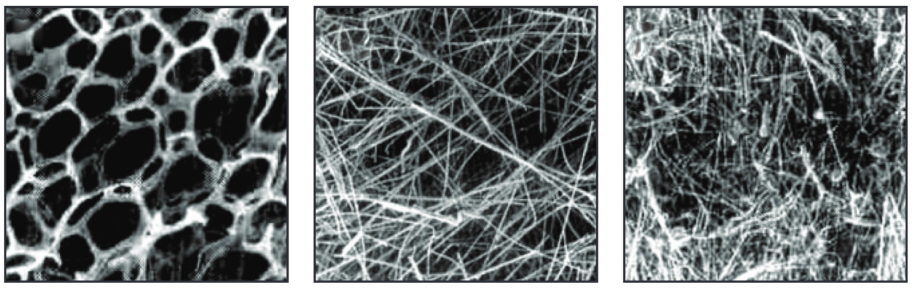


Fig. 1.2 Three different microstructures of porous materials: (Left) Plastic foam; (Center) Glass fiber; (Right) Mineral wool. [1]

effectively at higher frequencies where a heat loss is generated due to friction when sound waves traverse the fluid phase. Effective absorption is associated with the solid-air interface, governed by two mechanisms: viscous dissipation near the solid surface and heat conduction through the skeleton. Although heat is conducted through the solid phase, the most important effect defining absorption in conventional materials is heat conduction in the fluid phase. In fact, this effect determines the effective compressibility of the permeable medium. Porous and fibrous materials exhibit substantial dissipation coefficients owing to their extensive microstructured air-solid interfacial area. Dissipation, while crucial, is not the sole parameter for sound absorption. Interface impedance matching plays a vital role, defined as the product of mass density and sound velocity. Achieving impedance matching with air ensures minimal reflection from the sound-absorbing structure, maximizing sound energy absorption within the material. When a traditional porous and fibrous absorber is backed by an impervious wall, the lowest frequency absorption peak matches the quarter-wavelength resonance frequency given by the formula [52]:

$$f_n = \frac{c_p}{4L} \tag{1.19}$$

where $c_p$ is the speed of sound inside the material, and $L$ is the total thickness of the material. This is the so-called quarter wavelength resonance due to interference phenomena. Thus, the thickness of the porous material should be large to obtain absorption at low frequencies, limiting their use in many practical applications.

Moreover, studying sound propagation in these materials can be challenging due to their intricate internal geometries. Averaging measures and coefficients must be applied on a macroscopic scale through volume homogenization to address these complexities. Additionally, by considering the frame as motionless, the air within the skeleton can be replaced on a macroscopic scale by an equivalent free fluid, and it is important to define some typical parameters, which will be described next [53]:

- The porosity $\phi$ is defined as the fraction of volume filled with air on the total volume;

- The flow resistivity $\sigma$ depends on the air-filled space size and, for anisotropic materials, on the direction of flow relative to the layered fibers. It characterizes the ability of porous materials to impede airflow through their structure and measures how easily air can pass through the material.

- The tortuosity $\alpha_\infty$ quantifies the slowdown effect on the propagating waves because waves tend to travel most of the air-filled spaces, which are not straight.

Analyzing porous and fibrous materials involves employing mathematical models to understand and predict their behavior in response to sound waves. Various model have been developed in the last decades, each with its set of parameters and assumptions. The Delany-Bazley (DB) model [14] is the simplest empirical model for predicting sound absorption. It considers the flow resistivity and the porosity of the material to determine the sound absorption of a mateerials. Usually, it is not suitable for the low to mid-frequency range.

The Johnson-Champoux-Allard (JCA) [54, 15, 55] employs Biot's theory [56] of poroelasticity and is the most used phenomenological model. This model is more physically correct than the previous one and uses a macroscopical approach, considering the material to be a compressible fluid. It considers air flow resistivity, porosity, and tortuosity and introduces two characteristic lengths to consider viscous-thermal dissipations. The effective density and the effective bulk modulus are given by:

$$\rho_p(\omega) = \rho_0 \frac{\alpha_\infty}{\phi}[1 - iG_1(\omega)\sqrt{1 + iG_2(\omega)}] \tag{1.20}$$

$$K_p(\omega) = K_0 \frac{\phi^{-1}}{\gamma - (\gamma - 1)[1 - iG_1'(\omega)\sqrt{1 + iG_2'(\omega)}]} \tag{1.21}$$

where $\rho_0$ and $K_0$ are the density and bulk modulus of the fluid the porous material is saturated by, and $G_1$, $G_2$, $G_1'$, $G_2'$ are defined as:

$$G_1(\omega) = \frac{\sigma\phi}{\alpha_\infty \rho_0 \omega} \qquad G_2(\omega) = \frac{4\alpha_\infty^2 \rho_0 \eta \omega}{\sigma^2 \phi^2 \Lambda^2} \tag{1.22}$$

$$G_1'(\omega) = \frac{8\eta}{\rho_0 Pr \Lambda'^2 \omega} \qquad G_2'(\omega) = \frac{\rho_0 Pr \Lambda'^2 \omega}{16\eta} \tag{1.23}$$

where $Pr$ is the Prandtl number, $\Lambda$ and $\Lambda'$ are the characteristic lengths for thermal and viscous dissipations. The complex effective impedance and the effective wavenumber for a porous material can be obtained as follows:

$$Z_p = \sqrt{\rho_p K_p} \tag{1.24}$$

$$k_p = \omega \sqrt{\frac{\rho_p}{K_p}} \tag{1.25}$$

Note that the effective parameters are the intrinsic properties of the material and do not depend on the boundary conditions of a considered system.

Acoustic absorption of traditional porous and fibrous materials presents various challenges and limitations in various aspects. One primary constraint lies in the physical limitations of these materials, often dictated by their inherent properties. As said before, the effectiveness of traditional materials tends to diminish as the frequency decreases, making them less suitable for applications demanding absorption in low-frequency ranges. Moreover, the sustainability aspect of porous and fibrous materials raises concerns [10]. These materials, often derived from natural sources, may pose environmental risks due to their extraction and production processes. Additionally, these materials' degradation and wear and tear over time can lead to a decline in acoustic absorption performance. This deterioration compromises their long-term effectiveness and can result in maintenance challenges and potential risks, especially in critical applications [9]. Another important limitation is the spatial requirement associated with traditional materials. Large volumes of these materials are often needed to achieve significant absorption, leading to bulkier and less aesthetically pleasing acoustic solutions. These challenges underscore the importance of investigating innovative materials and approaches to overcome the inherent limitations of these conventional sound-absorbing materials.

## 1.4 Acoustic metamaterials

Metamaterials have emerged as innovative materials in various scientific domains, initially finding their roots in the manipulation of electromagnetic waves [57]. These engineered materials, featuring unique structures with properties not found in nature, revolutionized fields like optics and electromagnetic wave control [58]. As the metamaterial investigation progressed, researchers recognized the potential of applying these principles to the field of acoustics, thereby ushering in a new era of sound engineering [24]. Acoustic waves and electromagnetic waves behave differently in fluids, as the former are longitudinal scalar waves, while the latter are transverse vector waves with two polarizations. However, an analogy can be drawn between the two through the following correspondences involving density $\rho$ and bulk modulus $K$ from the acoustical perspective, and the dielectric constant $\varepsilon$ and the magnetic permeability $\mu$, as follows:

$$c_{sound} = \sqrt{\frac{K}{\rho}} \qquad c_{light} = \sqrt{\frac{1}{\mu\varepsilon}} \tag{1.26}$$

Thanks to these relationships, it can be stated that the two types of waves share most of the underlying physics, leading to negative refraction, superlens, and cloaking.

Acoustic metamaterials represent an emerging class of sound-absorbing materials that has garnered significant attention for its transformative potential in manipulating and controlling sound. Metamaterials offer numerous advantages unlike traditional materials, which exhibit inherent acoustic properties and have limitations imposed by the mass density law, in the case of trasmission problems [20]. They can derive their uncommon characteristics from engineered structures and overcome traditional absorbers' limitations, offering dimensions much smaller than the wavelength of the sound wave. Moreover, they can be made from any material, as their acoustic properties do not depend on the material they are made but rather on the geometric parameters that characterize them. For this reason, they also offer advantages when hygiene, maintenance, and sustainability are crucial factors. Additionally, AMMs can overcome the low-frequency absorption issue that has remained unresolved for many years in various contexts with traditional materials. The analogical characteristic between sound waves and electromagnetic waves gives rise to phenomena like negative refraction [59], invisible cloaks [60], and wavefront manipulation [61] through specific designs. AMMs may regulate acoustic behavior, leading to negative

effective mass density and negative bulk modulus based on localized resonance mechanisms and scattering properties [24] rather than Bragg scattering, as observed in band gap materials known as phononic crystals [62, 63].

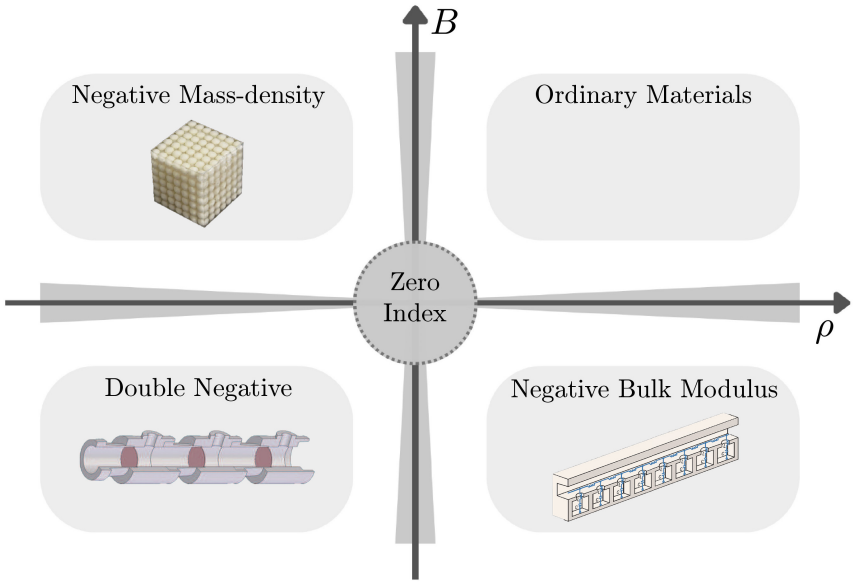


Fig. 1.3 Extreme constitutive parameters. The ordinary materials found in nature exhibit positive real part of the mass density and bulk modulus. An example of a negative mass density material is the subwavelength resonator (mega-atoms), made of metallic spheres coated with a soft layer of silicon rubber. A negative bulk modulus materialis an acoustic waveguide loaded with Helmholtz resonators. Double negative materials can be provided by combining negative mass density and negative bulk modulus effects. Moreover, Zero-Index materials can be achieved by an array of symmetric blind holes whose band structure possesses a Dirac-like cone at the center of the Brillouin zone. All figures are adapted with permission [20].

In natural media like air and traditional porous and fibrous materials, the real part of the bulk modulus and mass density is constrained to positive values (as depicted in Figure 1.3, first quadrant). Conversely, Acoustic Metamaterials (AMMs) can be intentionally engineered to exhibit a wide range of effective constitutive parameters, including not only positive values (whether very large or very small) but also negative values. According to the definition of bulk modulus and mass density, it is possible to affirm that certain AMM structures can exhibit negative mass density [64, 65], such as subwavelength resonators (mega-atoms) made of metallic spheres coated with a soft layer of silicon rubber. Similarly, structures may show negative bulk modulus [66], like acoustic waveguides loaded with Helmholtz resonators, showcas-

ing unconventional behavior. Combining materials with negative mass density and negative bulk modulus makes it possible to create double-negative materials [59]. Zero-Index materials can be achieved by utilizing an array of symmetric blind holes, whose band structure possesses a Dirac-like cone right at the center of the Brillouin zone [67]. Exploring extreme constitutive parameters opens up new possibilities in material science and acoustics, allowing for the development of materials with unprecedented characteristics and functionalities.

### 1.4.1 Resonance-based metamaterials

Metamaterials based on the principle of resonance are engineered structures developed to absorb sound waves at specific frequencies selectively. By adjusting the geometrical dimensions and properties of the resonators, these materials can be tailored to absorb unwanted sound waves while allowing others to pass through [68]. Their mechanism relies on localized resonances, where specific structural features interact with sound waves at targeted frequencies. These resonances result in enhanced absorption or reflection depending on the purpose they are developed for. In this thesis, the Quarter-Wavelength Resonator and the Helmholtz Resonator are two types of resonators considered for designing metamaterials (Figure 1.4).

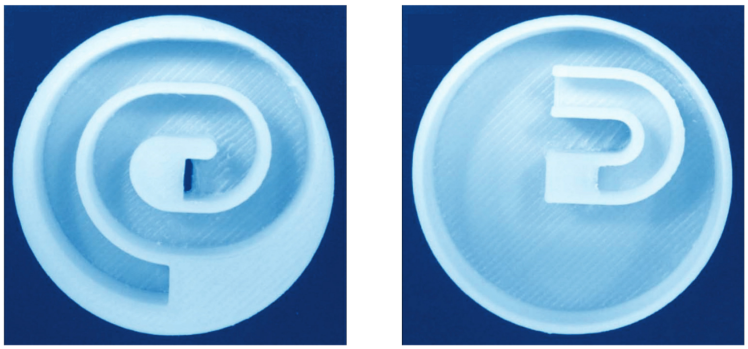

Fig. 1.4 (Left) Photograph of a coiled-up QWR; (Right) Photograph of a coiled-up HR. Both show a narrow band absorption that depends on the geometrical parameters.

#### Quarter-wavelength resonator

A *quarter wavelength resonator (QWR)* is an acoustic device based on the principle that when the length of an open cavity with a rigid end is one-fourth of the wavelength of the desired sound, an acoustic resonance occurs. In other words, resonances occur

when a quarter, and odd multiples of a quarter, of the acoustic wavelength are equal to the resonator length. At this frequency, this phenomenon significantly increases the amplitude of sound waves, which are absorbed and attenuated. Not considering losses, the resonance frequency of a QWR is determined by the formula:

$$f_{\text{res}} = \frac{N \cdot c}{4L} \tag{1.27}$$

Where $N$ is an integer, $c$ is the speed of sound in air, $L$ is the length of the resonator's cavity. The absorption mechanism in a quarter wavelength resonator is based on the interference effect of acoustic waves. When the sound frequency matches the resonator's resonance frequency, the waves reflected from the closed end of the cavity interfere with the incident waves, creating a cancellation or attenuation of sound waves at that specific frequency. The combination of incident and reflected waves results in a decrease in sound amplitude at $f_{\text{res}}$, representing the absorption of sound by the quarter wavelength resonator. One of the main properties of the QWR is that they can achieve high absorption levels through air viscosity dissipation. Moreover, its dimensions can be scaled by coiling the cavity. The coiled-space concept can be compared to the tortuosity concept described for porous and fibrous materials [53].

On the other hand, the biggest disadvantage is that, generally, the sound is absorbed in a small frequency band around the resonance frequencies of the air inside the resonator, as shown in Figure 1.5. It is possible to notice that the sound

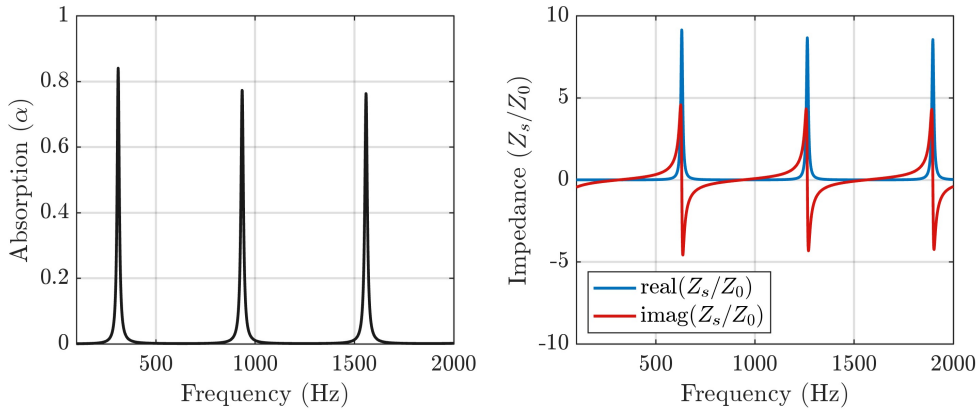


Fig. 1.5 Sound absorption coefficient and normalized impedance of a QWR with a length $l = 0.27$ m, and a side $a = 0.01$ m. The fundamental absorption peak is at 310 Hz; the first and the second harmonics at 935 Hz and 1559 Hz, respectively.

absorption coefficient presents a first peak of absorption at a certain frequency $f_1$,

which corresponds to the frequency of the quarter wavelength dimension of the resonator. There are additional frequencies of absorption that are integer multiples of the fundamental resonance frequency. Referring to Eq. 1.16 the surface impedance of a QWR is a complex quantity: it is important to notice that in the absorption frequency of the QWR, the imaginary part of the impedance is equal to 0, meaning that when perfect absorption occurs there is a matching between its impedance and the impedance of the air surrounding, and $Z_s = Z_0$, where $Z_0$ is the characteristic impedance of air. Coupled resonators with different lengths and cross-sections can be designed to overcome the narrow band absorption, creating multi-resonant systems.

### Helmholtz resonator

The *Helmholtz resonators (HRs)* possess the unique ability to resonate at frequencies characterized by wavelengths significantly exceeding the physical dimensions of the resonator itself. This distinctive property has propelled the widespread integration of HRs into the realm of acoustic metamaterial design, especially considering that acoustic metamaterials, by definition, are sub-wavelength in both size and dimensions. The fundamental structure of Helmholtz resonators comprises two key elements: a cavity with rigid walls and an extending neck. This specific arrangement allows HRs to resonate at distinct frequencies reminiscent of a mass-spring system. The air within the resonator's neck is the oscillating mass, while the adiabatic compression of air within the cavity provides the spring constant. In the presence of an incident acoustic wave, a displacement of the air mass in the neck happens. As the mass moves downward, it diminishes the cavity volume, increasing pressure. This process persists until the pressure is substantial enough to push the mass back into the cavity. The resonance frequency of an HR can be expressed in function of the geometrical parameters:

$$f_{res} = \frac{c}{2\pi}\sqrt{\frac{S}{V \cdot l_n}} \tag{1.28}$$

where $S$ is the area of the neck, $l_n$ is the length of the neck, and $V$ is the volume of the cavity. This definition does not consider losses inside the neck and the cavity. On the contrary, to take into account thermo-viscous losses, effective parameters have to be considered. Unlike the QWR, the Helmholtz resonator surpasses the quarter-wavelength absorption mechanism. This means that it can absorb at very low frequencies with compact geometric dimensions. Like the QWR, the Helmholtz resonator also has a narrow absorption band, as shown in Figure 1.6. The fundamental

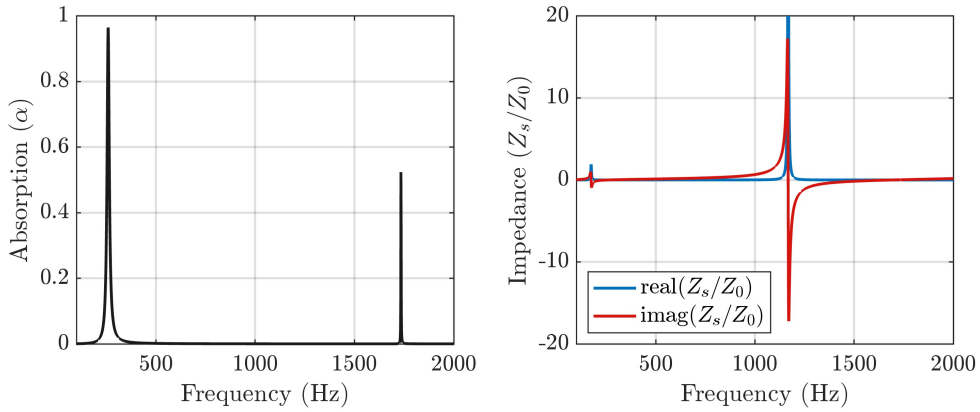


Fig. 1.6 Sound absorption coefficient and normalized impedance of an HR with a length of the neck $l_n = 0.01$ m, and a side of the neck $a_n = 0.004$ m, a length of the cavity $l_c = 0.10$ m, and a side of the cavity $a_c = 0.025$. The fundamental absorption peaks is at 259 Hz, and the first harmonic at 1734 Hz.

absorption frequency occurs when the wavelength of the incident sound wave is such that it corresponds to the effective length of the resonator's neck. The harmonics refer to absorption peaks at frequencies multiple integer of the fundamental resonance. The complex impedance can be used to design HRs: as it occurs for QWR, there is perfect absorption when the impedance of the HR matches the characteristic impedance of the air, $Z_s = Z_0$. For this reason, it can be implemented in multi-resonator systems to achieve more broadband absorption. Like the previous resonator type, it can be folded to minimize space requirements further.

# Chapter 2

# Method

This thesis chapter will address the method used to design acoustic metamaterials for several applications. The first step is to introduce the necessary tools for the analytical modelling of wave propagation, assuming the assumption of plane wave propagation. The Transfer Matrix Method (TMM) formulation will be described as a tool to simplify and handle complex structures, in the case of absorption and transmission scenarios. The focus will then be centered on wave propagation in ducts, and the TMM will be used to describe the characteristic parameters of the acoustic metamaterials of interest for this thesis, namely the Quarter-Wavelength resonator (QWR) and the Helmholtz resonator (HR). This includes a specific description of thermo-viscous losses and end corrections. Then, the design process progresses to numerical modeling. Numerical simulations conducted using Comsol Multiphysics allow for a more detailed and accurate representation of the metamaterial's performance under various conditions. These simulations consider a broader range of factors, enabling fine-tuning and optimizing the design. Finally, the transition from numerical models to physical prototypes involves selecting appropriate manufacturing techniques, such as Fuse Deposition Modelling (FDM) and Stereolithography (SLA). The prototyping techniques using 3D printing will be described, along with their advantages, limitations, and encountered challenges. The prototypes undergo experimental validation, comparing real-world measurements with the predictions of the analytical and numerical models. The setup for prototype characterization will be delineated based on experimental measurements in the impedance tube of metamaterials unit cells. This iterative process ensures that the final metamaterial design aligns with the intended acoustic objectives and performs as expected in practical applications. Considerations will focus on the effects of temperature on 3D-

printed metamaterial prototypes, aiming to establish a relationship between acoustic performance and temperature variations. Furthermore, additional validation will be necessary to assess the effectiveness of metamaterials in real-world scenarios. Depending on the application context and feasibility, validation will be conducted through experimental measurements in a real-world setting. If this is not feasible, validation will be done in a simulated scenario. The block diagram shown in Figure 2.1 represents the workflow for the design, development, and implementation of acoustic metamaterials described in this chapter.

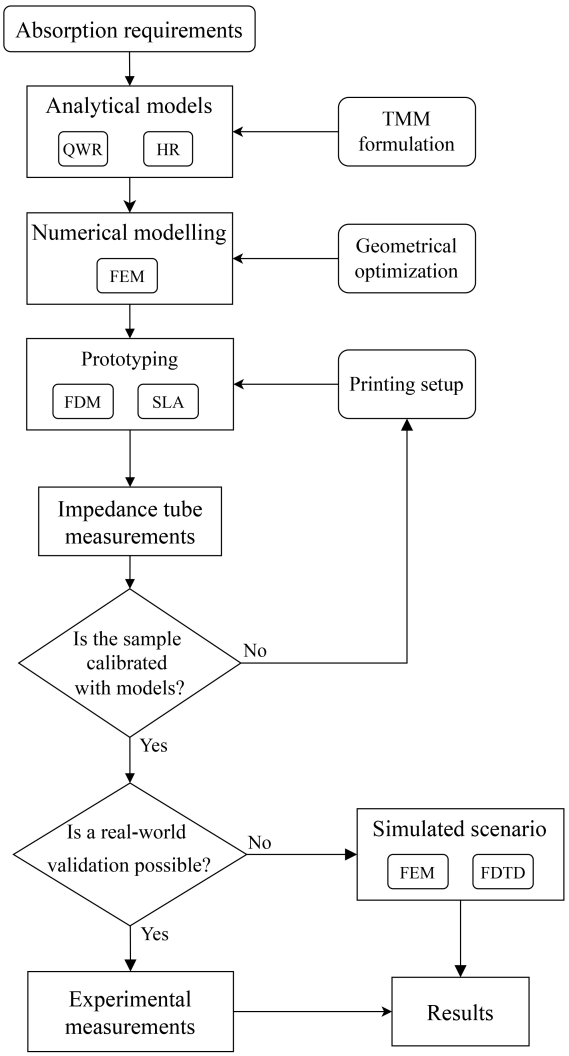


Fig. 2.1 Block diagram of the method used in the present thesis to develop acoustic metamaterials.

## 2.1 One-dimensional problems through the Transfer Matrix Method

The transfer matrix method serves as a straightforward yet robust analytical tool for simulating the propagation of acoustic waves in various one-dimensional scenarios [69]. Many practical acoustic issues can be simplified to one-dimensional cases by assuming plane-wave propagation. Recently, the transfer matrix method has found applications in modeling wave propagation in fluids, periodic structures, phononic crystals, and the analysis of acoustic metamaterials. It effectively characterizes wave dispersion and acoustic behaviors, such as reflection and transmission, in multilayer structures. This approach can also be employed to determine the effective parameters of resonant metamaterials and can readily account for thermo-viscous and viscoelastic losses. Consequently, the transfer matrix method has been utilized to design and evaluate efficient or near-perfect metamaterial absorbers based on quarter-wavelength resonators, Helmholtz resonators. One of the notable advantages of the transfer matrix method is its ability to provide swift calculations for complex acoustic structures, such as waveguide structures side-loaded by resonators or multi-layered systems.

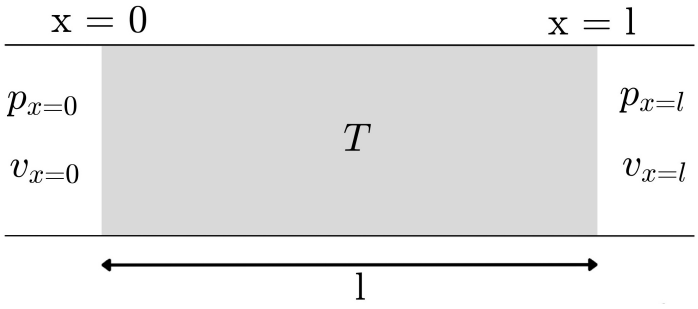


Fig. 2.2 Graphical representation of the Transfer Matrix Method applied to a single fluid layer.

Under the assumption of a plane wave propagating through a medium in the x-direction, the transfer matrix T relates the pressure and particle velocity at the beginning and end of a duct. In connection with the figure, it can be expressed:

$$\begin{bmatrix} p \\ v_x \end{bmatrix}_0 = T \begin{bmatrix} p \\ v_x \end{bmatrix}_l = \begin{bmatrix} T_{11} & T_{12} \\ T_{21} & T_{22} \end{bmatrix} \begin{bmatrix} p \\ v_x \end{bmatrix}_l \tag{2.1}$$

For an incident wave on a fluid, the pressure and particle velocity can be defined as:

$$p|_x = Ae^{-ikx} + Be^{ikx} \qquad v|_x = \frac{1}{Z}(Ae^{-ikx} - Be^{ikx}) \tag{2.2}$$

where A and B are the amplitudes of the incident and reflected waves, respectively. At the point *x=0*, and at the point *x=l*, they can be described:

$$p|_{x=0} = A + B, \qquad p|_{x=l} = (A+B)\cos(kl) - i(A-B)\sin(kl); \tag{2.3}$$

$$v|_{x=0} = \frac{1}{Z}(A-B), \qquad v|_{x=l} = \frac{1}{Z}[(A-B)\cos(kl) - i(A+B)\sin(kl)] \tag{2.4}$$

Combining the previous equations yields th expression:

$$p|_{x=l} = \cos(kl)p(0) - iZ\sin(kl)v(0); \tag{2.5}$$

$$v|_{x=l} = \cos(kl)v(0) - i\frac{\sin(kl)}{Z}p(0); \tag{2.6}$$

The relationship between pressure and particle velocity at two points in a fluid in matrix form can be represented as:

$$\begin{bmatrix} p \\ v_x \end{bmatrix}_0 = \begin{bmatrix} \cos(kl) & iZ\sin(kl) \\ i\frac{1}{Z}\sin(kl) & \cos(kl) \end{bmatrix} \begin{bmatrix} p \\ v_x \end{bmatrix}_l = \begin{bmatrix} T_{11} & T_{12} \\ T_{21} & T_{22} \end{bmatrix} \begin{bmatrix} p \\ v_x \end{bmatrix}_l \tag{2.7}$$

In a complex, multilayered configuration, as depicted in Figure 2.3, the connection between the input and output pressures and the acoustic flux is derived by multiplying individual transfer matrices associated with each layer. The total transfer matrix of a

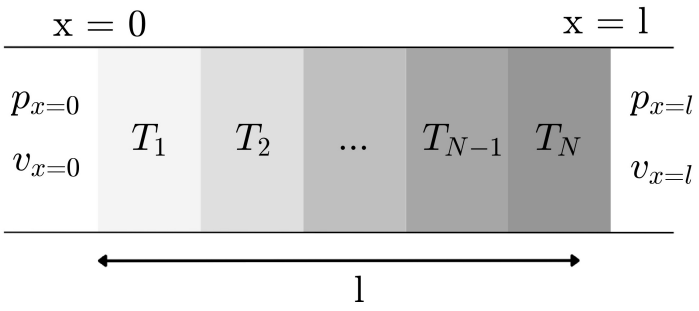


Fig. 2.3 Graphical representation of a multilayer fluid structure: the total matrix $T$ represents the characterization of the entire system.

multilayered acoustic structure is defined as the product of all the acoustic layers:

$$T = \prod_{n=1}^{N} T_n \tag{2.8}$$

where $N$ is the number of the layers.

### 2.1.1 Reflection

When a sound wave hits a uniform and infinite surface, some of the sound energy is reflected with a different amplitude and phase. The reflection coefficient is a function of the specific surface impedance, which is a complex quantity, and its value strongly depends on the frequency and the angle of the incident wave. The surface impedance quantifies how much sound pressure a given volume flow generates. In the case of a rigid boundary condition at position $x = L$, and considering equation 2.1 with the conditions $v|_{x=L} = 0$, it is possible to define the pressure and velocity following the relations:

$$p|_{x=0} = T_{11} p|_x; \tag{2.9}$$

$$v|_{x=0} = T_{21} p|_x; \tag{2.10}$$

So the surface impedance of the systems $Z_s$ is then expressed by:

$$Z_s = \frac{p|_{x=0}}{v|_{x=0}} = \frac{T_{11}}{T_{21}} \tag{2.11}$$

According to 2.7, the surface impedance, for an effective fluid layer results in:

$$Z_s = -iZ\cot(kL) \tag{2.12}$$

The reflection coefficient $R$ is related to the pressure and velocity at $x = 0$ and is defined as:

$$p|_{x=0} = 1 + R^{-}; \tag{2.13}$$

$$v|_{x=0} = \frac{1 - R^{-}}{Z_0}; \tag{2.14}$$

where $Z_0$ is the characteristic impedance of the air. The reflection coefficient can be defined by combining all the previous equations:

$$R = \frac{T_{11} - T_{21}Z_0}{T_{11} + T_{21}Z_0}; \tag{2.15}$$

Consequently, the absorption coefficient can be defined as:

$$\alpha = 1 - |R|^2 \tag{2.16}$$

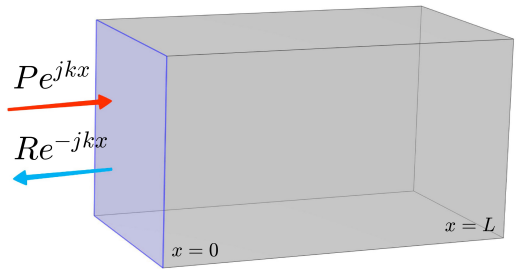


Fig. 2.4 2D sketch of the definitions of incoming and outgoing waves for 1D reflection problem.

### 2.1.2 Transmission

When a layer of material is surrounded by a fluid on both sides, the problem becomes a so-called transmission problem: assuming an incident pressure wave, a portion of the wave will be reflected, a portion will be absorbed, and a portion will be transmitted from one side of the material to the other. The equations 2.1 become:

$$p|_{x=0} = T_{11}p|_{x=L} + T_{12}v|_{x=L}; \tag{2.17}$$

$$v|_{x=0} = T_{21}p|_{x=L} + T_{22}v|_{x=L}; \tag{2.18}$$

Considering the propagation of the incident plane wave in the positive direction, it is possible to define the pressure and velocity at points $x = 0$ and $x = L$ in terms of the

reflection and transmission coefficients:

$$p|_{x=0} = 1 + R^{-}; \qquad p|_{x=L} = T^{-} e^{ikL}; \tag{2.19}$$

$$v|_{x=0} = \frac{1 - R^{-}}{Z_0}; \qquad v|_{x=L} = \frac{T^{-} e^{ikL}}{Z_L}; \tag{2.20}$$

If the medium on both sides is the same, it results $Z_0 = Z_L = \rho_0 c_0$. In case of a wave

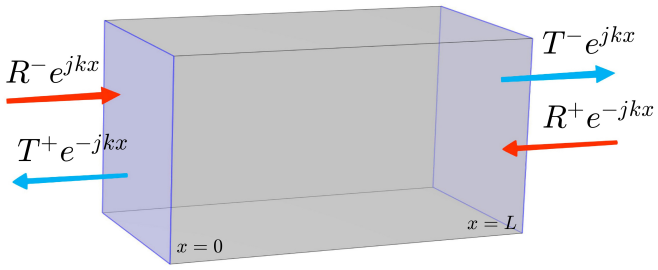


Fig. 2.5 2D sketch of the definitions of incoming and outgoing waves for 1D transmission problem, in function of the transmission and reflection coefficient

propagating in the negative direction, the pressure and flow velocity can be defined as:

$$p|_{x=0} = T^{+} e^{ikL}; \qquad p|_{x=L} = 1 + R^{-}; \tag{2.21}$$

$$v|_{x=0} = -\frac{T^{+} e^{ikL}}{Z_0}; \qquad v|_{x=L} = \frac{1 - R^{-}}{Z_L}; \tag{2.22}$$

Combining all the previous equations, and considering the same fluid on both side, the transmission coefficients for both propagations direction can be defined as:

$$T^{-} = \frac{1 + R^{-}}{T_{11} + T_{12}/Z_0}; \tag{2.23}$$

$$T^{-} = \frac{1 - R^{-}}{T_{21} Z_0 + T_{22}}; \tag{2.24}$$

$$T^{+} = T_{11}(1 + R^{+}) + \frac{T_{12}}{Z_0}(R^{+} - 1); \tag{2.25}$$

$$T^{+} = -T_{21} Z_0 (1 + R^{+}) - T_{22}(R^{+} - 1); \tag{2.26}$$

The equations 2.23, 2.24, 2.25, 2.26 can be rewritten to obtain the tranmission coefficient and the reflection coefficients as:

$$T^- = \frac{2e^{ikL}}{T_{11} + T_{12}/Z_0 + T_{21}Z_0 + T_{22}} \tag{2.27}$$

$$T^+ = \frac{2e^{ikL}(T_{11}T_{22} - T_{12}T_{21})}{T_{11} + T_{12}/Z_0 + T_{21}Z_0 + T_{22}} \tag{2.28}$$

$$R^- = \frac{T_{11} + T_{12}/Z_0 - T_{21}Z_0 - T_{22}}{T_{11} + T_{12}/Z_0 + T_{21}Z_0 + T_{22}} \tag{2.29}$$

$$R^+ = \frac{-T_{11} + T_{12}/Z_0 - T_{21}Z_0 + T_{22}}{T_{11} + T_{12}/Z_0 + T_{21}Z_0 + T_{22}} \tag{2.30}$$

**Reciprocal systems**

A reciprocal system occurs when the transmission does not depend on the direction of the incident wave. Mathematically, it means that the determinant of the transfer matrix is defined as:

$$T_{11}T_{22} - T_{12}T_{21} = 1 \tag{2.31}$$

In case of a reciprocal system, $T^- = T^+ = T$. Generally, acoustic structures, whether traditional materials or metamaterials, exhibit thermo-viscous losses, causing a portion of the energy to be absorbed. The absorption coefficient $\alpha$ provides an estimate of the dissipation due to intrinsic losses and depends on the direction of wave propagation. It is defined, for positive propagation and negative propagation, respectively, as:

$$\alpha^- = 1 - |R^-|^2 - |T|^2 \tag{2.32}$$

$$\alpha^+ = 1 - |R^+|^2 - |T|^2 \tag{2.33}$$

**Symmetrical systems**

Another simplification can be introduced in the case of a symmetric system, that is, when there is symmetry with respect to the midpoint. In this case, the transfer matrix has the following property: $T_{11} = T_{22}$. This implies that the reflection coefficient and consequently the absorption coefficient are independent of the direction of propagation considered. Therefore, the absorption coefficient can be written as:

$$\alpha^- = \alpha^+ = 1 - |R|^2 - |T|^2 \tag{2.34}$$

### Transmission Loss

In the acoustic context, transmission loss refers to the measure of the reduction in acoustic energy when a sound wave propagates through a material or a structure and is often used to assess the effectiveness of a material in blocking or attenuating the passage of sound. The Transmission Loss (TL) can be defined in logarithmic scale, in function of the transmission coefficient (T) as:

$$TL = -10\log|T|^2 \tag{2.35}$$

## 2.2 Wave propagation in ducts

For the purposes of this thesis, waveguides, cavities, and wave propagation in ducts with variable cross-sections will be considered. Consequently, the so-called flow formulation [69] is preferable to considering the formulation through particle velocity, as introduced earlier. In this formulation, fluid layers within the ducts are considered and defined, taking into account the variable sections in defining the characteristic impedances of the various layers. At each section discontinuity, some of the sound energy is reflected. In this context, it is necessary to introduce the definition of flow across a cross-section $S$ instead of using particle velocity.

$$V_x = Sv_x \tag{2.36}$$

Equation 2.1 changes and now relates the pressure and flow at the inlet and outlet of a duct of length L (Figure) as:

$$\begin{bmatrix} p \\ V_x \end{bmatrix}_0 = \begin{bmatrix} \cos(kl) & iZ'\sin(kl) \\ i\frac{1}{Z'}\sin(kl) & \cos(kl) \end{bmatrix} \begin{bmatrix} p \\ V_x \end{bmatrix}_l = \begin{bmatrix} T_{11} & T_{12} \\ T_{21} & T_{22} \end{bmatrix} \begin{bmatrix} p \\ V_x \end{bmatrix}_l \tag{2.37}$$

where $Z^{'} = Z/S$ is called normalized impedance, and $S$ is the cross-section of the duct. The characteristic impedance $Z$ and the characteristic wavenumber $k$ can be expressed as a function of the effective parameters, the effective density $\rho$ and bulk modulus $K$.

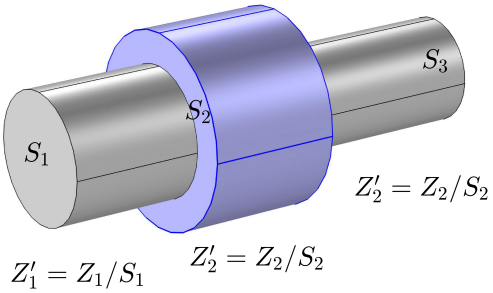


Fig. 2.6 3D sketch of a duct with three variable cross sections: the normalized impedances are defined for each different cross-sectional layer $S_1, S_2, S_3$.

### Effective parameters

When sound propagates through structures and geometries of reduced dimensions, such as QWRs or HRs, the sound waves attenuate due to thermal and viscous losses [70]. Specifically, these losses manifest in the acoustic thermal and viscous boundary layers near the surfaces. Recognizing this established phenomenon is imperative for evaluating the influence of these losses on acoustic systems. This understanding is essential to construct accurate models that align with experimental measurements. The thermo-viscous losses in small ducts of different cross-sections can be modeled employing a suitable complex characteristic impedance and wavenumber that are functions of the effective density $\rho$ and compressibility $C$:

$$Z(\omega) = \sqrt{\frac{\rho(\omega)}{C(\omega)}} \tag{2.38}$$

$$k(\omega) = \frac{\omega}{\sqrt{C(\omega)\rho(\omega)}} \tag{2.39}$$

In the case of rectangular ducts, two constants can be defined to find the general solution of the two-dimensional wave equation [70]:

$$\alpha_k = (k+\frac{1}{2})\pi/a \quad \beta_n = (n+\frac{1}{2})\pi/b \tag{2.40}$$

being $a$, $b$ the half-width and the half-height of the rectangular cross-section, and $k$, $n$ the indexes of all the terms that satisfy the boundary conditions. In the case of square sections, relevant to this thesis, the relationship $a = b$ holds. The effective density, $\rho(\omega)$, and compressibility, $C(\omega)$, are constitutional wave variables of the

tube, and can be defined according to visco-thermal acoustic theories [70]:

$$\rho(\omega) = \rho_0 \frac{a^2 b^2}{4i\omega} \left( \sum_{k=0}^{N} \sum_{n=0}^{N} [\alpha_k^2 \beta_n^2 (\alpha_k^2 + \beta_n^2 + \frac{i\omega}{v})] \right)^{-1} \tag{2.41}$$

$$C(\omega) = \frac{1}{P_0} \left[ 1 - \frac{4i\omega(\gamma-1)}{v' a^2 b^2} \left( \sum_{k=0}^{N} \sum_{n=0}^{N} [\alpha_k^2 \beta_n^2 (\alpha_k^2 + \beta_n^2 + \frac{i\omega\gamma}{v'})] \right) \right]^{-1} \tag{2.42}$$

where $\rho_0$ is the air density, $v$ is the air kinematic viscosity, $P_0$ is the equilibrum pressure of air, $v'$ is the air thermal diffusivity, $\gamma$ is the heat capacity ratio in air.

In case of cylindrical ducts, two functions $G_\rho(\omega)$ and $G_K(\omega)$ can be defined to express the complex and frequency-dependent mass density and bulk modulus as follows [70]:

$$G_\rho(\omega) = \sqrt{\frac{i\omega\rho_0}{\eta}} \tag{2.43}$$

$$G_K(\omega) = \sqrt{\frac{i\omega Pr\rho_0}{\eta}} \tag{2.44}$$

where $Pr$ is the Prandtl number, $\eta$ is the dynamic viscosity and $\rho_0$ the density of the fluid. The complex mass density and bulk modulus to account the thermal and viscous losses in cylindrical ducts can be written, respectively, as:

$$\rho(\omega) = \rho_0 \left[ 1 - \frac{2}{rG_p(\omega)} \frac{J_1(rG_\rho(\omega))}{J_0(rG_\rho(\omega))} \right]^{-1} \tag{2.45}$$

$$K(\omega) = K_0 \left[ 1 + \frac{2(\gamma-1)}{rG_K(\omega)} \frac{J_1(rG_K(\omega))}{J_0(rG_K(\omega))} \right]^{-1} \tag{2.46}$$

where $r$ is the radius of the duct, $J_n$ is the Bessel function of the first kind and order $n$, and $K_0 = \gamma P_0$ is the adiabatic bulk modulus with $P_0$ the static pressure.

### End corrections

In acoustics, end corrections are adjustments made to the effective length of a resonator to account for which differs from its physical length due to the presence of open ends. These corrections are because acoustic theory assumes that airflow terminates on a flat surface, but in reality, openings or section transitions can alter the acoustic behavior. They are crucial for accurately describing the analytical models when a section change occurs, creating a discontinuity [71]. Considering

airflow through an opening, the pressure distribution around the opening is not flat. The presence of the opening introduces pressure gradients, and the air pressure can vary significantly in the area surrounding the opening. The pressure variation is particularly noticeable near the edges and influences sound propagation.

An example could be the discontinuity produced between a waveguide and the Helmholtz resonator's neck or the neck itself and cavity, as shown in Figure 2.7a. For

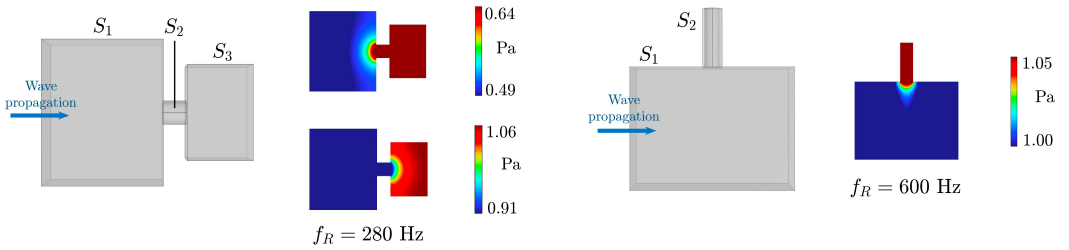


a) Change of section b) Side branch

Fig. 2.7 a) Drawing of the change of section in a Helmholtz resonator: the distribution of the sound pressure $p$ is highlighted for the discontinuity between the waveguide and the neck, and between the neck and the cavity. b) Drawing of a side branch: the distribution of the sound pressure $p$ is highlighted for the discontinuity between the waveguide and the QWR

in-line elements, locally resonators can be considered in series in a main waveguide.

If a waveguide is in series with one or more resonators, resulting in a constricted wave propagation section, it is necessary to use an end correction [69]. This correction can be modeled by adding a subwavelength fluid matrix of length $\Delta L$, which is a function of the ratio between the waveguide and resonator cross-sections and is defined as follows:

$$\Delta L = 0.82\left[1 - 1.35\Phi + 0.31(\Phi)^3\right]2a \tag{2.47}$$

where $2a$ is the side of the side of the resonator, and $\Phi$ is the ratio of the side of the resonator and the side of the waveguide

In case of a discontinuity when a resonator is loaded in parallel to a main waveguide, as shown in Figure 2.7b, the length of the end correction $\Delta L$ is defined as:

$$\Delta L = 0.82\left[1 - 0.235\Phi - 1.32(\Phi)^2 + 1.54(\Phi)^3 - 0.86(\Phi)^4\right]2a \tag{2.48}$$

The added equivalent fluid matrix is considered in series with the total transfer matrix, and is defined as:

$$M_{\Delta L} = \begin{bmatrix} 1 & Z_{\Delta L} \\ 0 & 1 \end{bmatrix} \tag{2.49}$$

The characteristic radiation impedance $Z_{\Delta L}$ is defined as:

$$Z_{\Delta L} = -i\omega\rho_0 \frac{\Delta L}{S} \tag{2.50}$$

where S is the section of the main waveguide.

### 2.2.1 Quarter Wavelength Resonator

In this section, the comprehensive analytical approach used to analyze the square-based quarter-wavelength resonator will be provided as an understanding of its behavior and resonant frequencies. The square-based QWR is a four-sided cavity with each side of length $l$. At the closed end of the resonator ($x = 0$), the following

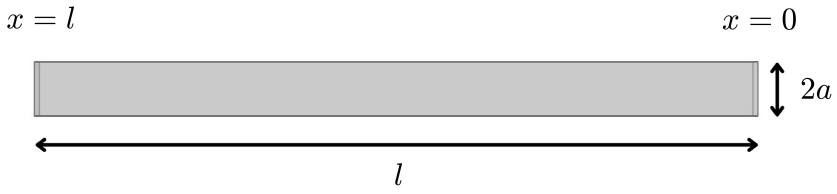


Fig. 2.8 2D sketch of a squared base QWR. At position $x = 0$, the resonator exhibits the closed end, and at position $x = l$ is the open end.

boundary condition can be imposed:

$$\frac{\partial p}{\partial x}(0,y) = 0 \quad \text{for} \quad 0 \leq y \leq 2a \tag{2.51}$$

This condition represents the perfect reflection of the acoustic waves at the closed end. At the open end of the resonator ($x = l$), we have the following boundary condition:

$$p(l,y) = 0 \quad \text{for} \quad 0 \leq y \leq 2a \tag{2.52}$$

This condition signifies zero pressure gradient at the open end, simulating an open boundary. The input impedance of the Quarter Wavelength resonator can be derived

by relating the pressure and the velocity at the beginning, $x = 0$, and at the end $x = l$, using the TMM formulation described in Section 2.2:

$$\begin{bmatrix} p \\ V_x \end{bmatrix}_0 = \begin{bmatrix} \cos(k_f l) & iZ_n{}' \sin(k_f l) \\ i\frac{1}{Z_n{}'} & \cos(k_f l) \end{bmatrix} \begin{bmatrix} p \\ V_x \end{bmatrix}_l \tag{2.53}$$

This analytical expression of the input impedance at the open boundary can be defined as:

$$Z_{in} = -iZ_f^{'} \cot(k_f l) = -i\frac{Z_f}{S_f} \cot(k_f l) \tag{2.54}$$

where $Z_f$ is the characteristic impedance inside the material, $S_f$ is the cross-section area of the resonator, $k_f$ the characteristic wavenumber.

Consequently, the characteristic impedance and the characteristic wavenumber can be derived as a function of the effective mass $\rho(\omega)$ and the compressibility $K(\omega)$ described in 2.41 and 2.42 for rectangular cross-sections, as follows:

$$Z_f(\omega) = \sqrt{\frac{\rho(\omega)}{K(\omega)}} \tag{2.55}$$

$$k_f(\omega) = \frac{\omega}{\sqrt{K(\omega)\rho(\omega)}} \tag{2.56}$$

The expression of Eq. 2.57 does not consider the pressure gradient surrounding the opening of the QWR. The end correction, expressed in Eq. 2.47 or 2.48 should be accounted to the characteristic impedance to consider the radiation of the resonator in the main waveguide through the use of a modelled fluid transfer matrix of length $\Delta L$:

$$\begin{bmatrix} p \\ V_x \end{bmatrix}_0 = \begin{bmatrix} \cos(k_0 \Delta L) & iZ_0{}' \sin(k_0 \Delta L) \\ i\frac{1}{Z_0{}'} \sin(k_f \Delta L) & \cos(k_0 \Delta L) \end{bmatrix} \begin{bmatrix} \cos(k_f l) & iZ_n{}' \sin(k_f l) \\ i\frac{1}{Z_n{}'} \sin(k_f l) & \cos(k_f l) \end{bmatrix} \begin{bmatrix} p \\ V_x \end{bmatrix}_l \tag{2.57}$$

wheere $k_0$ is the wavenumber of the main waveguide, $Z_0' = Z_0/S$ is the characteristic impedance of the waveguide and $S$ is the section of the waveguide. The input impedance of the QWR in series with a main waveguide with end correction, taking into account 2.54 and 2.47 is defined as:

$$Z_{in} = -i\frac{Z_f}{S_f} \cot(k_f l) - i\omega\rho_0 \frac{\Delta L}{S} \tag{2.58}$$

where S is the section of the main waveguide, and $\phi$ is the ratio of the side the QWR and the side of the waveguide.

### 2.2.2 Helmholtz Resonator

In this study, Helmholtz resonators with necks and cavities featuring a square base will be employed, similar to the one depicted in Figure 2.9. The square-based Helmholtz resonator operates on the principle of using a cavity with a square cross-section to absorb sound energy at a specific target frequency effectively. It surpasses the quarter-wave mechanism by exploiting the unique geometry of the square cross-section to create a resonance effect at the desired frequency. The key to its function lies in the surface impedance of the resonator, which considers effective parameters. This section provides a detailed analytical method for examining the square-based

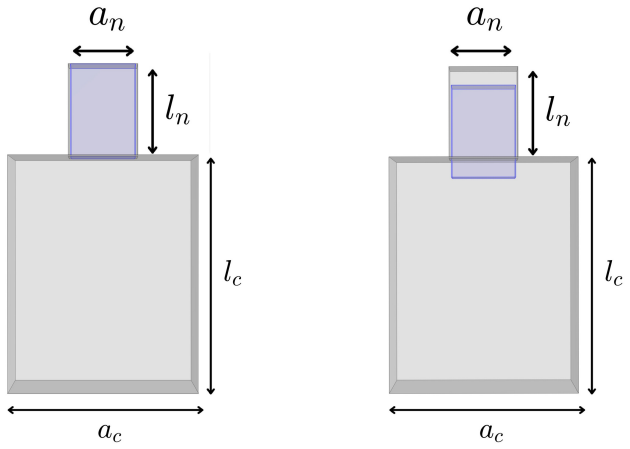


Fig. 2.9 2D sketch of a square-based Helmholtz resonator: the moving mass inside the neck is highlighted in blue. During the resonance, a variation in the volume of air and pressure within the cavity happens.

Helmholtz resonator. This method is crucial for understanding its behavior and identifying its resonant frequencies.

The square-based Helmholtz resonator is composed of a square-sectional cavity of side $a_c$ and length $l_c$ and a square-sectional neck of side $a_n$ and length $l_n$. At the closed end of the cavity ($x = 0$), the following condition represents the complete reflection of the acoustic waves at the closed end:

$$\frac{\partial p}{\partial x}(0,y) = 0 \quad \text{for} \quad 0 \leq y \leq a_c \tag{2.59}$$

At the open end of the resonator ($x = l_n + l_c$), the boundary condition is defined as follows:

$$p(x,y) = 0 \quad \text{for} \quad 0 \leq y \leq a_n \tag{2.60}$$

This condition signifies a zero pressure gradient at the open end, effectively simulating an open boundary. The input impedance of the Helmholtz resonator can be derived by relating the pressure and the velocity at the beginning, $z = 0$, and at the end $z = l = l_n + l_c$, using the TMM formulation described in Section 2.2:

$$\begin{bmatrix} p \\ V_x \end{bmatrix}_0 = \begin{bmatrix} \cos(k_n l_n) & iZ_n{}' \sin(k_n l_n) \\ i\frac{1}{Z_n{}'} \sin(k_n l_n) & \cos(k_n l_n) \end{bmatrix} \begin{bmatrix} \cos(k_c l_c) & iZ_c{}' \sin(k_c l_c) \\ i\frac{1}{Z_c{}'} \sin(k_c l_c) & \cos(k_c l_c) \end{bmatrix} \begin{bmatrix} p \\ V_x \end{bmatrix}_l \tag{2.61}$$

where $k_n$ and $k_c$ are the effective wave number inside the neck and the cavity, respectively, and $Z_n{}' = Z_n/S_n$ and $Z_c{}' = Z_c/S_c$, the normalized effective impedance of the neck and the cavity, respectively, $S_n$ the cross-section of the neck and $S_c$ the cross-section of the cavity. According to Eq. 2.41, 2.42, the effective parameters are calculated to consider the thermo-viscous losses inside the neck and the cavity, respectively:

$$Z_n(\omega) = \sqrt{\frac{\rho_n(\omega)}{K_n(\omega)}} \tag{2.62}$$

$$k_n(\omega) = \frac{\omega}{\sqrt{K_n(\omega)\rho_n(\omega)}} \tag{2.63}$$

$$Z_c(\omega) = \sqrt{\frac{\rho_c(\omega)}{K_c(\omega)}} \tag{2.64}$$

$$k_c(\omega) = \frac{\omega}{\sqrt{K_c(\omega)\rho_c(\omega)}} \tag{2.65}$$

Then, the impedance of the HR is defined as:

$$Z_{HR} = \frac{p(0)}{V_x(0)} = -iZ_n{}' \frac{Z_c{}'/Z_n{}' - \tan(k_n l_n)\tan(k_c l_c)}{Z_c{}'/Z_n{}' \tan(k_n l_n) + \tan(k_c l_c)} \tag{2.66}$$

Taking into account the consideration of the end corrections, the pressure radiation between the elements of the HR can be modeled as:

$$\begin{bmatrix} p \\ V_x \end{bmatrix}_0 = \begin{bmatrix} \cos(k_n \Delta L_2) & iZ_n{}' \sin(k_n \Delta L_2) \\ i\frac{1}{Z_n{}'} \sin(k_n \Delta L_2) & \cos(k_n \Delta L_2) \end{bmatrix} \begin{bmatrix} \cos(k_n l_n) & iZ_n{}' \sin(k_n l_n) \\ i\frac{1}{Z_n{}'} \sin(k_n l_n) & \cos(k_n l_n) \end{bmatrix} \tag{2.67}$$

$$\begin{bmatrix} \cos(k_n \Delta L_1) & iZ_n{}' \sin(k_n \Delta L_1) \\ i\frac{1}{Z_n{}'} \sin(k_n \Delta L_1) & \cos(k_n \Delta L_1) \end{bmatrix} \begin{bmatrix} \cos(k_c l_c) & iZ_c{}' \sin(k_c l_c) \\ i\frac{1}{Z_c{}'} \sin(k_c l_c) & \cos(k_c l_c) \end{bmatrix} \begin{bmatrix} p \\ V_x \end{bmatrix}_l \tag{2.68}$$

where $\Delta L_2$ and $\Delta L_1$ are the length corrections due to the pressure radiation at the discontinuity from a principal waveguide and the neck and at the discontinuity from the neck to the cavity, respectively. Their expression can be found at Eq. 2.47 and 2.48. Consequently, a more accurate expression that has been used to develop the characteristic impedance $Z_{HR}$ of an HR can be expressed, considering the end corrections, as:

$$Z_{HR} = -iZ_n{}' \frac{\cos(k_n l_n)\cos(k_c l_c) - \frac{k_n \Delta L Z'_n}{Z'_c}\cos(k_n l_n)\sin(k_c l_c) - \frac{Z'_n}{Z'_c}\sin(k_n l_n)\sin(k_c l_c)}{\sin(k_n l_n)\cos(k_c l_c) - \frac{k_n \Delta L Z'_n}{Z'_c}\sin(k_n l_n)\sin(k_c l_c) - \frac{Z'_n}{Z'_c}\cos(k_n l_n)\sin(k_c l_c)} \tag{2.69}$$

where $\Delta L = \Delta L_1 + \Delta L_2$ is the total addition of the two correction lengths [69].

### 2.2.3 Multi-resonant systems

QWR and HR are selective elements with a very narrow absorption band, limited to a single frequency. When the goal is to absorb multiple frequencies, or even a broadband range of frequencies, configurations with multiple resonators in parallel can be designed. By leveraging the definitions used by TMM, it is possible to analytically develop multi-resonator systems based on the individual characteristic impedances of each element. As described in [31], supposing to insert $n$ resonators in parallel, the total characteristic impedance will be defined as:

$$Z_{tot} = \sum_{n=1}^{N} \frac{1}{Z'_{f_n}} \tag{2.70}$$

where $Z'_{f_n}$ is the characteristic impedance of the n-th resonator. All the resonators can be critically coupled and loaded to a closed waveguide. Eq. 2.70 holds under the assumption that sound pressure and the particle velocity of the reflected waves

from the surface are uniform on any neighboring surface parallel to the surface since distances between the resonator are of subwavelength scale. In case distances between the resonator become longer or the incident wave frequency becomes higher, the local sound pressure and particle velocity would differ on the neighboring surface [72, 73]. Moreover, higher-order resonances of the resonators, which become numerous as frequency increases, can represent an advantage when broadband absorption is required.

## 2.3 Numerical modelling

This study's numerical simulations were performed using the COMSOL Multiphysics software [74]. COMSOL is a commercial software employing the Finite Element Method (FEM) to solve the wave equation. The FEM is a numerical technique that addresses partial differential equations in 1D, 2D, and 3D. Specifically, the considered geometries are discretized into a finite number of small domain subdivisions called elements. All elements are interconnected through singular points known as nodes. The system formed by nodes and elements constitutes the so-called mesh, the geometric unit where the equation under consideration is solved. A global solution is derived from solving individual cells, and interpolation is employed to determine a continuous solution across the entire domain. Specifically, the pressure acoustics

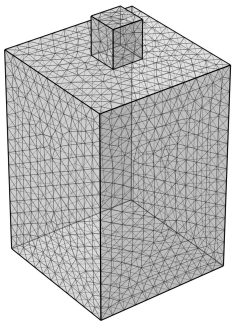

Fig. 2.10 3D sketch of the discretization of a Helmholtz resonator's domain in Comsol Multiphysics: the volume corresponding to the elements is composed by mesh, in which the wave equation is solved.

module in the frequency domain was utilized. Consequently, in the numerical models,

the governing equation is the Helmholtz equation, described by the expression:

$$\nabla(-\frac{1}{\rho_c}\nabla p_0) - \frac{k_{eq}^2 p_0}{\rho_c} = 0 \tag{2.71}$$

considering a harmonic pressure wave excitation, $p = p_0 e^{i\omega t}$, $k_{eq}$ as the equivalent wavenumber, defined considering the effective parameters, $\rho_c$ is the complex dynamic density. All the rigid surfaces of the domain are generally modeled as sound-hard boundaries, considering the Neumann boundary conditions:

$$\vec{n} \cdot (-\frac{1}{\rho_c}\nabla p_0) = 0 \tag{2.72}$$

where $\vec{n}$ is the normal vector at the boundaries.

The model's accuracy depends on the size of the discretization elements, known as the mesh. To model acoustic systems of this work, the maximum element size has been fixed to be at least six times smaller than the smallest wavelength considered relative to the maximum frequency in the model. This ensures the correctness of results for high frequencies without assuming any overlooked approximations due to excessively large mesh size and without achieving the so-called convergence of the model. On the other hand, the smaller the mesh elements of the system, the higher the computational processing cost. For this reason, it is advisable to seek a compromise where convergence is achieved and the system does not exhibit overly detailed geometry, which might be unnecessary for this study. Moreover, the number

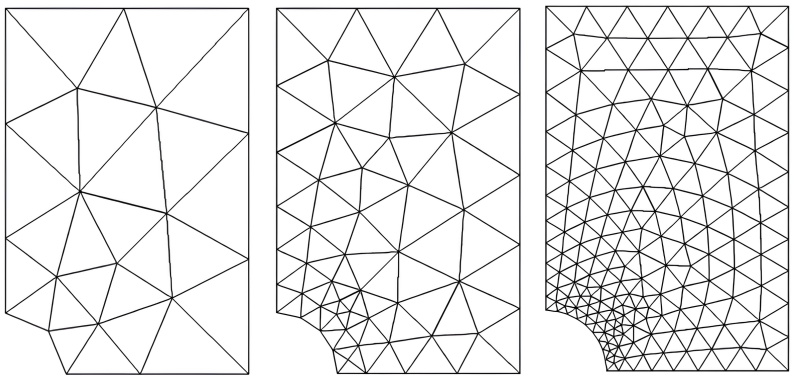

Fig. 2.11 The mesh fitting is increased at critical geometries or near sources or domain property changes.

of mesh elements has been increased near critical geometry features or particularly

small elements, such as around holes or at the boundary between two materials, as shown in Figure2.11. In practice, adaptive mesh refinement and practical adjustments have been set to enhance the mesh quality of a domain.

### 2.3.1 Narrow region for thermo-viscous losses

Since this study involves the development of metamaterials based on Helmholtz resonators and quarter-wavelength resonators, it was necessary to consider the well-known effects of thermo-viscous losses in relatively small ducts. When sound propagates in structures and geometries with small dimensions, the sound becomes attenuated because of losses. Specifically, thermo-viscous losses occur in the viscous boundary layer near the walls. From a numerical perspective, the resonator cavities have been implemented in the models *Narrow regions*, where the equations describe the physics outlined analytically in the previous section, considering the expression of the effective parameters, the bulk modulus, and the mass density. This Narrow Region domain feature adds the losses associated with the acoustic boundary layers to the fluid in a homogenized way. The losses are derived analytically, in function of the geometry of the small duct or cavity under study, reducing the computational costs. The slit, circular or rectangular duct models are based on the so-called low-reduced frequency model, described in detail in [70, 75, 76].

### 2.3.2 Absorption method

The numerical methodology for characterizing metamaterials was carried out using Comsol Multiphysics. Figure 2.12 illustrates the schematic of the model used to determine the acoustic properties of a one-port system for calculating the reflection and absorption coefficients of a sample. A plane wave source is placed at one end of the waveguide, and the sample is positioned at the other end of the waveguide, followed by a rigid wall. The walls of the waveguide are also considered as ideal rigid walls. The volume of the waveguide is characterized in the model as the Background Pressure Field. This allows modeling the incident pressure wave to study the scattered pressure field. The scattered pressure is defined as the difference between the total acoustic pressure and the background pressure field. Both pressures are calculated at the receiver point indicated in figure 2.12.

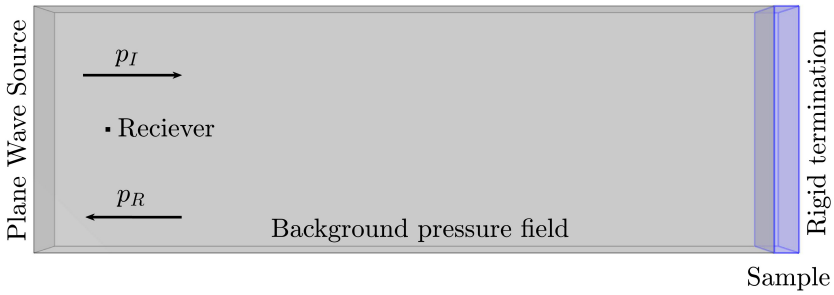


Fig. 2.12 Schematic drawing of the numerical model utilizing the background pressure field method to determine the reflection and absorption coefficients.

### 2.3.3 Transmission method

A two-port numerical model was developed to calculate the transmission coefficient. Unlike the model for absorption calculation, ideal plane wave radiation is applied at both ends of the waveguide, as shown in Figure 2.13. It was preferred to introduce a plane wave source at the second end rather than using the Perfect Matched Layer (PML) domain for lower computational costs. In this case as well, utilizing the background pressure field allowed the calculation of the scattered pressure field. Additionally, it is possible to calculate the value of the incident pressure at receiver position 2, located after the sample, to compute the transmitted acoustic wave and the subsequent transmission coefficient.

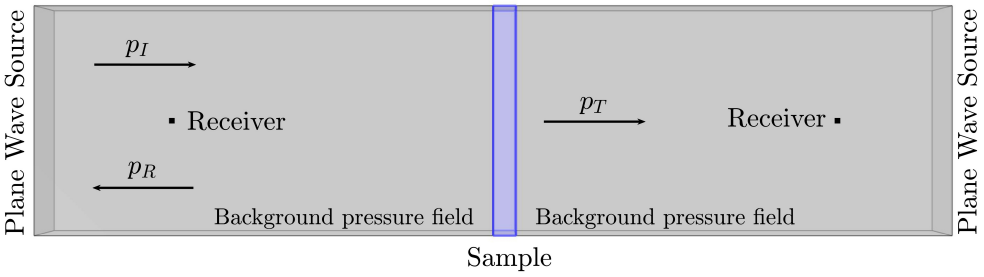


Fig. 2.13 Schematic drawing of the numerical model utilizing the background pressure field method to determine the reflection, absorption, and transmission coefficients.

## 2.4 3D printing and Prototyping

Acoustic metamaterials are usually studied analytically and numerically and then tested on prototypes. For this reason, 3D printing is becoming a popular way of quickly realizing AMMs' innovative and complex geometrical designs [77]. Despite this advantage, previous studies have demonstrated how the acoustic properties of metamaterial prototypes depend on printing parameters and quality [78, 32, 79]. Although rapid, these aspects must be validated and maintained at optimal levels. The quality of layers and the precision of geometries must be upheld to avoid mismatches between the analytical and numerical models through which they were designed and experimental measurements. To assess the connection between printing parameters and the absorbing properties of acoustic metamaterials, various printing models and setups were tested to replicate the acoustic properties of predictive models of a coiled-up quarter-wavelength resonator. The printing techniques considered in this study include Fused Deposition Modeling (FDM) for printing PETG samples and Stereophotography (SLA) for printing resin samples. This section will detail different

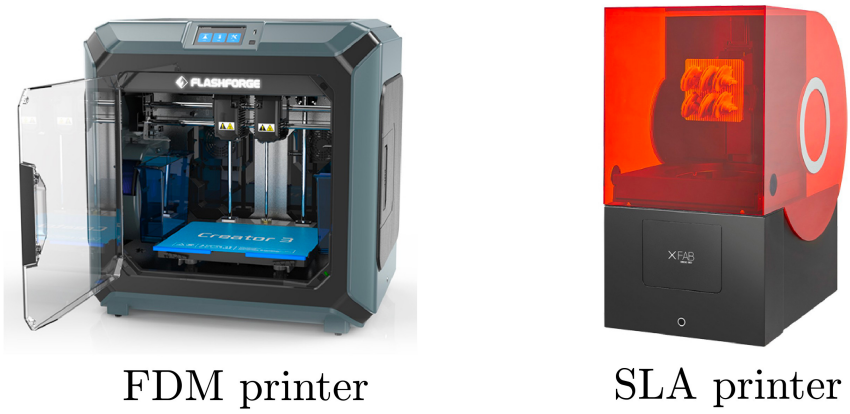


Fig. 2.14 Fuse Deposition Modeling printer and Stereolithography printer were used to print the samples in this study.

printing parameters used, and later, the setup used in the practical applications of the metamaterials presented in this study will be shown.

### 2.4.1 Fuse Deposition Modeling

Fused deposition modeling (FDM) is one of the most prevalent additive manufacturing technologies, chosen for its cost-effectiveness and the diverse range of

thermoplastic polymers available [80, 81, 78]. In FDM methods, specific material (PLA or PETG) filament is fused through a nozzle and deposited on the printing platform following specific geometry and layering inputs. In this study, all specimens were produced using FDM technology through a Flashforge Creator 3-D printer. The selected material was FormFutura HDglass specifically an amorphous polyethylene terephthalate glycol (PETG) blend. This filament was chosen for its suitable mechanical properties, including a high tensile modulus and strength.

### 2.4.2 Stereolithography

Stereolithography (SLA) is a 3D printing technique initially developed for precise technical prototyping in medical research and has garnered attention for its reproduction accuracy at the micron scale [82, 83]. Bio-engineering and engineering researchers have increasingly employed SLA, exploring its physical, mechanical, and environmental aspects [84–86]. SLA is a 3D printing process that utilizes the polymerization of photosensitive resins to create three-dimensional objects layer by layer. In this process, a laser or other light source selectively solidifies thin layers of liquid resin, gradually building up the final 3D-printed object. After the objects have been printed, it is common for residues of unpolymerized liquid resin to remain on the surface of the objects. Cleaning the samples usually involves using specific solvents that effectively remove the unpolymerized resin. After cleaning, the samples can be further cured through a process called post-curing, which ensures that all unpolymerized materials are completely removed and the objects are ready for use or further finishing. Generally, this 3D printing method is not the preferred prototyping method due to its higher cost, extensive post-processing requirements, and potential material toxicity issues. Despite its disadvantages, resin prototypes produced with SLA generally have a 100% filling density, as the resulting geometrical volumes are entirely solid, as shown in Figure 2.15. Furthermore, the speed and print quality do not significantly affect the accuracy of the final prototype and the resulting acoustic properties. The most significant variable for stereolithography remains the quality of the material used. Higher-quality resins obviously come at higher prices but ensure better printing accuracy in terms of low porosity and easier sample cleaning at the end of the printing process. For the purposes of this study, a printing speed of 30 seconds per layer and a layer resolution of 0.1 mm were used. These values were optimized to reproduce the expected acoustic performance of AMMs. The DWS X-FAB printer (see Figure 2.14) and INVICTA 977 (non-flexible) and TDS

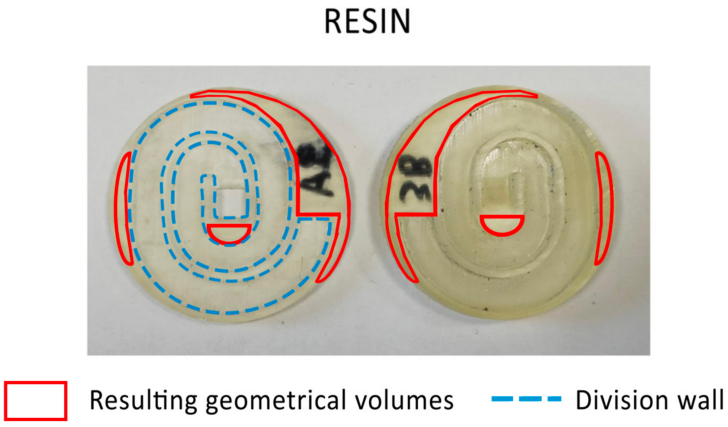


Fig. 2.15 Picture of the sectioned 3D printed prototypes in SLA-resin, cut in half to display the upper (left) and lower) resulting geometrical volumes (highlighted by the red lines) and the resonant volume wall's (blue lines) characterization can be observed.

IT - FLEXA693 (flexible) polymers were used. SLA resins are typically toxic, and post-processing materials pose fire hazards, necessitating proper safety measures and training for personnel managing the equipment.

Table 2.1 SLA printing parameters used in this study. Unlike FDM, the printing parameters were kept constant, without varying printing configurations.

| **SLA parameter** | **Value** |
|---|---|
| Printing speed $[s/layer]$ | 50 |
| Layer height $[mm]$ | 0.1 |
| Filling density of the geometrical voids $[\%]$ | 100 |

## 2.5 Impedance tube measurements

An impedance tube was employed to characterize the materials developed in this study. An impedance tube is a scientific apparatus designed to measure the acoustic properties of materials operating under controlled conditions. This instrument is utilized to determine various characteristics, such as the surface complex impedance, the acoustic reflection, transmission, and absorption coefficient of a specimen, within specific frequency ranges and under precisely controlled environmental conditions. The impedance tube operates within the range where the plane wave approximation

is valid, representing the controlled conditions for characterizing a sample, with the incidence of the acoustic pressure wave being normal. All measurements in the present work were performed using a square-based impedance tube according to ISO 10534-2 (1998) [87]. The square impedance tube has a side of 12 cm, providing results in the frequency range of 200 - 1200 Hz, where the plane wave assumptions are valid. The one-microphone method in two different locations was employed to assess the acoustic performance of the samples, specifically the normal incidence sound absorption coefficient, ensuring phase consistency between microphones. The measurement setup comprises a loudspeaker for signal generation, a signal amplifier (with a signal-to-noise ratio of 96dB), a power supply, a sound card, a single microphone, and a battery signal conditioner (output current 3 mA). The loudspeaker emits an exponential sine sweep, converted to an analog signal by the sound card's digital-to-analog converter (DAC). The pressure signals captured by the microphone undergo conversion to digital audio through an analog-to-digital converter, sampled at 92 kHz with a 24-bit depth to avoid dynamic gain issues. MATLAB [88] was employed for digital signal processing, based on the transfer-function method [89, 90].

### 2.5.1 Two-microphone method

The two-microphone method was employed to assess the acoustic performance of the samples, specifically the normal incidence sound absorption coefficient, ensuring phase consistency between using the same microphone in two microphone locations, as described in [87]. The idea is to determine the reflection coefficient by extracting the complex total acosutic pressure at the two microphone locations $x_1$ and $x_2$, as shown in Figure 2.16. The complex total pressures at the microphone locations are

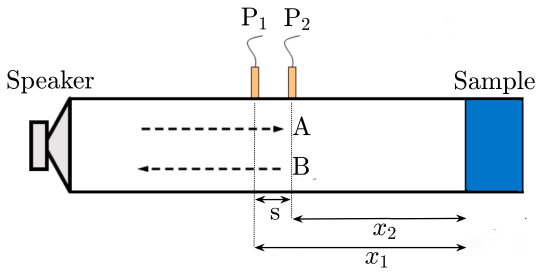


Fig. 2.16 Schematic diagram of the impedance tube for absorption measurements.

defined as:

$$p_1 = p_I(x_1) + p_R(x_1) = \hat{p_I} e^{-ikx_1} + \hat{p_R} e^{ikx_1} \tag{2.73}$$

$$p_2 = p_I(x_2) + p_R(x_2) = \hat{p_I} e^{ikx_2} + \hat{p_R} e^{-ikx_2} \tag{2.74}$$

where $\hat{p_I}$ and $\hat{p_R}$ are the amplitudes of the incident and reflected waves, respectively, $k$ is the wave number. Two transfer functions for incident and reflected waves can be defined as:

$$H_I = \frac{p_I(x_2)}{p_I(x_1)} = \frac{\hat{p_I} e^{-ikx_2}}{\hat{p_I} e^{ikx_1}} = e^{iks} \tag{2.75}$$

$$H_R = \frac{p_R(x_2)}{p_R(x_1)} = \frac{\hat{p_R} e^{ikx_2}}{\hat{p_R} e^{ikx_1}} = e^{-iks} \tag{2.76}$$

where $s = x_2 - x_1$ is the spacing between the microphone positions. The transfer function between the two pressure point positions can be defined as:

$$H_{12} = \frac{p_2}{p_1} = \frac{\hat{p_I} e^{-ikx_2} + \hat{p_R} e^{ikx_2}}{\hat{p_I} e^{-ikx_1} + \hat{p_R} e^{ikx_1}} \tag{2.77}$$

Combining equations 2.75, 2.76, 2.77, the reflection coefficient at the sample surface can be obtained as:

$$R = \frac{H_{12} - H_I}{H_R - H_{12}} e^{ik2s} \tag{2.78}$$

The absorption coefficient can be obtained from equation 2.78:

$$\alpha = 1 - |R|^2 \tag{2.79}$$

### 2.5.2 Four-microphone method

The method for measuring the transmission coefficient of a two-port system is based on the four-microphone method, as described in [90]. This experimental approach allows the use of the transfer matrix to obtain the reflection, the absorption, and the transmission coefficient, as depicted in the figure. In this case, there are two microphone positions before the sample and two microphone positions after the sample. The impedance tube can be used in the case of a non-symmetric system. This assumption relates to the definition of a non-symmetric system, as indicated in Equation , where $T_{11} = T_{22}$. A loudspeaker is mounted at one end of the tube, while the other has an ideally anechoic termination, as shown in Figure 2.17. The anechoic termination determines the asymmetry of the system and, consequently,

the acoustic properties based on the direction of wave propagation relative to the sample. The loudspeaker ensures the emission of a plane wave within the tube's

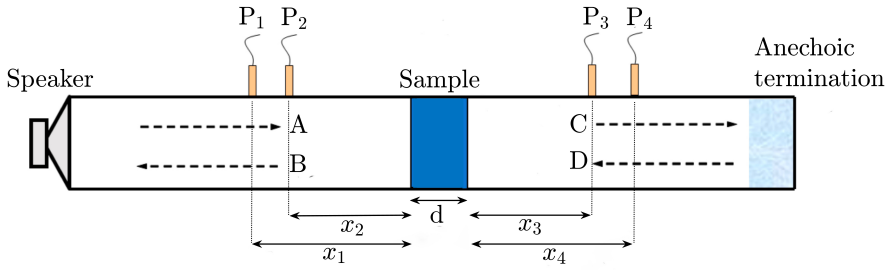


Fig. 2.17 Schematic diagram of the impedance tube for transmission measurements.

usable range, described by Equation x. In the case of the impedance tube used for the measurements in this thesis, the assumption of a plane wave is valid up to a frequency of $f_{cut} = 1200$ Hz According to Figure, it is possible to express the complex sound pressure at the four microphone locations as:

$$P_1 = (Ae^{-ikx_1} + Be^{ikx_1})e^{i\omega t} \tag{2.80}$$

$$P_2 = (Ae^{-ikx_2} + Be^{ikx_2})e^{i\omega t} \tag{2.81}$$

$$P_3 = (Ce^{-ikx_3} + De^{ikx_3})e^{i\omega t} \tag{2.82}$$

$$P_4 = (Ce^{-ikx_4} + De^{ikx_4})e^{i\omega t} \tag{2.83}$$

The amplitude coefficients $A, B, C, D$ can be defined by combining the complex acoustic pressure obtained from microphone locations $x_1, x_2, x_3, x_4$, as follows:

$$A = \frac{i(P_1 e^{ikx_2} - P_2 e^{ikx_1})}{2\sin k(x_1 - x_2)} \tag{2.84}$$

$$B = \frac{i(P_2 e^{-ikx_1} - P_1 e^{-ikx_1})}{2\sin k(x_1 - x_2)} \tag{2.85}$$

$$C = \frac{i(P_3 e^{ikx_4} - P_4 e^{ikx_3})}{2\sin k(x_3 - x_4)} \tag{2.86}$$

$$D = \frac{i(P_4 e^{-ikx_1} - P_3 e^{-ikx_1})}{2\sin k(x_3 - x_4)} \tag{2.87}$$

By measuring the acoustic pressure at the four microphone positions shown in the figure, the following calculations can be used to determine a sample's reflection and

transmission coefficients, for a symmetrical and reciprocal case:

$$R = \frac{(B \cdot A) - (C \cdot D)}{A^2 - D^2} \tag{2.88}$$

$$T = \frac{(B \cdot D) - (C \cdot A)}{D^2 - A^2} \tag{2.89}$$

Consequently, the sound absorption coefficient can be expressed as:

$$\alpha = 1 - |R|^2 - |T|^2 \tag{2.90}$$

## 2.6 Optimization of 3D printing setups

The prototyping of acoustic metamaterials remains a focal point for real-world applications. Analytical and numerical models, while of great value in the design phase, often make simplifications and do not fully consider the complexity of acoustic, vibrational, and structural phenomena that are frequently present when wave propagation in materials is considered. During the design phase, it is crucial to establish as strong a connection as possible between predictive models and experimental measurements obtained from samples produced using various manufacturing methods. For the purposes of this thesis, 3D prototyping through FDM and SLA has been considered. On one hand, for SLA, optimization primarily concerns the choice of the material used for printing and the accuracy of the post-processing phase. On the other hand, for FDM, it is necessary to optimize the printing parameters and setups to achieve calibration between analytical and numerical models and experimental measurements.

Calibration ensures that the acoustic properties of the designed metamaterials are then replicated in real-world scenarios, enhancing the stability and robustness of the development and design method. Especially, FDM is a rapid and cost-effective prototyping method, the printing setups of which need to be carefully analyzed as part of an effective and potentially fragile process. The filling density, printing speed, and printing quality of FDM can influence the accuracy of prototypes and, consequently, the acoustic characteristics, especially in acoustic metamaterials whose properties should, in a first approximation, depend exclusively on their geometric parameters.

The optimization of parameters was carried out considering a sample of coiled-up QWR. The geometric parameters of the sample are as follows: a cavity length of $L_t = 133$ mm, the side of the square cavity $2a = 5.59$mm, and the diameter of the circular sample $2R_0 = 39$ mm,as shown in Figure 2.18a. The analytical and numerical results of the resonator are shown in Figure 2.18b: the resonance frequency is $f_R = 638$ Hz, with a modulus of the sound absorption coefficient equal to $\alpha = 0.91$.

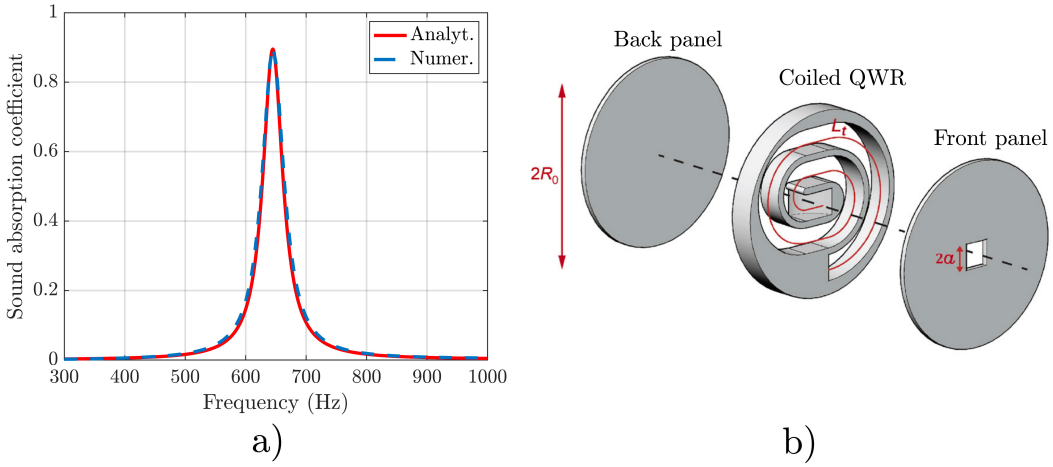


Fig. 2.18 a) Sound absorption coefficient of the coiled-up resonator: analytical and numerical models. The QWR has a resonance absorption peak at $f_R = 638$, with $\alpha = 0.91$. b) 3D sketch of the coiled-up resonator under study for the optimization.

### Influence of filling density

The resulting volume of a 3D printed prototype is defined as the volume within the sample geometry that does not have a specific characterization (e.g., the volume enclosed in a cylinder) and for which a filling density can be set up (with different degrees of customizability). According to Figure 2.19, the resulting volume is highlighted in red, and specific attention should be addressed to this, mainly in developing resonant metamaterials. According to the printing machine's limits, these volumes can be characterized by a specific percentage of filling density. The filling density is strictly connected with the goodness of the acoustical properties of this kind of AMM. Results of Figure 2.20 show that the samples that experimentally present higher correspondence with the analytical model are those having a filling density> 30%, while those with 10% and 20% filling density exhibit the peaks of

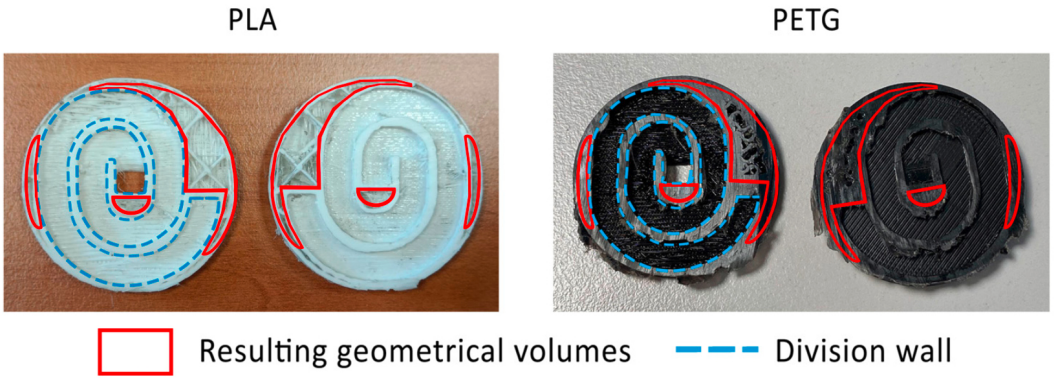


Fig. 2.19 Pictures of the sectioned 3D printed prototypes in FDM-PLA and FDM-PETG, cut in half to display the upper (left) and lower) resulting geometrical volumes (highlighted by the red lines) and the resonant volume wall's (blue lines) characterization can be observed.

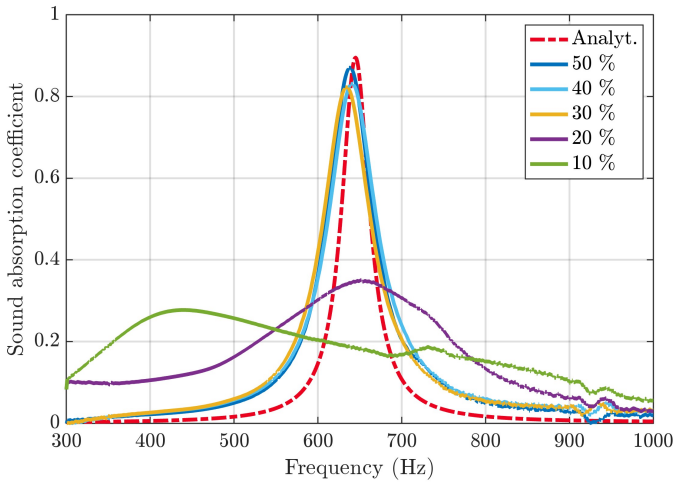


Fig. 2.20 The sound absorption coefficient of a coiled-up Quarter-Wave Resonators (QWRs) sample, 3D printed with various filling densities, was compared with the analytical model.

the sound absorption coefficient too damped and not centered in terms of resonant frequency. This happens because the infill percentage plays an important role in keeping the walls of the resonator rigid. In the case of low infill percentages, the internal walls of the resonator are not to be considered perfectly rigid, but undergo vibration that dampens the absorption of the resonator.

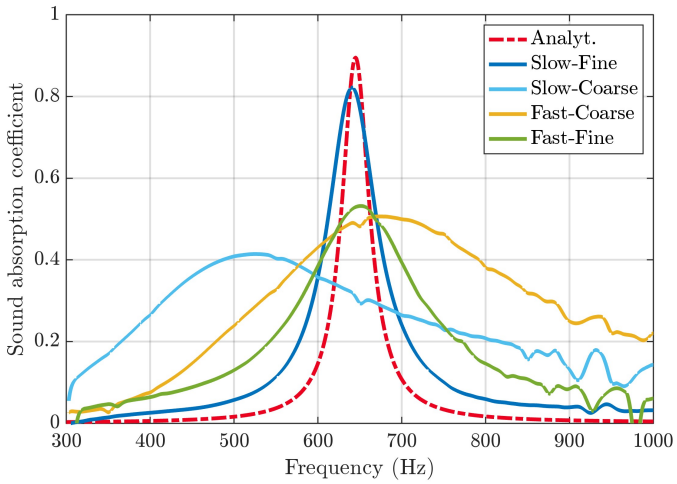


Fig. 2.21 Comparison among the specimens fabricated with the four manufacturing settings and the predictive analytical model; the slow-fine setting best matches the prediction model.

### Printing speed and quality

An investigation into printing parameters was conducted to understand their impact on the acoustic properties of the coiled-up QWR shown in Figure 2.18. Four printing setups were defined based on two different printing speeds and two quality settings. The printing setups include base speed, outline speed, solid layer speed, and infill speed. Quality setups involve layer height and the number of layers for the top and bottom layers. The detailed combinations are described in Table 2.2. Figure 2.21

Table 2.2 Variable FDM printing parameters. The combinations of two printing speed configurations (slow/fast) and two quality setting configurations (fine/coarse) are investigated through four distinct manufactured specimens.

| **Printing speed** | **Slow** | **Fast** |
|---|---|---|
| Base speed $[mm/s]$ | 50 | 80 |
| Outline speed $[mm/s]$ | 15 | 20 |
| Solid layer speed $[mm/s]$ | 30 | 50 |
| Infill speed speed $[mm/s]$ | 45 | 75 |
| **Quality setting** | **Fine** | **Coarse** |
| No. of top and bottom solid layers | 4 | 2 |
| Layer height $[mm]$ | 0.12 | 0.30 |

displays the absorption coefficient results for the four samples, all sharing the same nominal geometry and dimensions, manufactured with the four combinations of

printing parameters: slow-fine, slow-coarse, fast-coarse, and fast-fine. Root-mean-square (RMS) deviations have been calculated to quantify the discrepancies between each configuration and the analytical model: 27% for fast-coarse, 21% for fast-fine, 30% for slow-coarse, and 14% for slow-fine. Observing these experimental results, it is evident that these printing parameters significantly affect the acoustic performance of the specimens and the agreement with the theoretical values. Therefore, the quality setting (fine/coarse) influences more than the printing speed (slow/fast), and to understand why, a qualitative analysis on the inner division wall characterization was run through SEM technology [79].

**Influence of temperature**

The FDM method employs polymeric materials for printing. The performance of polymeric AMM made through FDM may be affected by deformations due to temperature variations [91, 92]. With this premise, an investigation into the influence of temperature variations on PET samples of a coiled-up QWR was conducted. The aim was to explore the relationship between possible environmental conditions and the acoustic properties of this type of metamaterial, not so much on the temperature of the fluid that affects airspeed but whether different temperatures cause deformations to the internal cavities and subsequent differences in the estimated absorption. A climate chamber was employed to alter the temperature of the samples in the range of $T = 10°C - 50°C$, with a $\Delta T = 10°C$. Figure 2.22 shows the experimental results of absorption coefficients measured in the impedance tube under 5 temperature configurations. As detailed in [32], the frequency shift caused by temperature variations due to deformations of the internal cavity, which narrows as the sample temperature increases, was evaluated. Specifically, numerical models were used to identify and quantify the internal deformations of the samples. First, a calibration of the numerical models was performed based on experimental measurements of the sound absorption coefficient of the sample at $T = 20°C$; then, the actual deformations were determined by imposing the five temperature scenarios; finally, the acoustic performance was determined for each deformed mesh, i.e., for each temperature value considered. All the experimental measurements in the impedance tube have been conducted on a circular impedance tube with a diameter of 40 mm. This allowed to investigate absorption properties in the frequency range between 300 and 4000 Hz. The results showed that temperature variation does not significantly impact the absorption coefficient's amplitude and quality factor, as reported in Table 2.3.

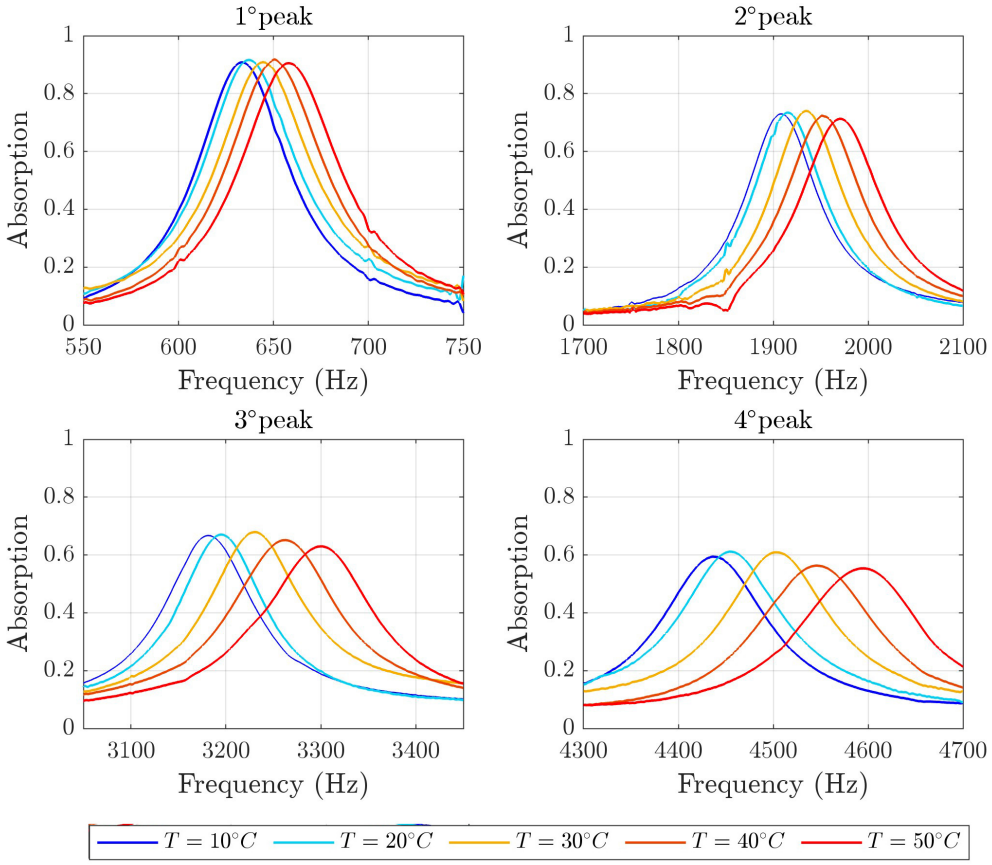


Fig. 2.22 Experimental curves obtained by increasing the temperature with $\Delta T = 10°$. The variation of resonance frequency ($f_{R,n}$) of the first absorption peak and three harmonics is reported; amplitude ($a_{max,n}$), and $1/Q_n$ parameter for the first resonance peaks are reported in Table 2.3

The frequency shift of the first resonant peak can also be evaluated considering as the reference point the resonance peak frequency at $T = 20°$ C. A comparison of the experimental results with the specific volume variations for polyethylene resins through the ratio $f_R/f_{R,20°}$ has been made. Figure 2.23 reports the numerical and experimental regression curves [32]. The resulting trend is similar to relative volume variations of PET resins provided by [93], even if the temperature range allows analysis of only the early part of the exponential functions. The exponential regression curve related to the resonance peaks of the sample is expressed by:

$$\frac{f_R}{f_{R,20°}} = Ae^{BT^2} \tag{2.91}$$

Table 2.3 Experimental variation of the fundamental resonance frequency, amplitude and $1/Q$ parameter for the coiled-up QWR in steps of $\Delta = 10°C$.

| Temperature | $f_R$ (Hz) | $\alpha_{max}$ | $1/Q$ (%) |
|---|---|---|---|
| $T = 10°C$ | 632 | 0.90 | 9.0 |
| $T = 20°C$ | 638 | 0.91 | 9.2 |
| $T = 30°C$ | 645 | 0.90 | 9.8 |
| $T = 40°C$ | 651 | 0.91 | 10.0 |
| $T = 50°C$ | 638 | 0.91 | 10.1 |

where $A = 0.9924$, $B = 16.32x10^{-6}$, and the coefficient of determination that expresses the robustness of the regression are equal to $R^2 = 0.99$. These results must be

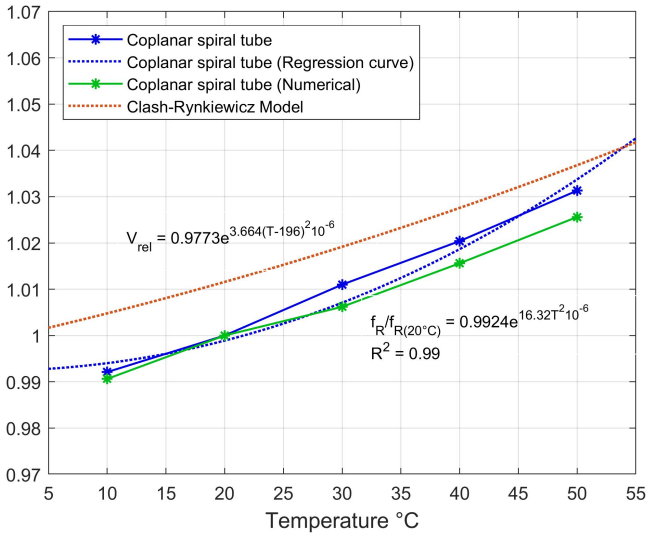


Fig. 2.23 Comparison between the regression curve for $f_R/f_{R,20°}$ experimental values, numerical values, and the specific volume variations for polyethylene resins for a coiled Quarter Wavelength Resonator.

taken into consideration when PET metamaterial prototypes are used for industrial applications that require fine-tuning of the metamaterials and involve a significant alteration of ambient temperature.

## 2.7 Validation

The steps outlined so far to realize metamaterials represent a robust design method but involve some simplifications and ideal conditions. Analytical and numerical models inherently contain approximations by definition and are necessary for understanding the problem from a general perspective. On the other hand, experimental measurements in the impedance tube also serve as a method for acoustical characterization of materials under plane wave assumption and normal incidence. For real-world applications, this thesis leverages additional validation tools. These validation tools may include more complex numerical models or those more representative of real-world scenarios, as well as other experimental measurements more relevant to the specific application. These alternative validation tools have been employed, depending on the requirements and possibilities. In some cases, room acoustics simulations have been implemented to simulate a real-world context and extrapolate parameters of practical interest. In others, such as with speakers, experimental measurements of the object's frequency response serve as a valid validation method, relying on comparing pre- and post-application scenarios of the designated metamaterial designs. In cases where other validation methods different from those already introduced have been used in this work, their theoretical background will be introduced and analyzed in order to better understand and interpret the results obtained, on a case-by-case basis.

# Chapter 3

# Application in a diffuse field: the hospital setting

This chapter focuses on the development and design of acoustic metamaterials to enhance acoustic comfort within hospital environments. Specifically, the aim is to create an alternative to traditional sound-absorbing materials, which are challenging to use in a setting that demands hygiene and maintenance considerations. First, an analysis of the acoustic context to be addressed was conducted through a sound pressure level monitoring campaign and a reverberation time measurement campaign. Additionally, a clustering analysis was carried out to qualitatively understand the acoustic context, identifying the contribution of different noise sources within the considered spaces. Once the target noise was characterized, an acoustic metamaterial based on Helmholtz resonators was developed analytically, numerically, and experimentally using the method described in the previous chapter. Finally, after prototyping a sample and measuring it in the impedance tube to verify the match with the models, a hybrid FDTD/GA numerical model of the treated environment was developed to assess the potential impact of the metamaterial as a ceiling panel, in terms of reverberation time in a simulated scenario.

## 3.1 Case study

The experimental study was conducted in two rooms of a hospital located in Bologna, Italy. Both units feature rectangular layouts with similar geometric dimensions. One room is a four-bed bay in active conditions (referred to as room A), and measures 5.95 meters in length, 6.45 meters in width, and has a height of 3 meters. The

second room is a four-bed bay, in empty and unoccupied condition (referred to as room B), and measures 5.85 meters in length, 6.40 meters in width, and has a height of 4 meters (as shown in Figure 3.1). These rooms have separate bathrooms

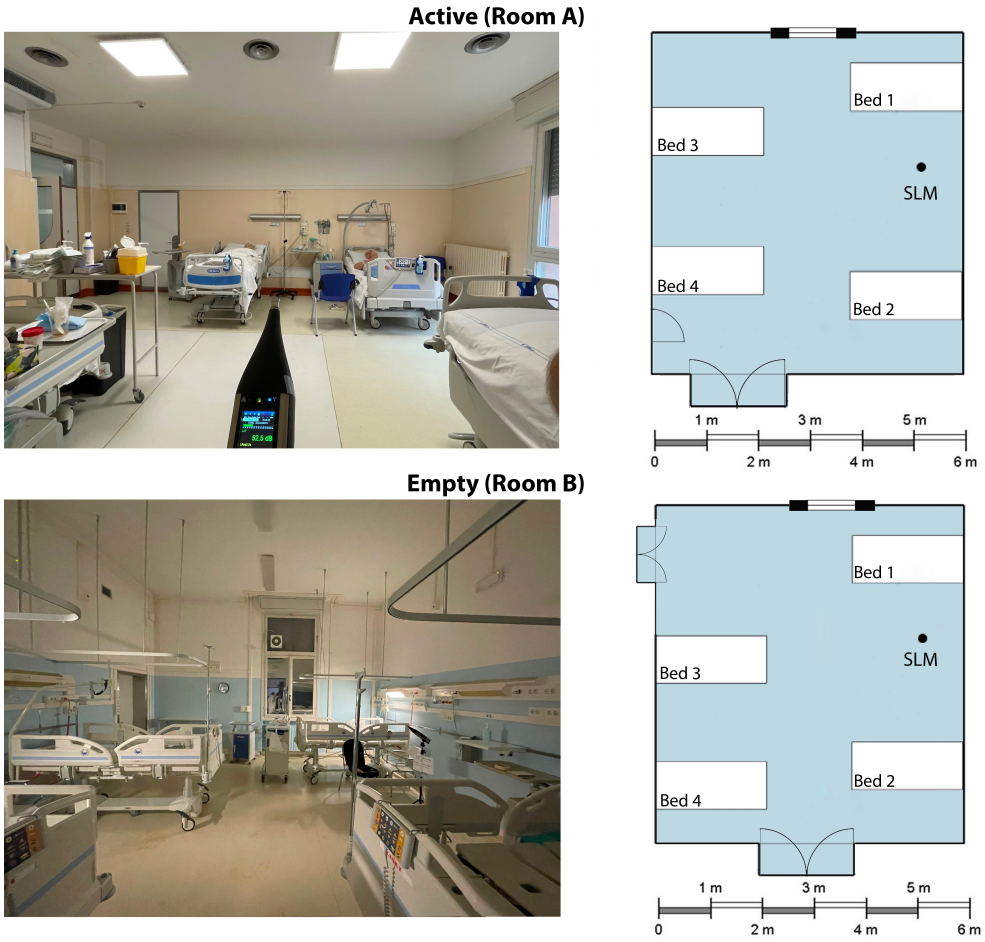


Fig. 3.1 (Top) Picture of the active four-bed bay (room A) and plane. (Bottom) Picture of the empty four-bed bay (room B) and plan. The black dots on the plans refer to the sound lever meter positions for monitoring.

and shower facilities and are situated in the same geriatric ward, albeit on different building floors. Each room has a rectangular window facing the inner courtyard of the building, and the entire facility is situated away from the city center and traffic noise. The building holds historical significance, and the hospital hosted the medical school and university. Consequently, the hospital's routine involves a morning round taking place between 9:00 a.m. and 11:00 a.m., during which doctors and students visit all patients' rooms. Additionally, various healthcare services,

including medication, administration, and infusions by nurses, occur throughout the day and night, typically three to four times daily. It's worth noting that the rooms lack acoustic treatment, and the doors are typically kept open while the windows remain closed.

## 3.2 Noise characterization

The first step was to characterize the noise within the environments. A sound monitoring was conducted in the two rooms to understand the total sound pressure levels and contributions in one-third octave bands. Additionally, a measurement campaign of room acoustic parameters was carried out in the empty room (room B), where there would be no interference with patient care and normal activities, to quantify the reverberation time. Finally, a qualitative analysis of the sound pressure levels collected from monitoring the occupied room was conducted through clustering analysis. It was possible to identify the origin of sound sources within the environment through clustering algorithms, separating the noise sources into clusters, one connected to human activity and the other to mechanical sources. Machine learning algorithms were applied to a dataset derived from the most annoying time period for patients and staff: morning rounds.

### 3.2.1 Sound Level Monitoring

The experimental study in the active room was conducted in July 2022 in Bologna, Italy, while the empty room was monitored in September 2022. In both instances, Sound Pressure Levels (SPLs) were recorded continuously over two days (48 hours) from Thursday to Saturday. The monitoring was carried out using a calibrated 01dB DUO sound level meter, with measurements taken at 100 millisecond intervals. The active room (room A) is situated within the geriatric care section of the hospital. In this setting, various mechanical systems, including the Heating, Ventilation, and Air Conditioning (HVAC) system, air exchanger, and alarm devices, were active. Life-saving equipment was consistently used to monitor patients' physiological parameters, and the presence of people in the active room contributed to the overall noise level. The empty room (room B) is in a temporarily closed area of the same geriatric care section. However, the HVAC and alarm devices were still active. These rooms were selected due to their comparable volumes, building design, distance

from the city center, and road traffic. Two sound level meters were positioned between two beds near the wall to ensure they did not obstruct the movement paths of patients and hospital staff. The microphone was placed approximately 1 meter from the wall between bed 1 and bed 2, positioned as close to the height of the patient's head as possible (Figure 3.1). Room A was selected based on input from nursing and medical staff, considering factors such as availability, the presence of four patients, and proximity to the ward corridor and the nurses' control room. Room B was chosen for its similar geometric characteristics and the availability of a fully unoccupied floor, minimizing external noise sources except for the ventilation system. Measurements were taken for A-weighted and Z-weighted short-time equivalent levels with a one-third-octave band filtering. Throughout the monitoring process, all staff members were instructed to continue their regular activities while avoiding any contact with or moving the equipment. No patient admissions or initial check-ups have been documented during the monitoring. Figure 3.2 reports the corresponding time-frequency spectrograms revealing the SPLs of each third-octave across the frequency range 25 - 20000 Hz. The spectrogram of the active room shows a wide variety of different noises. Three distinct morning rounds are recognizable between 9:00 a.m. and 11:00 a.m. on each monitoring day. Moreover, medications and general care services occur randomly during the mornings and evenings and generally stop after 8:00 p.m. [94]. In the empty room, the SPLs remained constant for all the monitoring, except between 10:00 a.m. and 11:00 a.m. of the second day, when the ventilation systems went off. In addition to the difference due to human activity in the two spectrograms, there is another significant distinction. The spectrogram of the active room exhibits a third continuous component in the one-third octave band of 160 Hz. This may be attributed to a second ventilation system dedicated to air exchange, which is inactive in the empty room.

### 3.2.2 Comparison with WHO guidelines

The guidelines from the World Health Organization (WHO) regarding community noise [95] propose specific limits for ambient noise in rooms where patients are treated or observed. These limits are designed to alleviate potential adverse effects on the health of both patients and staff. To be more specific, WHO sets a limit for the A-weighted equivalent sound pressure level (SPL) at $L_{A,eq} = 35$ dBA during both daytime and nighttime, with a maximum value of $L_{A,max} = 40$ dBA. Numerous studies have highlighted the challenge of adhering to WHO guidelines, which generally

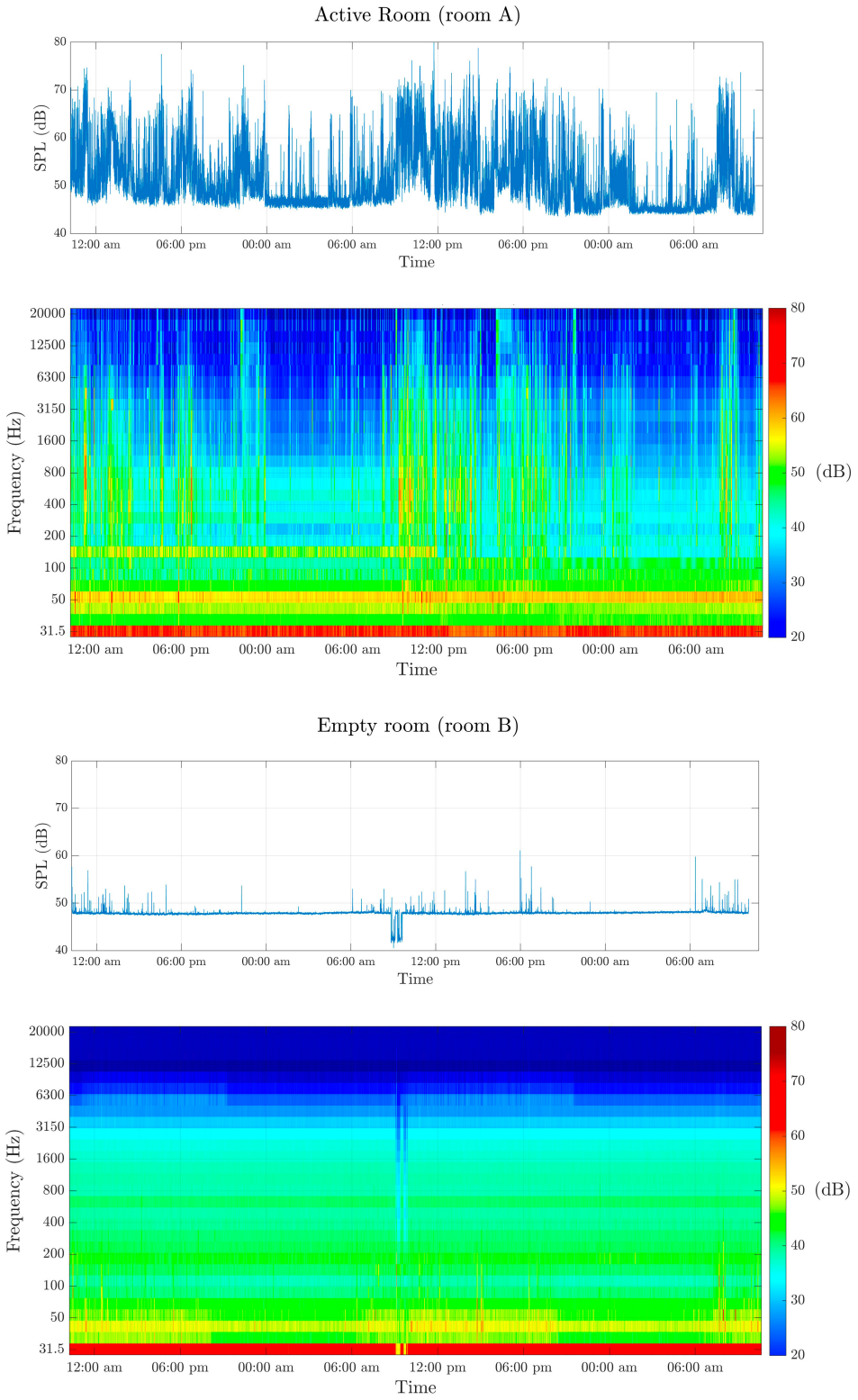


Fig. 3.2 Time history and spectrogram of the Z-weighted short-time equivalent levels $L_{Z,eq}$ collected during the two-day monitoring in the room A (Top) and in the room B (Bottom).

impose very stringent SPL limits [96–98]. However, there is currently no standardized measurement protocol for assessing the acoustic environment within hospitals. The histogram of figure 3.3 shows the equivalent A-weighted SPLs collected within the active room (Room A) and the empty room (Room B) during the monitoring, compared to the WHO guidelines limits for daytime and nighttime. The active room

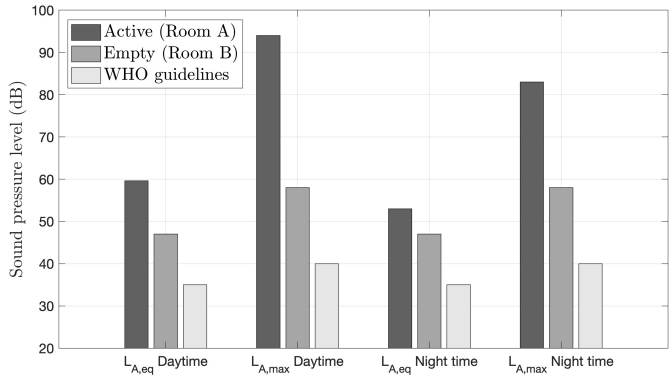


Fig. 3.3 Spectrogram of the Z-weighted short-time equivalent levels $L_{Z,eq}$ collected during the two-day monitoring in room A (Top) and in room B (Bottom).

exceeds the limits set by the WHO during the day by at least 25 dBA of equivalent level and at night by 15 dBA of equivalent level. Even the $L_{A,max}$ are well above the recommended thresholds in the active room. The interesting point is that even room B exceeds the equivalent and maximum levels suggested by the WHO. This means that the ventilation systems installed in hospital rooms are the cause of exceeding the indicated thresholds.

### 3.2.3 Room Acoustics parameters

A measurement campaign of reverberation time was conducted in the empty room (Room B). The measurements were made possible because the room was in a temporarily closed-off section of the ward, away from patients and staff. This allowed the measurements to be carried out without interruption and without causing any disruptions to the regular activities. An exponential sine sweep (ESS) has been generated through custom software. The length of the input signal was 10 seconds. For the measurements, two source points and six receiver points (see Figure 3.4) were selected to obtain the reverberation time in octave bands, ranging from 125 Hz to 4000 Hz, in accordance with ISO 3382:1-2008 standards [99]. The Impulse Responses (IR) has been acquired through the deconvolution process.

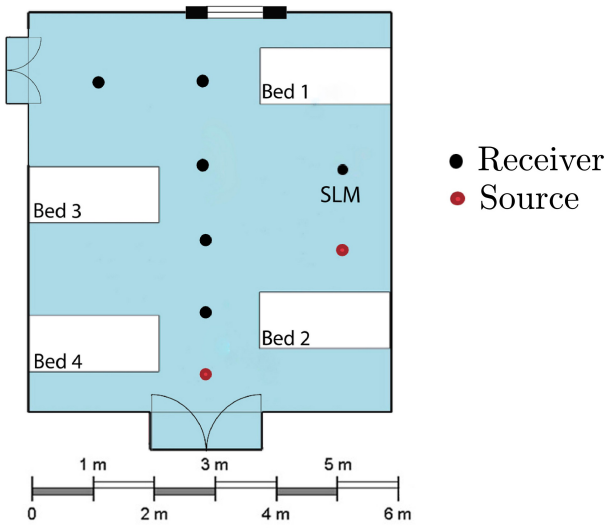


Fig. 3.4 Plan of the empty room: 2 source and 6 receiver points have been chosen for the reverberation time measurements.

Table 3.1 shows the results of the experimental campaign in terms of reverberation time ($T_{20}$) inside the empty room. The octave bands with the highest reverberation times are 125 and 500 Hz. The latter, in particular, significantly impacts speech intelligibility within the space. Regarding the elevated reverberation times in the bands at 2000 and 4000 Hz, it should be noted that the room was unoccupied and equipped with minimal medical equipment. Additionally, mattresses were not present on the 4 beds, which, in occupied conditions, would considerably reduce $T_{20}$ in these bands, along with the presence of individuals. An interesting point is the reduction in the reverberation time in the octave band of 250 Hz. The plausible explanation is the presence of two wall cabinets positioned on the wall near the room's entrance door: they consist of two sliding wooden panels that close the air cavities, acting as absorbers in this octave band, significantly reducing the reverberation time.

Table 3.1 Trend in frequency of $T_{20}$ mean values corresponding to the results of the measurements made according to ISO 3382:2-2008.

| | **125 Hz** | **250 Hz** | **500 Hz** | **1000 Hz** | **2000 Hz** | **4000 Hz** |
|---|---|---|---|---|---|---|
| $T_{20}$ | 1.81 | 1.35 | 1.74 | 1.55 | 1.68 | 1.44 |

Fig. 3.5 Photographs of the reverberation time measurements in the empty room: an omnidirectional source (dodecahedron) has been used as a source in two locations.

### 3.2.4 Clustering analysis

In addition to the typical approach commonly employed, a statistical analysis has been performed on the recorded Sound Pressure Levels (SPLs) in room A, which is the active room. The method utilized for this statistical analysis draws from prior applications in educational and office environments [100–102] . Earlier studies explored various algorithms to distinguish noise contributions in real-world settings and concluded that the Gaussian Mixture Model (GMM) was the most suitable approach for using SPL occurrences [103]. Consequently, all the collected short-time equivalent levels served as the data population to be processed using GMM.

#### Gaussian Mixture Model

GMM is a clustering method that characterizes the original data as a linear combination of Gaussian curves [104, 105]. Given a set of observations $x_1, \ldots, x_n$ (e.g., the collected short-time equivalent levels), the Gaussian probability density function

$f(x_i)$ for these observations can be represented as a sum of $K$ Gaussian densities $f_k(x_i, \mu_k, \sigma_k^2)$:

$$f(x_i) \simeq \sum_{k=1}^{K} \pi_k f_k(x_i, \mu_k, \sigma_k^2) \tag{3.1}$$

where $\pi_k$ are the so called *mixing proportions* [105], non-negative quantities that sum to one; that is, $0 \leq \pi_k \leq 1 \quad (k = 1, \ldots, K)$ and $\sum_{k=1}^{K} \pi_k = 1$. The likelihood function for a mixture model with $K$ univariate Normal components is detailed:

$$\mathscr{L}(x) = \prod_{i=1}^{n} \sum_{k=1}^{K} \pi_k f_k(x_i) = \prod_{i=1}^{n} \sum_{k=1}^{K} \pi_k \frac{1}{\sqrt{2\pi\sigma_k^2}} e^{-\frac{(x_i-\mu_k)^2}{2\sigma_k^2}}. \tag{3.2}$$

The equality in this equation is generally achieved using the Expectation-Maximization (EM) optimization algorithm [104]. A pivotal step in unsupervised analysis with GMM is determining the number of clusters to search for. This number, denoted as $K$, must be established before beginning the iterative process and is determined using various evaluation metrics, including the Calinski-Harabasz index, Davies-Bouldin index, Silhouette coefficient, and Gap statistic. SPLs octave-band filtered from 31.5 up to 16000 Hz and third-octave band filtered from 25 up to 20000 Hz were used, depending on the noise source under investigation. Octave bands are employed to evaluate human activity, particularly speech, whereas third-octave bands are used for assessing mechanical systems. As detailed described in [94], analysis can be broken down into five steps as follows:

**Step 0 –** After data collection, SPLs are filtered into octave-band or third-octave bands, generating sets of vectors labeled $j = (1, \ldots, N)$ to be linearly independent.

**Step 1 –** SPL occurrences for each band are computed and processed through GMM with varying numbers of clusters $K$. The candidate models, referred to as $GMM(K)$ with $K = (1, \ldots, N)$, represent the so-called candidate models. Candidate models are assessed from $K = 2$ to $K = 6$.

**Step 2 –** The candidate models are evaluated using model selection metrics, including the Calinski-Harabasz index (CH), Davies-Bouldin index (DB), Silhouette coefficient (SC), and Gap statistic (GS). The best model is selected using a majority rule based on the most frequent number of clusters obtained by comparing each evaluation metric.

**Step 3 –** Based on the selected model, statistical features are utilized to categorize different sound sources for each $j$-th vector, with $j = (1,\ldots,N)$ representing the number of bands. Each cluster is associated with a sound source, where the means of the Gaussian curves represent the SPLs, and the standard deviations (s.d.) indicate the extent to which the source is stable or random over time.

**Step 4 –** The columns of the $K$ clusters are consolidated, and each category of noise sources are reconstructed.

In other words, the GMM algorithm takes as input the occurrences of sound pressure level (SPL) values and creates $K$ different clusters based on their standard deviation. Figure 3.6 depicts the case with the number of clusters set to $K = 2$, which is of interest to the present study. From the occurrences curve, two distinct sets of values can be distinguished. Each of these sets represents the occurrences of each of the two clusters.

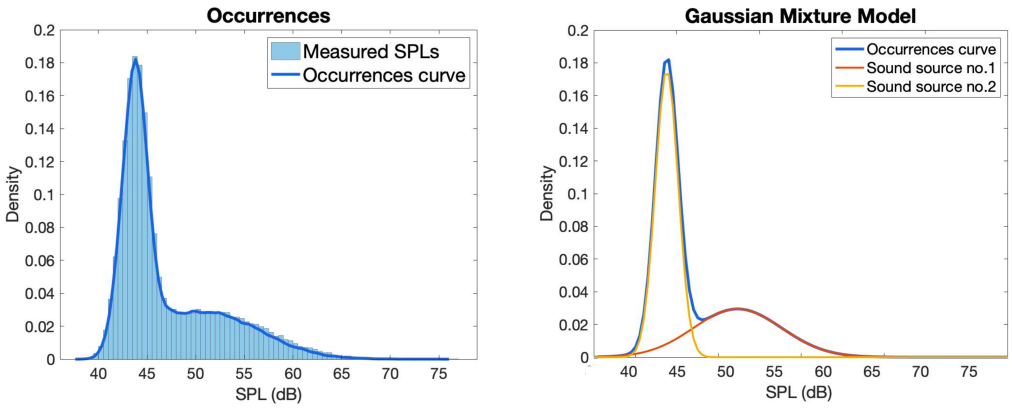


Fig. 3.6 Example of the input occurrences curve and the selected clusters obtained via GMM

As described later, the unsupervised statistical analysis was conducted during the morning rounds of the medical staff. Hence, it is reasonable to consider noise primarily associated with speech and with mechanical noise sources. Based on previous applications [94] and preliminary results in office and classroom settings [101, 100, 103] a preliminary threshold of 5 dB has been set, [106–108]. This is a suitable threshold for distinguishing between continuous sound sources and noises related to human activity [107, 108]. In summary, if a cluster exhibits a standard deviation equal to or greater than 5 dB, it is considered to be a source of speech;

on the other hand, a source with standard deviations lower than 5 dB is regarded as mechanical. Following the five-step procedure for each frequency band, it is possible to attribute features to the same source and reconstruct its spectrum:

$$\sigma < 5\ dB \quad \Longrightarrow \quad Mechanical\ source$$
$$\sigma \geq 5\ dB \quad \Longrightarrow \quad Human\ source$$

The block diagram of the GMM algorithm used in this study is depicted in Figure 3.7. The statistical analysis and post-processing of the collected data were carried out using MATLAB.

### 3.2.5 Morning round analysis

The morning round period proves to be the time of greatest patient discomfort and a crucial time for verbal communication among the staff and between the staff and patients [109]. The morning round considered for this part of the study is the one conducted between 9 a.m. and 11 a.m. on the second day of monitoring. The clustering algorithm allowed for the separation of human noise contributions - associated with all human activities - and mechanical noise contributions - encompassing all contributions from life-saving devices, ventilation systems, and alarms. The separation of the noise sources provides a qualitative assessment of the acoustic context, even in occupied conditions, during the most disturbing time period. Figure 3.8 shows the clustering results obtained by applying the GMM to the SPLs of the two hours of monitoring under consideration. To validate the clustering analysis, the outcomes of human activities were compared with the anechoic speech spectrum, as shown in ISO 3382-3 [110]. In this work, the directional speech spectrum was chosen as the reference. The figure displays the relative spectrum of major speech and the reference, normalized to the 1 kHz octave band at 0 dB. On the other hand, the outcomes of mechanical cluster has been compared with the measured SPLs of the empty room, where only the mechanical sources were present. The curve trends align between 250 Hz and 2000 Hz, where the substantial portion of speech energy is concentrated. The 250 Hz band marks the fundamental frequency of the voice, while the higher-frequency bands capture the articulation of phonemes in various consonants. Some discrepancies arise at 125 Hz and 4000 Hz: the former is likely due to the contribution of the air exchanger at 160 Hz, emphasizing the uncertainties associated with low-frequency speech-in-noise spectra [111]. The latter difference at

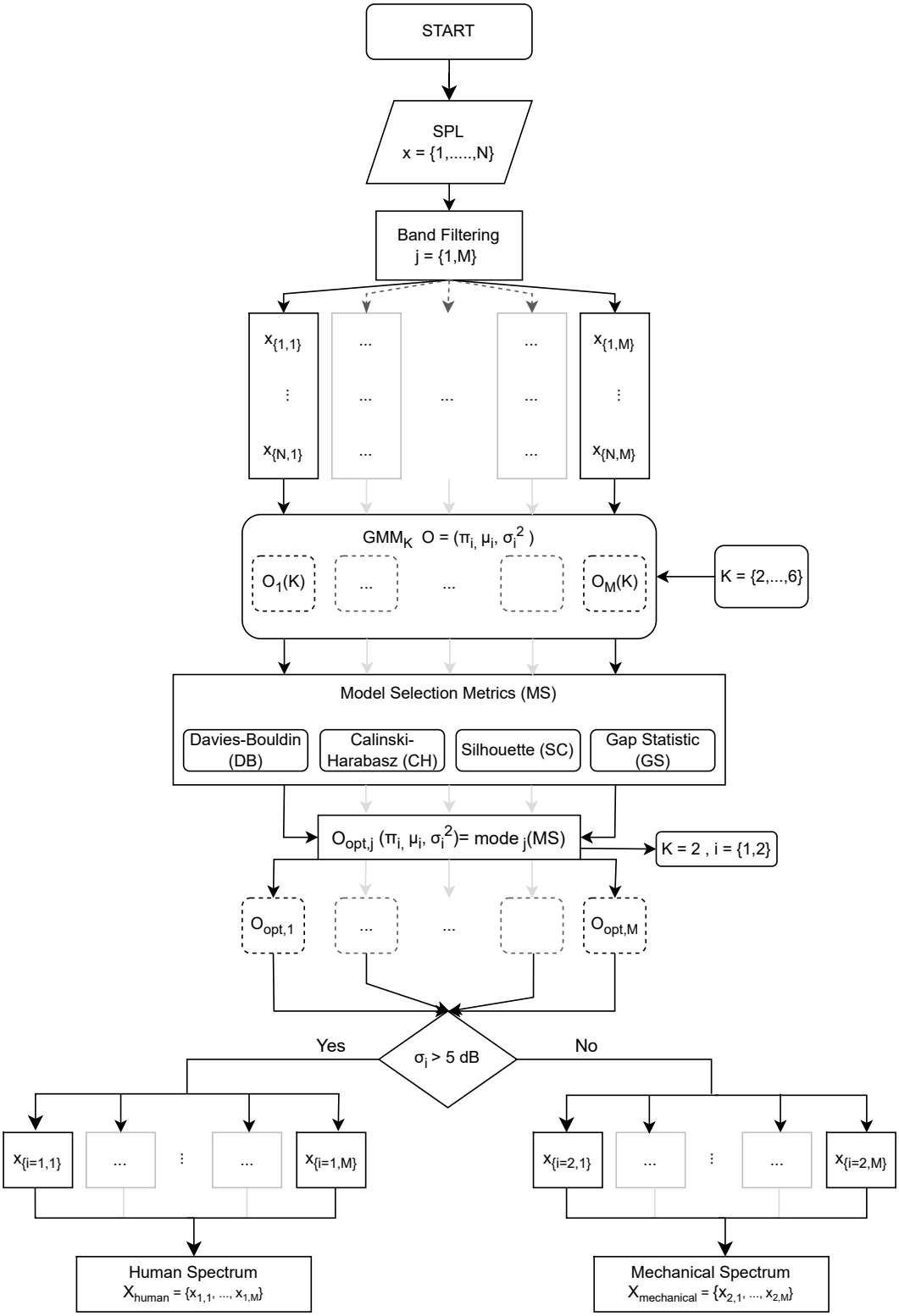


Fig. 3.7 Block scheme of the Gaussian Mixture Model algorithm for the separation of the human and mechanical contribution (Example of the optimal model with $K = 2$).

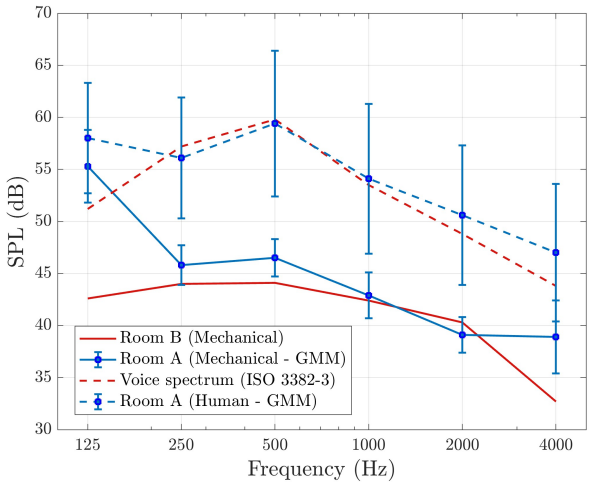


Fig. 3.8 Reconstructed one-octave band spectra of mechanical (solid lines) and human (dashed lines) noises. Blue lines report the results of the separation obtained via GMM in room A. The red solid line reports the spectra of room B (the empty room), where only the ventilations systems are switched on. Furthermore, the speech spectrum - directional source - at a distance of 1 m in free-field according to ISO 3382-3 is reported for a comparison with the humans noise of room A. Error bars show the standard deviations of each Gaussian curve.

4k Hz results from the combined influences of pronounced reverberation, even at higher frequencies.

The comparison of clustering results with the references and the measurement of the unoccupied room provided the opportunity to demonstrate the effectiveness of the algorithm for separating sources even in a complex acoustic environment such as the hospital setting ([94]). Regarding the characterization of noise, the focus of this study, the clustering results of the noise sources confirm that the major contribution to the Sound Pressure Level (SPL) comes from human activity. This has allowed for identifying the octave bands at 500 and 1000 Hz as the frequency range to address the improvement of the acoustic environment within the room by reducing the reverberation time and SPL and enhancing speech intelligibility and communication.

## 3.3 Design of the acoustic metamaterial

Once the environmental noise characterization within the hospital room was completed, the frequency range for improving acoustic comfort became clearer. The idea was to develop a metamaterial to absorb the frequency range between 500 and 1000 Hz, thereby reducing stress in frequencies where the human ear is most sensitive and increasing speech intelligibility, consequently improving communication between staff and patients. Considering the method described in Chapter 2, the idea was to develop a 12 x 12 cm metamaterial unit cell, a replicable unit. The dimensions of the unit cell reflect the possibility of characterizing it in the impedance tube. The acoustic properties valid for the unit cell are maintained in a diffuse field by replicating the unit cell to obtain larger surfaces. Unlike other applications, the metamaterial must ensure broadband absorption. Therefore, the idea is to leverage the available area to implement twenty square-based Helmholtz resonators in parallel, each designed with a different resonance frequency. The analytical model based on the Transfer

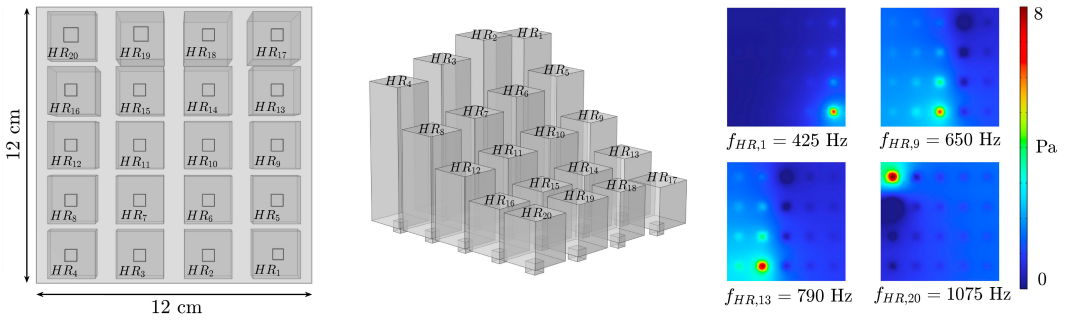


Fig. 3.9 (Left)3D sketch of the unit cell, made by 20 different Helmholtz resonators; (Center) Fluid path cavities of the Helmholtz resonators of the unit cell; (Right) The pressure distribution visualized at the opening plane of the resonator at specific frequencies: $f_{HR,1} = 425$ Hz, $f_{HR,9} = 650$ Hz, $f_{HR,13} = 790$ Hz, and $f_{HR,20} = 1075$ Hz.

Matrix Method (TMM) was used for the initial design of the geometric parameters of the resonators, namely the side ($a_n$) and length ($l_n$) of the neck, and the side($l_c$) and length($l_c$) of the cavity. The constitutive parameters were optimized through a numerical model in Comsol, as shown in Figure 3.9.. Table 3.2 provides all the values of the constitutive parameters of the 20 Helmholtz resonators used, along with their absorption frequency.

Table 3.2 Constitutive geometrical dimensions of the 20 Helmholtz resonators used to design the unit cell for broadband absorption in the frequency range 500-1000 Hz.

| | $a_n$ [cm] | $l_n$[cm] | $a_c$[cm] | $l_c$[cm] | $f_R$ [Hz] |
|---|---|---|---|---|---|
| Resonator 1 | 0.45 | 0.55 | 2.00 | 8.20 | 425 |
| Resonator 2 | 0.50 | 0.55 | 2.00 | 8.50 | 460 |
| Resonator 3 | 0.50 | 0.55 | 2.00 | 7.70 | 490 |
| Resonator 4 | 0.50 | 0.55 | 2.00 | 7.00 | 510 |
| Resonator 5 | 0.50 | 0.55 | 2.00 | 6.60 | 530 |
| Resonator 6 | 0.50 | 0.55 | 2.00 | 5.50 | 560 |
| Resonator 7 | 0.50 | 0.55 | 2.00 | 5.40 | 595 |
| Resonator 8 | 0.50 | 0.55 | 2.00 | 5.00 | 620 |
| Resonator 9 | 0.50 | 0.55 | 2.00 | 4.60 | 650 |
| Resonator 10 | 0.50 | 0.55 | 2.00 | 4.30 | 675 |
| Resonator 11 | 0.50 | 0.55 | 2.00 | 3.85 | 715 |
| Resonator 12 | 0.50 | 0.55 | 2.00 | 3.50 | 755 |
| Resonator 13 | 0.50 | 0.55 | 2.00 | 3.20 | 790 |
| Resonator 14 | 0.50 | 0.55 | 2.00 | 2.90 | 835 |
| Resonator 15 | 0.50 | 0.55 | 2.00 | 2.65 | 880 |
| Resonator 16 | 0.50 | 0.55 | 2.00 | 2.40 | 910 |
| Resonator 17 | 0.50 | 0.55 | 2.00 | 2.20 | 950 |
| Resonator 18 | 0.50 | 0.55 | 1.80 | 2.50 | 995 |
| Resonator 19 | 0.60 | 0.55 | 2.00 | 2.50 | 1030 |
| Resonator 20 | 0.60 | 0.55 | 2.00 | 2.30 | 1075 |

### 3.3.1 Prototyping

The goal was to manufacture a 12 cm x 12 cm sample for measurement in the square impedance tube. The unit cell can then be replicated to cover the necessary surface, maintaining the acoustical properties of the unit cell, with the adequate corrections. The method chosen for 3D printing the sample is Stereolithography (SLA). The decision to design square base cavities from the increased ease of printing the resonator cavities without the risk of internal walls deforming due to the material deposition weight during printing. Furthermore, the decision to develop all Helmholtz resonators with an equal neck length ($l_n$) is dictated by the need to simplify the printing process. It was, therefore, decided to change the other geometric parameters while keeping the neck lengths all equal. The best printing setup in terms of printing speed and printing quality, as described in Chapter 2. It took 8 hours to complete the printing process and obtain the sample shown in Figure 3.10. The thickness of the sample is 10 cm.

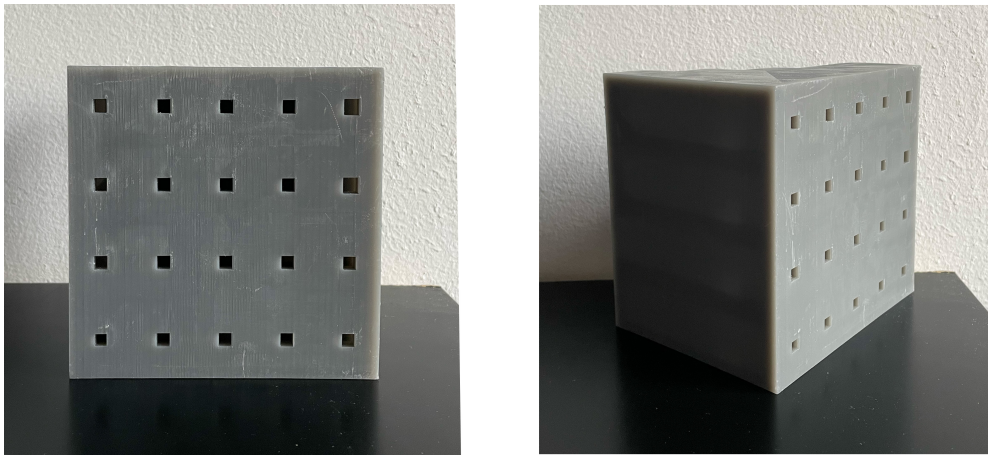

Fig. 3.10 Photographs of the 3D printed unit cell for broadband absorption.

### 3.3.2 Impedance tube measurements

The metamaterial prototype was measured in the square-based impedance tube. The measurement was conducted using the two-microphone technique for absorption, as described in the methodology of this thesis. The sample was mounted inside the tube, and efforts were made to minimize mounting-induced leakages (Figure 3.11). The results of the experimental measurements are presented in Figure 3.12. A

Fig. 3.11 Pictures of the sample mounted inside the square-based impedance tube.

comparison with analytical and numerical predictive models showed good agreement. The sample provides absorption $\alpha > 0.6$ over a frequency range from 420 to 1080 Hz. A phenomenon of evanescent coupling between the resonators in the experimental measurements can be observed, which is not present in the models. Analytical models do not account properly for the coupling effect of different resonators placed in relative proximity. This effect is mostly evident in the extreme frequency range

of absorption: there is a decrease in the sound absorption peak of resonator 1 and resonator 20.

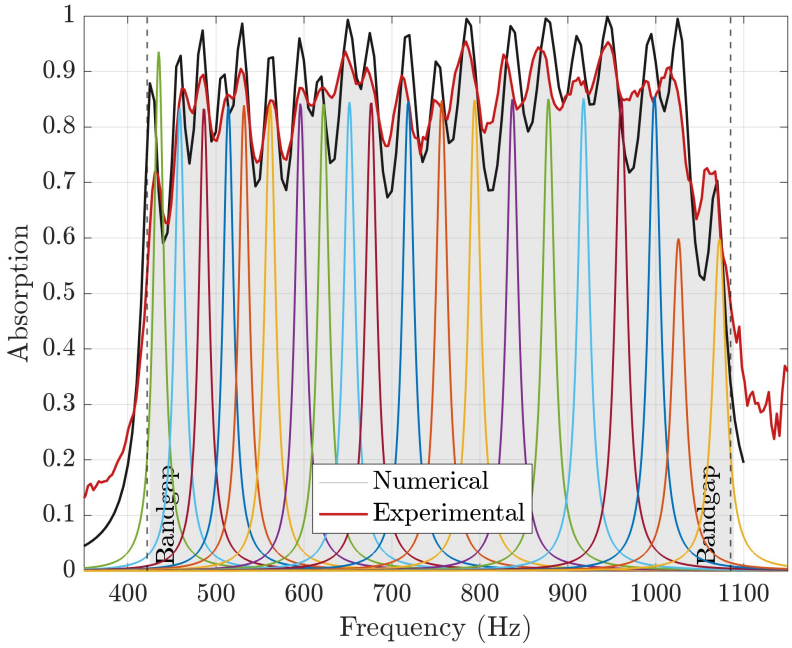


Fig. 3.12 Sound absorption coefficient of the unit cell measured in the impedance tube and compared to the analytical and numerical models.

## 3.4 Numerical validation

The practical implementation of the metamaterials false ceiling was not considered for the present study due to high costs, time constraints, and the difficulty of installation in a hospital room, part of an active hospital ward. The validation method for this application involved developing a numerical model to quantify the effect of the metamaterial in a simulated scenario. A hybrid finite-difference time-domain (FDTD) and geometrical acoustic (GA) numerical model has been developed on the software Treble, to simulate the empty room (Room B) before and after applying a metamaterial ceiling in terms of reverberation time ($T_{20}$).

### 3.4.1 Calibration

The initial step involved the calibration of the numerical model with the experimental reverberation time measurements of the environment. The hybrid 3D model of the considered environment was implemented in Treble, room simulation software [112]. The Treble algorithm directly solves the wave equation for low frequencies. This approach offers numerous advantages, including avoiding additional physical approximations in sound propagation, such as interference, scattering, diffraction, and modal behavior [113–115]. On the other hand, it uses a classical geometrical acoustics algorithm (GA) to compute the acoustic response at high frequencies, thus preventing computational overload on the model. The cutoff frequency for the use of the two algorithms was chosen to be $f = 500$ Hz, which proves to be a good compromise for the dimensions of the considered room. The overall calculation range was set from the octave of 63 Hz up to that of 8 kHz. The length of the impulse response output by the software was set to 3 s, knowing from measurements that the reverberation times in various bands did not exceed 2 s. The calibration was performed considering the two sound source positions during the measurements, as indicated in Fig. 3.4. The tolerance range for reverberation

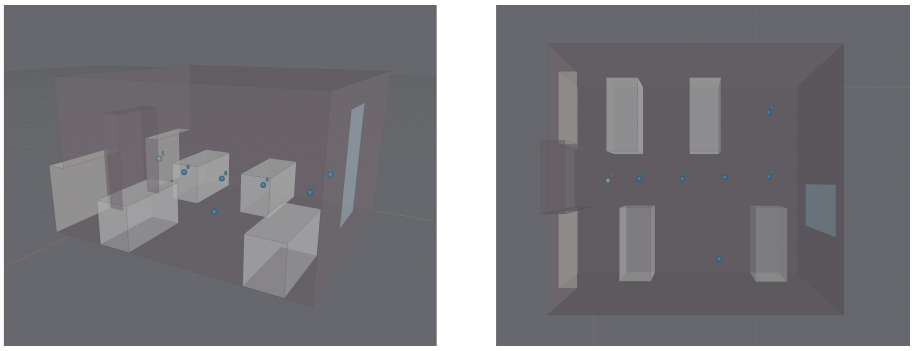

Fig. 3.13 3D model of the hospital room: source and receiver points are highlighted in the figure.

time in the hospital room was set to 10% for each octave band. The boundary conditions assigned to the materials are derived from the software's material list and are reported in Table 3.3 based on scientific literature. The wave-based algorithm part uses the absorption coefficients and converts them into frequency-dependent complex acoustical impedances, while the geometrical acoustics algorithm part directly employs the input absorption coefficient values. High scattering values ($s = 0.5$) were assigned to the beds to compensate for the modeling reduction, according

to literature [116, 117], while the standard ($s = 0.05$) was assigned to the remaining surfaces. The built-in closet near the entrance door was modeled as a wooden wall followed by an air cavity, resulting in absorption at low frequencies, around 250 Hz. For the metamaterial surface based on Helmholtz resonators, measured

Table 3.3 Sound absorption coefficients per octave, and scattering coefficient s assigned to the 3D model's surfaces (Treble).

| **Materials** | 125 Hz | 250 Hz | 500 Hz | 1000 Hz | 2000 Hz | 4000 Hz | 8000 Hz | s |
|---|---|---|---|---|---|---|---|---|
| Floor | 0.01 | 0.01 | 0.01 | 0.01 | 0.01 | 0.01 | 0.01 | 0.05 |
| Windows | 0.14 | 0.22 | 0.03 | 0.02 | 0.02 | 0.01 | 0.01 | 0.1 |
| Beds | 0.31 | 0.31 | 0.25 | 0.13 | 0.09 | 0.09 | 0.07 | 0.5 |
| Closet | 0.02 | 0.33 | 0.02 | 0.02 | 0.02 | 0.01 | 0.01 | 0.05 |
| Wall | 0.04 | 0.04 | 0.03 | 0.004 | 0.005 | 0.005 | 0.005 | 0.005 |
| **Metamaterial** | 0.11 | 0.24 | 0.79 | 0.77 | 0.37 | 0.1 | 0.01 | 0.2 |

absorption coefficient values in the impedance tube were considered. A reverse engineering process is performed by the software, which converts energy-based acoustic absorption values to pressure-based values of surface impedance of the material [118]. This process reconstructs phase information from actual absorption coefficient values, minimizing the objective function $\chi$, defined as follows:

$$\chi = |\hat{\alpha} - \alpha_{input}|^2 \tag{3.3}$$

where $\hat{\alpha}$ is the computed random incidence absorption coefficient from the estemated model of surface impedance, $\alpha_{input}$ is the absorption coefficient from the material datasheet. For a specific incident angle $\theta$, $\hat{\alpha}$ is defined as:

$$\hat{\alpha} = 2\int_0^{\frac{\pi}{2}} \frac{\sin(2\theta)4Re(\hat{Z})\cos(\theta)}{|\hat{Z}|^2\cos^2(\theta) + 2Re(\hat{Z})\cos(\theta) + 1} d\theta \tag{3.4}$$

The software then seeks $\hat{Z}$ values that minimize the objective function $\chi$. This results in a non-unique problem; hence, the values are constrained to more restrictive ranges based on the nature of the material being more or less absorbent and the mechanism characterizing its absorption property. In the case of the false ceiling, a resonant absorbing material was selected. Once the type of absorbing material is chosen, the software recalibrates the alpha values and assigns plausible values for the complex impedance. Despite these limitations, the software proved useful in obtaining a meaningful estimate of the metamaterial's effectiveness while maintaining simplicity in validation.

### 3.4.2 Results

Simulation results show that introducing the metamaterial at the hospital room's ceiling enhances the acoustic behavior in the frequency range of 500-1000 Hz, improving the condition for speech communication. The improvements are evaluated in terms of $T_{20}$ values averaging all the source-receiver pairs considered (see locations of sources and receivers in Fig.3.4). Results show a significant decrease of reverberation time values at the mid frequencies assessed, as shown in Table 3.4. Simulation

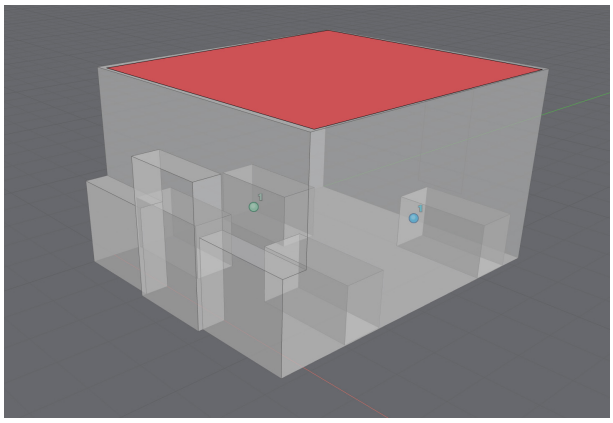

Fig. 3.14 3D view of the acoustic treatment virtually introduced into the numerical model. The metamaterial ceiling is highlighted in red.

results show that introducing the metamaterial at the hospital room's ceiling enhances the acoustic behavior in the frequency range of 500-1000 Hz, improving the condition for speech communication. The improvements are evaluated in terms of $T_{20}$ values averaging all the source-receiver pairs considered (see locations of sources and receivers in Fig.3.4). Results show a significant decrease of reverberation time values at the mid frequencies assessed, as shown in Table 3.4.

Table 3.4 Trend in frequency of $T_{20}$ mean values corresponding to the results of the measurements ("Meas.), the equivalent values obtained from the calibration of the numerical model ("before treatment") and the variations due to the applications as the metamaterial false ceiling ("After treatment").

| $T_{20}$ **(s)** | 125 Hz | 250 Hz | 500 Hz | 1000 Hz | 2000 Hz | 4000 Hz |
|---|---|---|---|---|---|---|
| Measurement | 1.81 | 1.35 | 1.74 | 1.55 | 1.68 | 1.44 |
| Num.(before) | 1.80 | 1.48 | 1.65 | 1.58 | 1.45 | 1.23 |
| Num.(after) | 1.42 | 1.00 | 1.08 | 1.44 | 1.19 | 1.12 |

### 3.4.3 Discussions

From the results of the noise characterization, it is evident that the considered hospital environment does not meet the requirements for the acoustic comfort of both patients and staff in its current state. The sound pressure levels are high and exceed the limits suggested by the WHO. Moreover, the ventilation systems alone already do not comply with the guidelines. The reverberation time is excessively high, leading to elevated SPLs, also due to the absence of acoustic treatment. Hospital environments pose challenges for acoustic treatments, especially when employing conventional porous and fibrous sound-absorbing materials. The latter are prone to deterioration and require continuous maintenance in a non-critical healthcare setting. In a hospital context, they may also become risky materials due to stringent hygiene and safety regulations for patients. The results of the simulation of the implementation of the acoustic metamaterial within the hospital room led to a decrease in reverberation time. Despite this, a greater reduction may be expected to fulfill room acoustics recommendations in hospitals and healthcare facilities, improving the acoustic conditions for both staff and patients. In any case, acoustic metamaterials have demonstrated that they can offer an alternative solution, addressing both acoustic and material considerations, as their acoustic properties depend on their geometries, not on the materials they are made of. Future research steps could involve optimizing structures of acoustic metamaterials to maximize absorption effectiveness in such contexts and exploring advantageous industrial manufacturing methods for this purpose, creating a sample of AMM ceiling to be installed in the hospital room to quantify its effect in a real-world context.

## Summary

This chapter describes the design and application of a metamaterial for the acoustic treatment of a hospital room. Firstly, a characterization of noise in the hospital setting was conducted. Specifically, two sound pressure level (SPL) monitoring sessions were carried out in two hospital rooms: one under active conditions and another empty, located in a temporarily closed ward where only HVAC systems were operating. The monitoring results were compared with the limits suggested by the World Health Organization (WHO) for recommended equivalent noise levels in a hospital environment, demonstrating that the limits were exceeded in both environments, both for equivalent levels and maximum pressure levels, during

the night and day. Additionally, a reverberation time measurement campaign was conducted in the empty room according to ISO 3382-2. Furthermore, a clustering analysis was performed on the data collected from the monitoring in the occupied room. This allowed for a qualitative analysis of different sound sources within the active room.

With the noise characterization, a spectrum to focus the metamaterial design for absorption was obtained, and the range between 500 and 1000 Hz was taken as a reference. At this point, the development and design of a metamaterial for absorption in this frequency range were carried out. First, a unit cell for broadband absorption was developed analytically, numerically, and physically realized through fused deposition modeling. The unit cell sample was characterized and measured in the impedance tube. The obtained results in terms of absorption coefficient were used as input for an additional hybrid numerical model FDTD/GA, used as a validation. The model, calibrated through experimental reverberation time measurements, was developed considering a ceiling of replicated metamaterial unit cells. The simulation results confirmed that using the metamaterial contributes to lowering the reverberation time within the environment. This solution could represent a valid alternative to traditional fibrous and porous absorbent materials, which are challenging to apply in a critical environment regarding hygiene and maintenance, such as a hospital.

# Chapter 4

# Application on loudspeaker systems

The continuous pursuit of high-fidelity audio reproduction has fueled innovation in loudspeaker technology [119]. Over the past decades, researchers and loudspeaker manufacturers have explored various materials, driver designs, and configurations to improve efficiency and performance [120]. Specifically, there has been a quest for new methods to enhance speakers' audio quality while minimizing the portion of sound energy emitted by speakers that do not contribute positively to sound emission, thereby impacting the linearity of loudspeakers. The challenge involves either absorbing the energy emitted from the rear of the transducers or eliminating potential resonances generated by the air volumes within cabinets and enclosures. To surpass the application of fibrous and porous materials as absorbents, which do not ensure optimized absorption for low frequencies and require substantial volumes, engineers have shifted their attention to leveraging the characteristics of metamaterials for this purpose [42, 121, 44, 122]. This study will consider two cases. The first case involves developing a metamaterial to absorb the radiation emitted from the rear of a tweeter, whose enclosure contributes to reflecting sound energy, subsequently impacting the linearity of the frequency response. The second application focuses on acoustic metamaterials for a vented port loudspeaker. In this case, the challenge is to reduce resonances emitted from the reflex port due to the generation of stationary waves inside the cabinet.

## 4.1 Tweeter for high frequencies

A tweeter is a specialized transducer in audio systems designed to handle and reproduce high-frequency sounds, typically those above 1000 Hz and extending

into the frequency range 20-25000 Hz. Its primary function is to ensure the clarity and precision of treble frequencies, contributing to a well-balanced audio output. At its core, a tweeter converts electrical signals into sound waves. It comprises a diaphragm, a lightweight and rigid component often made of silk, metal, or ceramics. This diaphragm is connected to a voice coil, a wire coil suspended within the magnetic field of a magnet. When an electrical signal passes through the voice coil, it interacts with the magnet's field, resulting in the rapid back-and-forth movement of the diaphragm. Surrounding the diaphragm is a suspension system that allows controlled movement while maintaining the diaphragm's position within the magnetic field. This system typically includes a surround (a flexible edge) and a spider (a flexible structure at the base of the diaphragm). The magnet assembly provides the magnetic field against which the voice coil operates. This magnetic interaction is essential for converting electrical energy into mechanical motion, ultimately driving the diaphragm. A crossover network is employed in multi-driver speaker systems to direct specific frequency ranges to different drivers. The crossover ensures that low-frequency signals are directed to woofers, midrange frequencies to appropriate drivers, and high-frequency signals to the tweeter. This optimization helps each driver, including the tweeter, perform efficiently within its designated frequency range. These components' design and material choices collectively influence the tweeter's performance characteristics, such as frequency response, sensitivity, and distortion. Through the intricate interplay of these elements, tweeters contribute significantly to the faithful reproduction of high-frequency content, enhancing the overall fidelity and clarity of audio in a speaker system.

Typically, the bottom of the tweeter's magnetic assembly is isolated by an enclosure, a meticulously designed structure for this purpose. It serves to control the acoustic environment around the tweeter, influencing its performance and ensuring optimal sound reproduction. The enclosure should manage factors like resonance, diffraction, and interference from the reflection of the portion of sound energy emitted to the rear of the tweeter. For this reason, the enclosure's design has always been a critical aspect of tweeter engineering, as crucial as the magnetic components and materials used. Typically, efforts have been directed toward shaping the enclosure or incorporating fibrous materials to control reflections. However, in both cases, these solutions do not ensure the complete absence of reflections, which, once emitted forward, can degrade the tweeter's frequency response, causing destructive or constructive interferences that alter the sound, introduce undesired

colorations, or induce resonances. This section outlines the development of an acoustic metamaterial aimed at broadband absorption to absorb the portion of sound energy emitted rearward. The goal is to design a compact structure positioned inside the enclosure.

### 4.1.1 Case study

The case under study is a 26 mm dome tweeter designed for emitting high frequencies. The operating range is between 1000 and 30000 Hz, with a resonance frequency around 520 Hz.

Fig. 4.1 Photographs of the tweeter under study: on the left, a frontal view of the tweeter featuring the flange, the waveguide, and the diaphragm. On the right is the enclosure that separates the rear of the tweeter from the surroundings.

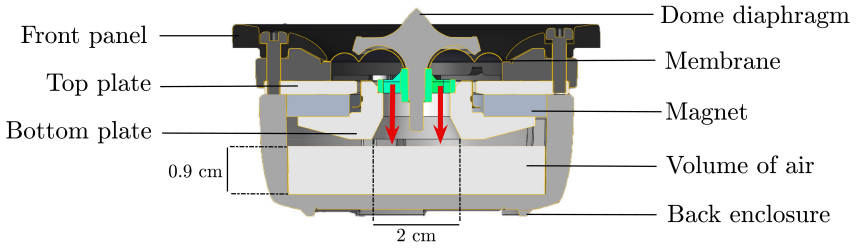


Fig. 4.2 3D sketch of the side section of the tweeter under study, with a description of all its components: red arrows indicate the rear radiation of the tweeter which propagates within the duct of the magnetic circuit. In the illustration, the available air volume for the application of metamaterial is highlighted.

The Thiele-Small parameters of the driver given by the manufacturer are listed in the Table 4.1. The tweeter has the enclosure shown in Figure 4.1: typically, enclosures of this type are generally filled with porous material to absorb the rear radiation.

However, fibrous materials do not ensure the absorption of mid-frequency emissions, especially considering the thicknesses that can be inserted inside. The enclosure cavity has a thickness of 1.5 cm. This thickness is insufficient to accommodate an adequate thickness of fiber to absorb the rear radiation. Indeed, taking into account the definition of Eq. 1.19, the thickness of the enclosure under consideration might accommodate a layer of porous material optimized for frequencies greater than 5700 Hz.

Table 4.1 Thiele-Small parameters, measured in free air, of the 2" tweeter.

| **T&S parameter** | **Nominal** | **Value** |
|---|---|---|
| C resistance [Ω] | $R_e$ | 3.00 |
| Resonance frequency [$Hz$] | $F_s$ | 520 |
| Moving mass [$g$] | $M_{ms}$ | 0.3 |
| Force factor [$T \cdot m$] | $Bl$ | 2.80 |
| Mechanical Q-factor | $Q_{ms}$ | 2.90 |
| Electrical Q-factor | $Q_{es}$ | 0.38 |
| Total Q-factor | $Q_{ts}$ | 0.33 |
| Equivalent air volume [$l$] | $V_{as}$ | 0.01 |
| Inductance of voice coil [$mH$] | $L_e$ | 1.69 |
| Diaphragm area [$cm^2$] | $S_d$ | 5.60 |
| Efficiency [%] | $\eta_0$ | 0.66 |

### 4.1.2 Design of the metamaterial

For the specific purpose of this application, the idea was to design a multi-resonant structure composed of numerous and different Quarter-Wave Resonators (QWR) in parallel to achieve broadband absorption. The starting point is the volume of the available space inside the enclosure where the metamaterial is to be placed, as shown in Figure 4.3. Despite the larger front panel, the available surface for designing the open ends of the resonators was limited to a circular area with a 2 cm diameter – equivalent to the diameter of the opening in the tweeter's magnetic assembly, which acts as a waveguide for the sound energy emitted by the diaphragm directed towards the back. The first step was determining the number of QWRs to implement in the available space. An absorption range between 700 and 3000 Hz was chosen as the target, and 14 resonators were selected to cover this range. Analytically, resonators

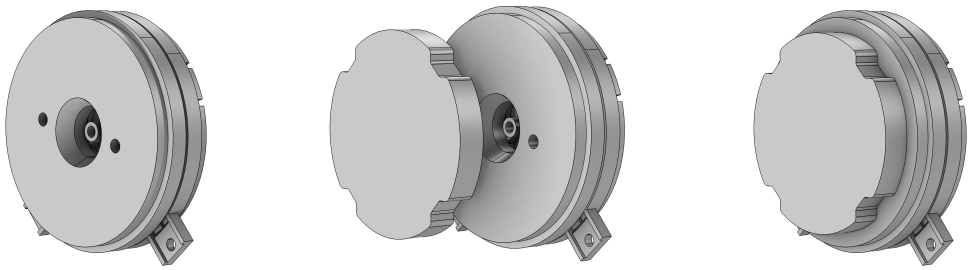

Fig. 4.3 3D sketch of the back part of the tweeter's magnetic assembly: at the center of the magnetic circuit it is possible to observe the open duct where the rear radiation propagates towards the enclosure. In the center and on the right in the figure, the available volume inside the enclosure for the design of the metamaterial to be applied to the back part of the magnetic circuit, aiming to absorb the rearward radiation and prevent reflections.

with geometric dimensions and absorption frequencies were designed as listed in Table 4.2.

The choice was to design a metamaterial with square-based resonators, driven by the bigger simplicity of 3D printing prototyping. Therefore, the geometric parameters considered for the design are $a$, the side of the section, and $l$, the length of the cavity. The sides of the sections were also designed to be of equal dimensions, striking a balance between acoustic performance and simplifying printing and arrangement of the resonators within the available volume. A numerical model was developed in COMSOL, in which the cavity lengths were optimized, and the overall absorption coefficients of the multi-resonant system were simulated. A circular impedance tube model, with a diameter equal to the central hole in the lower plate of the tweeter's magnetic assembly, was created to maintain the ratio between the total surface area and the resonator surface area equivalent to the real case, as shown in Figure 4.5.

### 4.1.3 Prototyping

As described in the preceding section, the available volume resulted in the metamaterial exhibiting Quarter-Wavelength Resonators with a very small square cross-section, with a side of 2.5 mm. Five resonators with the lowest resonance frequency, i.e., those with the longest cavity length, were designed on the second level of the metamaterial. The remaining nine resonators, with higher resonance frequency and smaller length of the cavity, were developed on the first level. The two levels are separated by an

Table 4.2 Constitutive geometrical parameters of the QWRs designed for the metamaterial to be inserted into the tweeter enclosure. The resonance frequency of each resonator from the numerical model after optimization are provided.

| | $a$ [mm] | $l$ [mm] | $f_{R,Numer.}$ [Hz] |
|---|---|---|---|
| Resonator 1 | 2.5 | 110.0 | 750 |
| Resonator 2 | 2.5 | 100.0 | 820 |
| Resonator 3 | 2.5 | 90.0 | 910 |
| Resonator 4 | 2.5 | 80.0 | 1020 |
| Resonator 5 | 2.5 | 70.0 | 1180 |
| Resonator 6 | 2.5 | 60.0 | 1380 |
| Resonator 7 | 2.5 | 55.0 | 1500 |
| Resonator 8 | 2.5 | 50.0 | 1650 |
| Resonator 9 | 2.5 | 45.0 | 1820 |
| Resonator 10 | 2.5 | 40.0 | 2050 |
| Resonator 11 | 2.5 | 35.0 | 2340 |
| Resonator 12 | 2.5 | 32.5 | 2520 |
| Resonator 13 | 2.5 | 30.0 | 2720 |
| Resonator 14 | 2.5 | 27.5 | 2940 |

intermediate layer of material with a height of 1 mm (Figure 4.6). For prototyping, resin stereolithography (SLA) was chosen, a method outlined in the methodology section of this thesis. The SLA method allowed for greater precision and improved quality of internal cavities. The sample is depicted in Figure 4.7, featuring a thickness of 7 mm and a variable section designed to fit into the tweeter's enclosure. The transparency of the resin allowed for the verification of the quality of the coiled-up internal cavities of the QWRs, which develop on two different levels, each separated by a 1 mm wall.

### 4.1.4 Frequency response measurements

For this case study, it was not possible to use impedance tube measurements due to the size of the acoustic metamaterial sample. To evaluate the effectiveness of the metamaterial, the tweeter was mounted on a panel acting as an infinite baffle, and the frequency response was measured in an anechoic chamber, as shown in Figure 4.8. These experimental measurements were conducted using CLIO software, which is recognized as the standard for loudspeaker frequency response measurements. An exponential sine sweep was used as the excitation signal, and the microphone was placed at 8 cm and 25 cm from the tweeter. The frequency response of the tweeter was measured in three different configurations for comparison:

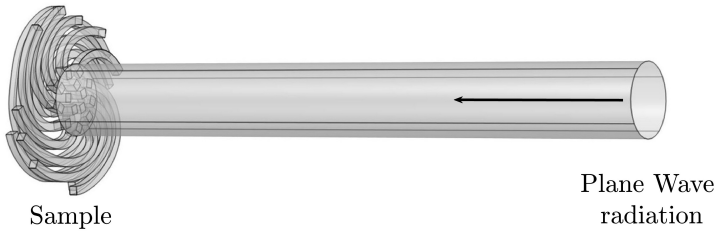


Fig. 4.4 Schematic drawing of the numerical model to simulate the acoustical behavior of the multi-resonant metamaterials. The openings of the QWRs are positioned across the available area of diameter 2 cm, while the cavities are developed on two levels, utilizing the entire available space within the tweeter's enclosure.

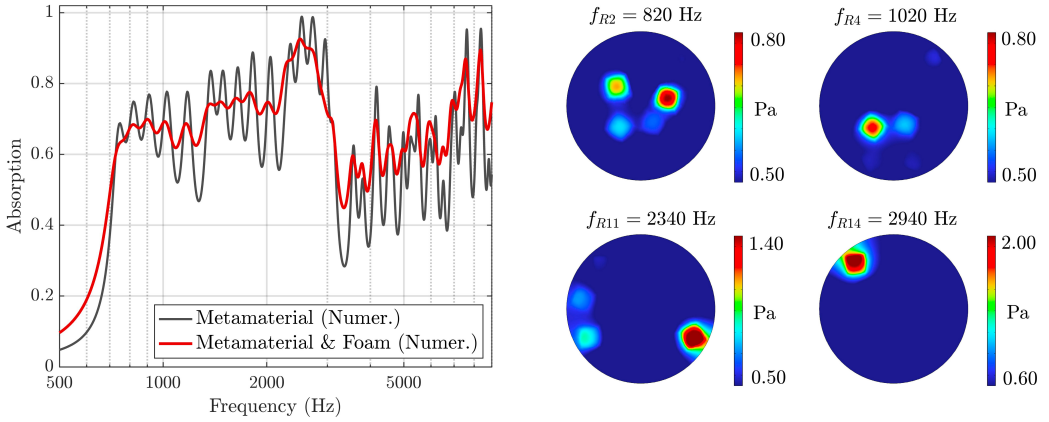


Fig. 4.5 (Left) Numerical results of the sound absorption coefficient of the metamaterial (black line), and the metamaterial with a 3 mm polyster fiber layer (red line). (Right) The distribution of sound pressure $|p|$ visualized at the opening of the resonator at four different resonant frequencies: $f_{R2} = 820$ Hz, $f_{R2} = 1020$ Hz, $f_{R2} = 2340$ Hz, $f_{R2} = 2940$ Hz.

- Measurement with the standard empty enclosure (Blue lines);
- Measurement with the enclosure filled with 1 cm of polyester fiber with a density of 50 $kg/m^3$ (Red lines);
- Measurement with the metamaterial covered by a thin layer of polyester fiber of 1 mm (Yellow lines);

A comparison between the three solutions measured at a distance of 8 cm is reported in Figure 4.9. Below the cutoff frequency at which the tweeter is designed to be filtered in post-processing, around 1000 Hz, the metamaterial lowers the SPLs.

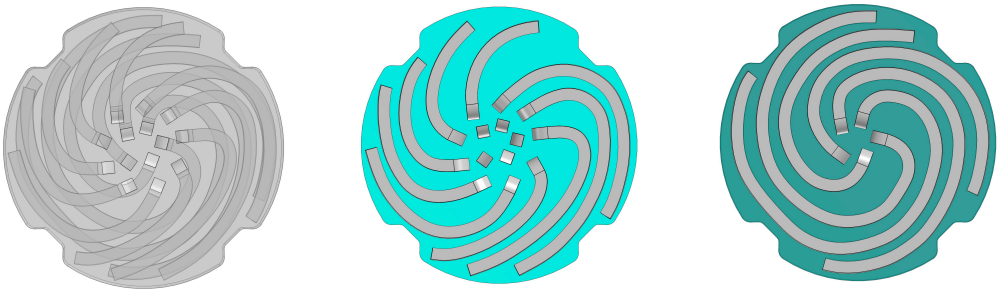

Fig. 4.6 3D sketch of the metamaterial: (Left) Front panel; (Center) the first level with nine coiled QWRs; (Right) the second level with five coiled-up QWRs.

Fig. 4.7 Pictures of the metamaterial sample produced in resin through Stereolithography (SLA). The sample has a thickness of 8 mm and has been designed to be placed inside the tweeter's enclosure.

Moreover, the most interesting point in comparing the frequency responses in various enclosure setups is the behavior around 1300 Hz: it can be observed that even the polyester fiber contributes to increasing the SPL by approximately 0.5 dB around this frequency. On the other hand, the metamaterial allows for greater absorption of the rear radiation, resulting in an increase in sound pressure level of 3 dB and a significant flattening of the frequency range across the tweeter's cutoff frequency. A similar analysis can be made to the frequency range from 2000 to 5000 Hz: the polyester fiber helps slightly improve the frequency response's flattening. However, the measurement with the metamaterial significantly improve the frequency response, reducing resonances due to rear radiation that, in turn, generates constructive and destructive interference in this frequency range. The frequency responses of the three enclosure setups remain almost unchanged in high frequency. In terms of phase, adding fibrous material or inserting the metamaterial does not cause substantial changes.

Fig. 4.8 Photographs of the tweeter mounted in the baffle for frequency response measurements: (Left) the front view of the tweeter; (Center) the rear view of the tweeter; (Right) Measurement setup used in the anechoic chamber, including the tweeter in the baffle and the microphone at a distance of 25 cm.

Figure 4.10 shows the frequency response and phase measurements at a distance of 25 cm, for the three configurations. In this case, an improvement in SPL with the metamaterial is visible. There is a consistent increase in SPL from above 700 Hz up to 1300 Hz. Furthermore, the flattening of the response is significantly greater with the metamaterial than with the empty or polyester-filled enclosure. There is an SPL increment around 2500 Hz and a reduction in resonance around 5000 Hz. In high frequencies, there are differences in frequency response among the various setups, likely due to small displacements of the sample relative to the microphone, which are accentuated by the directional emission of sound at high frequencies.

The benefits of adding the metamaterial to the enclosure are less evident in the measured frequency response at a distance of 25 cm, as shown in Figure 4.10 , especially in the medium-low frequency range. This is mainly due to the fact that the measurement at a bigger distance is more susceptible to the effects generated by the presence of the baffle in which the transducer is installed during the measurement. Indeed, the baffle does not ensure the ideality of a true infinite baffle, resulting in the presence of reflections of acoustic energy that are more pronounced in a measurement at a distance of 25 cm compared to a measurement in a near field.

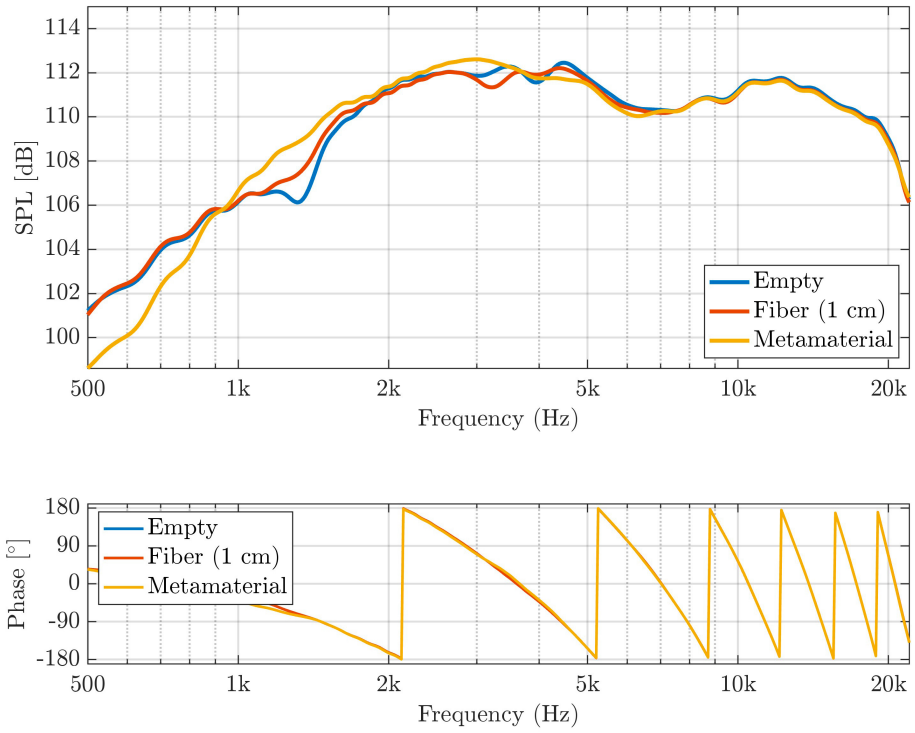


Fig. 4.9 Frequency response (Top) and phase response (Bottom) of the tweeter under study with three different configurations of the enclosure, measured at a distance of 8 cm: classic empty enclosure (blue line), the enclosure with a sample of polyester fiber ($60 kg/m^3$) (red line), and the enclosure with the metamaterial sample (yellow line). A drastic flattening of the overall response with the metamaterial compared to the other two configurations is evident, along with a clear SPL increase of at least 3 dB around the frequency of 1300 Hz. At this frequency, the rear radiation causes destructive interferences with the direct radiation of the tweeter, resulting in a reduction in sound emission.

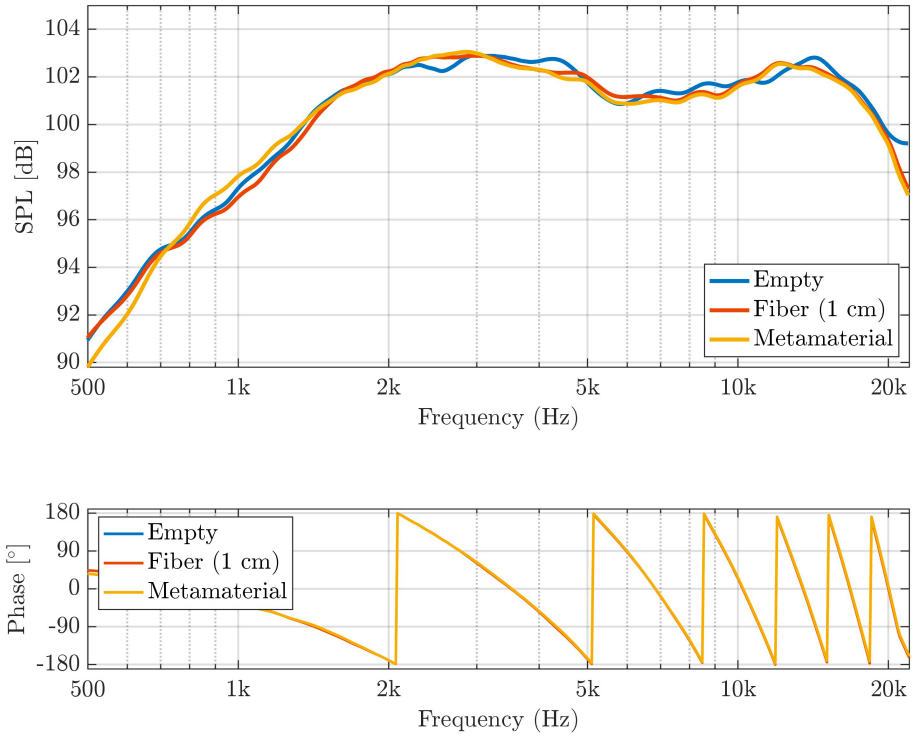


Fig. 4.10 Frequency response (Top) and phase response (Bottom) of the tweeter under study with three different configurations of the enclosure, measured at a distance of 25 cm: classic empty enclosure (blue line), the enclosure with a sample of polyester fiber ($60 kg/m^3$) (red line), and the enclosure with the metamaterial sample (yellow line). Even at a greater measurement distance, it is possible to observe a flattening of the frequency response in the setup with metamaterial in the enclosure. There is an increase in SPL around 2500 Hz and, at the same time, a reduction in resonance due to rear radiation around 4000 Hz.

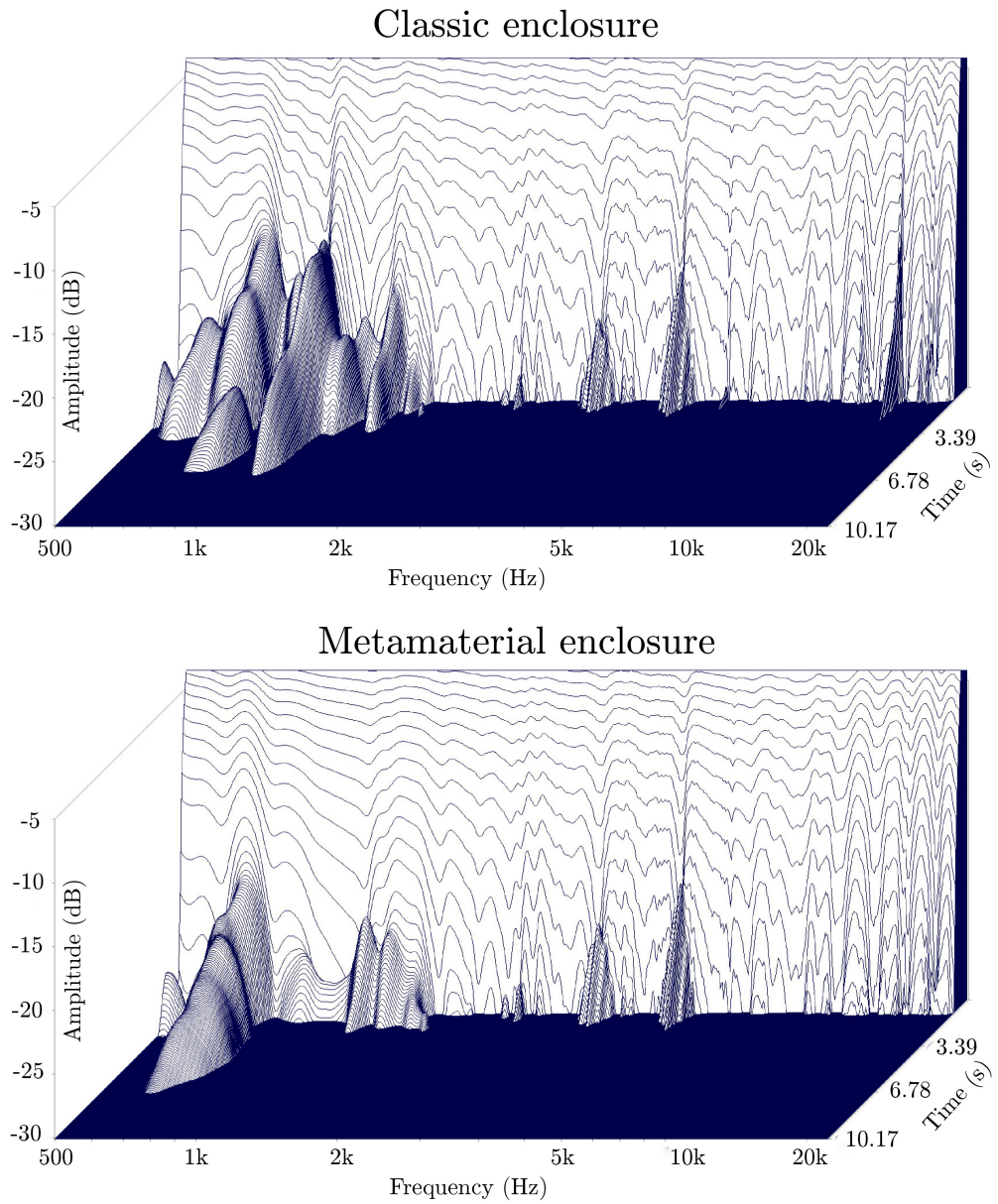


Fig. 4.11 Waterfall representations of measurements taken at a distance of 8 cm from the tweeter in two measurement configurations: (Top) with the classic enclosure and (Bottom) with the metamaterial enclosure. The transients between 800 and 2000 Hz are significantly reduced by at least 5 ms with the metamaterial. There are slight differences around 15 kHz at high frequencies, which may also be attributed to small measurement variations.

A further analysis using a waterfall plot was conducted to provide detailed insight into the frequency response in the time domain of the tweeter. This 3D representation, as depicted in Figure 4.11, illustrates how the system's frequency response changes over time, highlighting the effects of investigated transients and resonances. The two graphs depict the waterfall of the tweeter with the empty classic enclosure and with the enclosure containing the metamaterial in the measurement configuration at a distance of 8 cm. Noticeably, the transients in the frequency range between 800 and 2000 Hz have significantly decreased, both in amplitude and duration, roughly in the order of 5 ms. Transients at high frequencies are not visible in the waterfall plot but remain at an order of magnitude small enough to observe no substantial differences.

## 4.2 Vented-port subwoofer

Bass reflex audio systems, also known as ported or vented speakers, have gained prominence for their capacity to produce deep low frequencies. They employ a specific design incorporating a port or vent into its design, essentially a tuned opening in the enclosure. The working principle is based on the driver producing sound waves, and a portion of these waves is directed into the enclosure. Simultaneously, the port allows a controlled amount of air to escape from the enclosure, typically tuned to a specific frequency. The interaction between the sound waves inside the enclosure and those exiting through the port improves low-frequency performance. The frequency extension comes exploiting the Helmholtz resonator created by the compliance of the air inside the cavity and the inertance of the air in the reflex [123]. If losses are not considered, the working frequency of the bass reflex can be defined as:

$$f = \frac{c}{2\pi}\sqrt{\frac{S}{VL}} \tag{4.1}$$

Where $c$ is the speed of sound, $S$ is the port cross-sectional area, $V$ is the volume of the reflex cavity, and $L$ is the length of the port. This design offers several advantages over non-reflex systems. They enhance the maximum acoustic output, present a higher overall efficiency, and reduce harmonic distortion at low frequencies, enhance maximum sound pressure level, and minimize cabinet size [124, 125, 123, 126]. While popular in various audio applications, from large-stage subwoofers to high-fidelity studio monitors, they present challenges. Stationary waves generated inside these systems' cabinet volumes can disrupt sound emission through the reflex port [127–129]. To address these challenges, contemporary solutions incorporate fibrous and porous materials within cabinets to manage unwanted resonances [130–133]. However, these materials have limitations, often being frequency-restricted, requiring maintenance, and demanding substantial thickness and volume for efficiency in the mid and low-frequency ranges. The present section of this study investigates and proposes the application of acoustic metamaterials (AMMs), specifically Quarter Wavelength Resonators (QWR) on a loudspeaker with a vented port. AMMs are enginereed structure that can manipulate sound waves in unprecedented ways [134], and can offer a alternative and more efficient solution than traditional porous materials for this kind of issue. The aim is to reduce the effect of the standing waves and resonances coming from the cabinet's shape. In any case, the method

demonstrated in this study may be replicated for any monitor equipped with a bass reflex, optimizing the structures for the frequency range of interest.

### 4.2.1 Case study

The investigation is focused on the performance of a subwoofer system comprising a 12" cone driver and a reflex-ported enclosure for handling low-frequency signals (Figure 4.12). The bass reflex has a horn-like structure and is located at the bottom of the speaker. The internal geometrical dimensions of the cabinet are the following: a height $h_{box} = 495$ mm, a width $w_{box} = 365$ mm, and a length $l_{box} = 345$ mm. The Thiele-Small parameters are a set of parameters that describe the electrical and

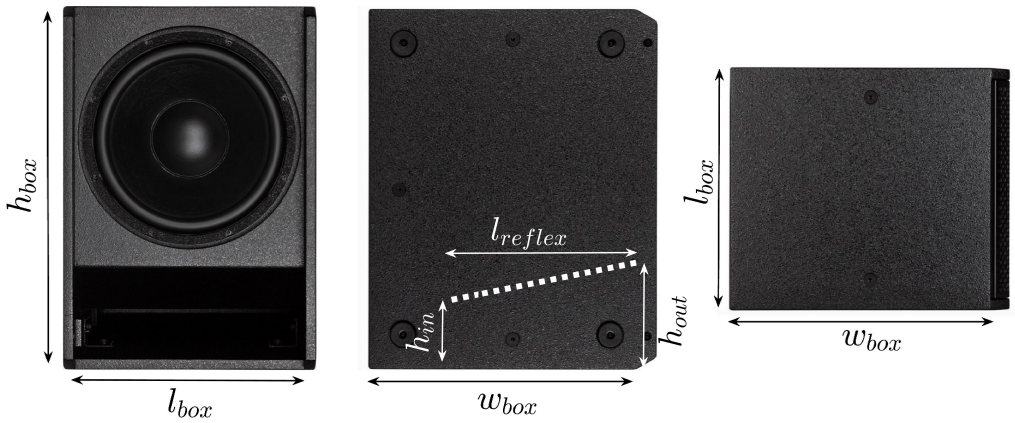


Fig. 4.12 Picture of the subwoofer under study: a 12" cone driver is mounted on a wood cabinet. A vented port is designed to enhance the low-frequency range.

mechanical characteristics of a speaker. These parameters are commonly used in the design and modeling of speakers and are reported in Table 4.3. The primary focus lies in examining the unfiltered frequency response of this system, shown in Figure 4.13, and revealing a phenomenon characterized by numerous resonance peaks in sound pressure level (SPL). This phenomenon is most prominently evident in the frequency response measured at the reflex port's output (dark grey line). However, its influence significantly affects the overall subwoofer response. The interaction of these acoustical resonances within the reflex port and cabinet alters the system's response and presents a unique challenge in achieving a flat and accurate low-frequency reproduction.

Table 4.3 Thiele-Small parameters, measured in free air, of the 12” subwoofer driver.

| T&S parameter | Nominal | Value | Toll. | Min | Max |
|---|---|---|---|---|---|
| C resistance [Ω] | $R_e$ | 5.72 | 10% | 5.15 | 6.29 |
| Resonance frequency $[Hz]$ | $F_s$ | 49.1 | 15% | 41.7 | 56.5 |
| Moving mass $[g]$ | $M_{ms}$ | 124.8 | | | |
| Force factor $[T \cdot m]$ | $Bl$ | 19.5 | | | |
| Mechanical Q-factor | $Q_{ms}$ | 8.04 | | | |
| Electrical Q-factor | $Q_{es}$ | 0.58 | | | |
| Total Q-factor | $Q_{ts}$ | 0.54 | 15% | 0.46 | 0.62 |
| Equivalent air volume $[l]$ | $V_{as}$ | 33.6 | | | |
| Inductance of voice coil $[mH]$ | $L_e$ | 1.69 | | | |
| Diaphragm area $[cm^2]$ | $S_d$ | 530.9 | | | |
| Efficiency $[\%]$ | $\eta_0$ | 0.66 | | | |

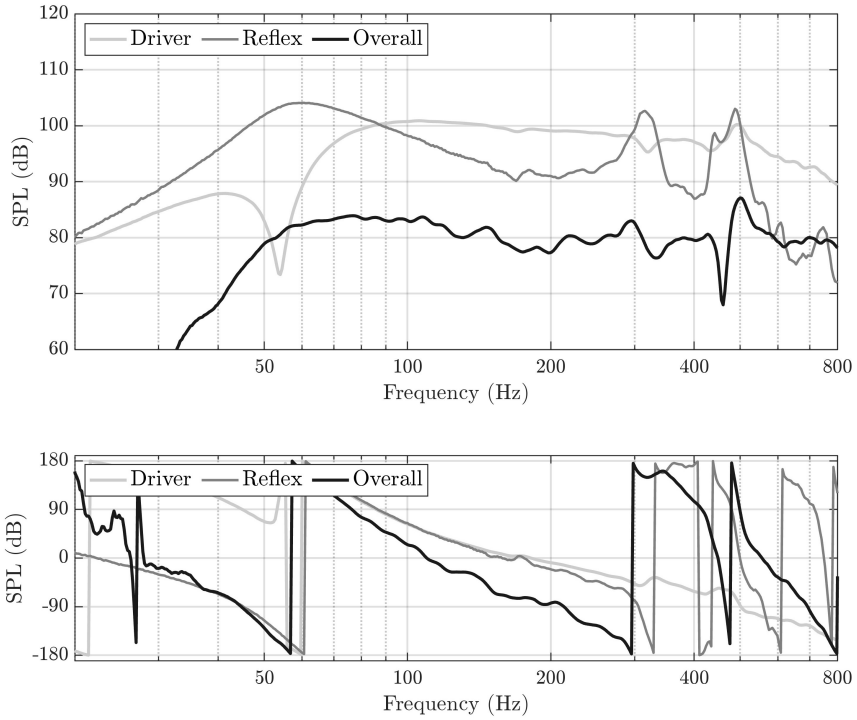


Fig. 4.13 The frequency response of the subwoofer was measured in front of the woofer (light grey line), at the opening of the bass-reflex (dark grey line), and the overall response at a distance of 0.25 m from the woofer (black line).

### 4.2.2 Resonance investigation

The resonances originate from standing waves that show within the cabinet and reflex port, significantly impacting the system's overall output. Specifically, the prominent peaks around $f_{R1} = 440$ Hz and $f_{R2} = 490$ Hz indicate standing waves within the cabinet cavity. To validate this observation, given the complexity of the cabinet's geometry, a numerical simulation was conducted using a simplified model of the subwoofer system to identify the natural frequencies of the enclosed volume. As depicted in Figure 4.14, these two frequencies correspond respectively to the first axial mode along the X-axis and the first axial mode along the Z-axis. This correlation between the measured peaks and the modal frequencies provides compelling evidence of the acoustical resonances within the cabinet, shedding light on the origins of the observed frequency response anomalies.

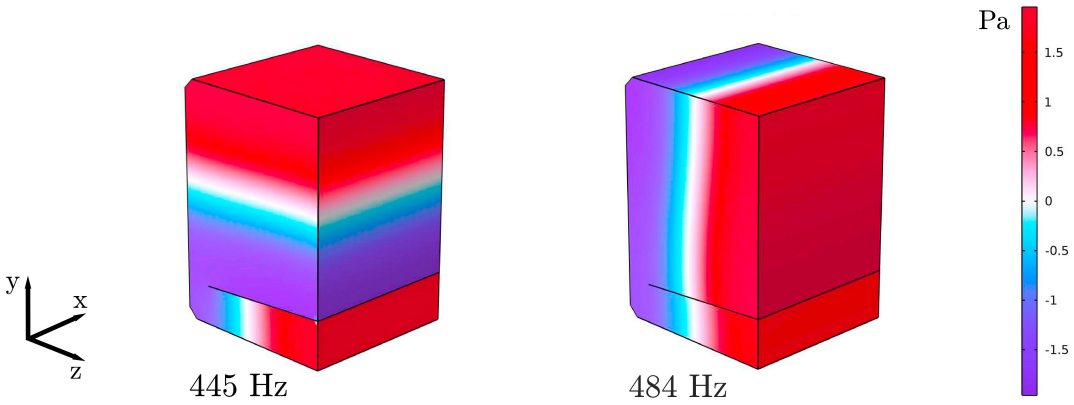


Fig. 4.14 The acoustic pressure for the eigenfrequencies corresponding to the modal resonances of the cabinet.

An intriguing point of interest lies in the resonance observed at $f_{R3} = 318Hz$. This resonance peak seems not to derive directly from an eigenfrequency of the cabinet. Instead, it could be attributed to vortex shedding of the acoustical flow at the port's end when flow velocities are high [135]. It is independent of the speaker's emission and, instead, reflects the behavior of the reflex ports, which exhibits non-linear characteristics [127]. Around this frequency, losses and unwanted noise emissions are generated due to turbulences and flow separation at the reflex's inlet and outlet. The resulting non-linear acoustic losses for a specific reflex volume and geometry should take into account the resonance frequency of a variable cross-

section port. This resonance is related to the port's shape and depends on an effective length of the reflex [129]. It is possible to analytically verify this resonance requires calculating an end correction to be added to the length of the port to account for the mass of air moving in and out of the reflex port. This effective length can be expressed as:

$$L_{eff} = \int_{L}^{0} \frac{S_0}{S(x)} dx \tag{4.2}$$

where $S_0$ is the cross-sectional area of the reflex and $V$ the enclosure volume, and $L$ is the physical length of the reflex, and $S_x$ is the cross-sectional area at axial coordinate x. This effective length is used to consider the mass of moving air at the opening of the reflex. The resonance clearly visible in the frequency response of the sub-woofer does not depend on the emission of the woofer but it comes from the periodic vortex shedding which gives rise to a periodic excitation, and can be analytically defined as [136]:

$$f_n = \frac{nc}{2L_{eff}} \quad \text{for} \quad n = 1,2,3,\ldots \tag{4.3}$$

Taking into account the definition of 4.2, the open pipe resonant frequency $f_{R3} = 315$ Hz corresponds to the $\frac{1}{2}\lambda$ wave in the X-axes of the reflex. Table 4.4 summarizes the resonances due to standing waves inside the cabinet, indicating the cause that generates them, the expected values derived from analytical and numerical calculations, and the frequency values measured in the subwoofer frequency response.

Table 4.4 Summary of the resonances due to the standing waves generated within the cabinet volume, the cause the resonances are generated by, the expected values and the measured values of the resonances.

| **Resonance** | **Cause** | **Num. (Hz)** | **Meas. (Hz)** |
|---|---|---|---|
| $f_{R1}$ | Axial mode (0,1,0) | 437 | 440 |
| $f_{R2}$ | Axial mode (0,0,1) | 484 | 490 |
| $f_{R3}$ | Open pipe | 315 | 318 |

### 4.2.3 Calibration

A numerical model has also been used to address the behavior of the sub-woofer. As shown in Figure 4.15, the model was implemented by coupling two physics: pressure acoustics and structural mechanics. The Thiele-Small parameters of the

driver (measured in free air), as listed in Table 4.3, were used as input for a lumped parameter model [125, 124]. Through this process, the displacement of the driver was

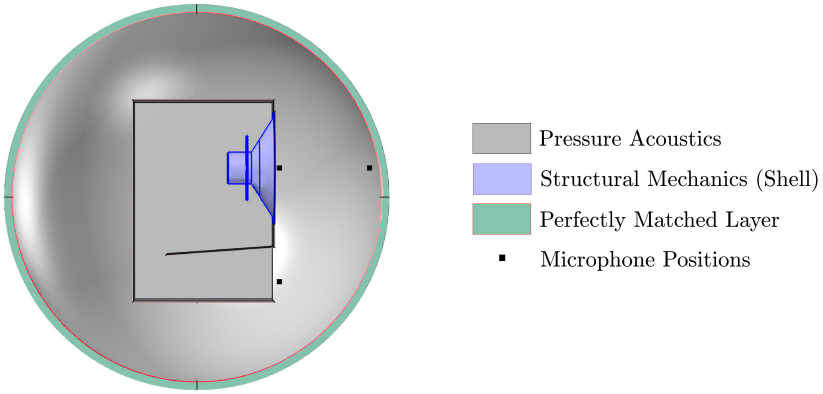


Fig. 4.15 3D sketch of the numerical model developed on Comsol: the subwoofer driver belongs to the Structural Mechanics Physics and the air domain inside and outside the cabinet is calculated as Pressure Acoustics. A Perfectly Matched Layer (PML) is applied to the open boundary of the model. Furthermore, three microphone positions have been considered in the numerical model to assess the SPL in front of the driver, at the opening of the reflex duct, and at a distance of 25 cm from the driver.

obtained to achieve the frequency response of the subwoofer, which was measured in three different positions, taking into account the microphone positions used for the experimental measurements. All walls of the subwoofer were considered to be of negligible thickness to avoid overburdening the model and were treated as perfectly rigid. Additionally, a Perfectly Matched Layer (PML) was applied to an open boundary of the system. Figure 4.16 shows the calibration results of the COMSOL model with the experimental measurements in the two configurations measured at the output of the reflex port and at a distance of 25 cm from the driver. There is a good agreement between the measurements and the numerical model: the working frequency of the woofer and the reflex are underestimated because the TS parameters considered for the study are in free-field.

### 4.2.4 Design of the metamaterial

Once the resonance frequencies to act upon are defined, it is possible to study configurations of acoustic metamaterials to remove them or, at the very least, reduce

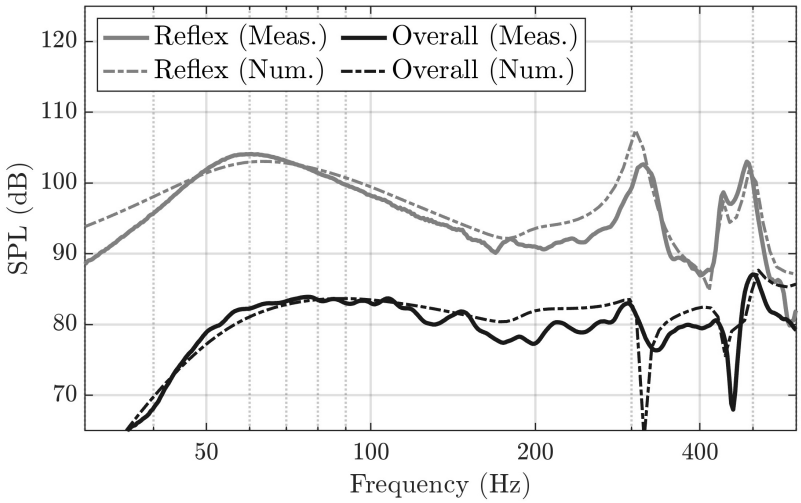


Fig. 4.16 Calibration of the numerical model with the experimental measurement of the subwoofer with the traditional cabinet. The frequency responses measured at the opening of the bass reflex in near-field (grey lines) and the overall frequency response measured at a distance of 0.25 cm (black lines) are reported.

their effect. Acoustic metamaterials based on QWRs can effectively mitigate two distinct resonance types from cabinet geometry. Optimized design and placement within the volumes are critical for their effectiveness. For resonances induced by the stationary waves generated within the cabinet cavity $f_{R1}$ and $f_{R2}$, the concept involves developing a metamaterial to be applied to the inner wall opposite the rear of the driver (Figure 4.17). The goal is to achieve perfect absorption of resonance peaks while preserving the propagation of rear radiation, which contributes to the output of the reflex port. Therefore, to achieve maximum absorption, it is necessary to optimize the losses by impedance matching, whether due to viscous dissipation or thermal effects within the resonators. Regarding the resonance $f_{R3}$ caused by the geometry of the reflex itself, placing a metamaterial inside the cabinet cavity is not an effective solution, as the resonance occurs within the reflex duct. The idea is to leverage the space available on the bottom wall of the reflex, as shown in Figure 4.17. In this case, the aim is to reduce the sound wave transmission at the resonance frequency without disrupting the outgoing airflow toward the reflex outlet. In a real-world scenario, achieving zero transmission is an ideal concept due to losses. However, minimizing transmission at a specific frequency is feasible by reducing viscous dissipation and thermal dissipation and optimizing the ratio between the

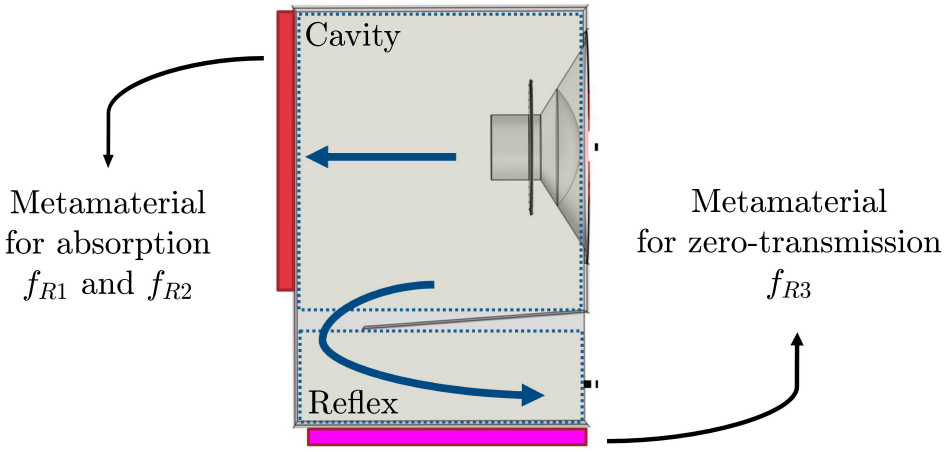


Fig. 4.17 3D sketch of the cabinet: highlighted in red, the placement of the array of AMMs for the absorption of the resonances $f_{R1}$ and $f_{R2}$; highlighted in violet, the placement of the array of AMMs for the quasi-zero transmission of the resonance $f_{R3}$.

cross-sectional area of the resonating elements and the total cross-sectional area of the reflex duct [34].

### Single unit-cells

The surface for applying the metamaterial for absorption corresponds to the total surface area of the cabinet's front face where the source, i.e., the subwoofer driver, is installed. A surface area of 34.5 cm x 34.5 cm on the cabinet's back panel has been designated as the total area to be treated with metamaterials. The cut-off frequency of the tube, which coincides with the limit beyond which the plane wave assumption breaks down, can be calculated as follows:

$$f_{cutoff} = \frac{c}{2d} = 497 \quad \text{Hz} \tag{4.4}$$

where $d$ is the side of the cabinet, and $c$ is the speed of sound. This means the limit is close to the resonances that must be eliminated. To simplify the problem and maintain the plane wave assumption, it was necessary to break down the area of interest into smaller unit cells, where higher-order modes could be neglected. This implies raising the cut-off frequency and remaining in the frequency range where the plane wave assumption is valid. The development of a single unit cell of 11.5 cm x 11.5 cm was considered. The cut-off frequency is $f_{cutoff} = 1490$ Hz for these

dimensions. The unit cell should have the target acoustic properties, which will then be replicated in periodic and symmetric structures of the unit cell to cover the entire area of interest. The unit cell for absorption is composed of eight QWRs. Four coiled QWRs are tuned to the resonance frequency $f_{R1} = 440$ Hz, taking shape on a first level. Four coiled QWRs are tuned to the resonance frequency $f_{R2} = 490$ Hz and take shape on a second level (Figure 4.18). The resonators designed for $f_{R1}$ have a total length $L_{n,1} = 169.45$ mm, and a side $a_{n,1} = 8.94$ mm. The resonators designed for $f_{R2}$ have a total length $L_{n,2} = 189.00$ mm, and a side $a_{n,2} = 9.32$ mm.

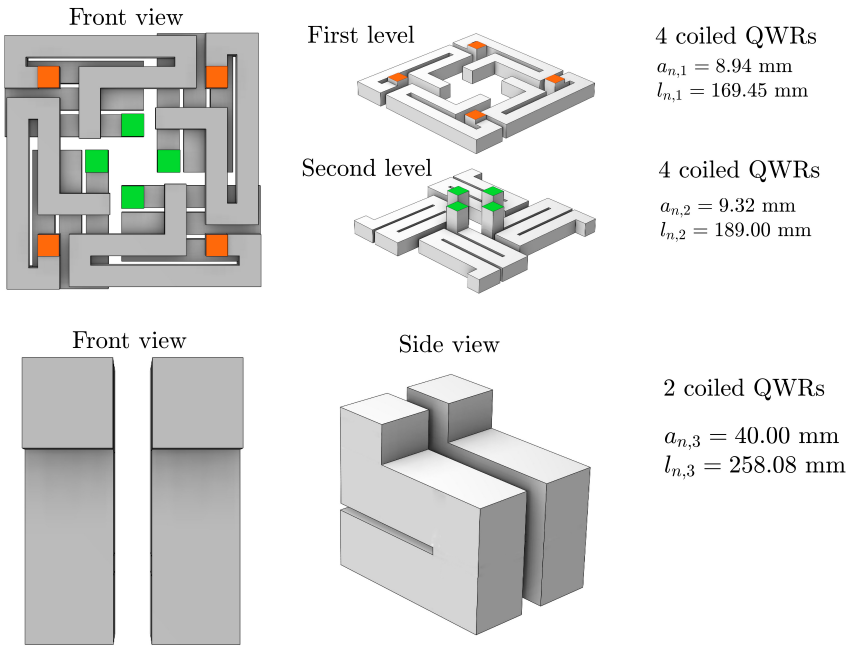


Fig. 4.18 (Top) Fluid path cavity of the QWRs of the unit cell for absorption: four identical coiled QWRs take shape on a first level (the opening are highlighted in orange), and four identical coiled QWRs take shape on a second level (the opening are highlighted in green); (Bottom) Fluid path cavity of the QWRs of the unit cell for zero-transmission: two identical coiled QWRs take shape on multiple levels.

For the zero-transmission issue, it was crucial to consider the waveguide dimension perpendicular to the direction of acoustic wave propagation. For this reason, the width of the reflex port is the target surface to apply metamaterials. In this case, two identical resonators placed in parallel are present in the unit cell, as shown in Figure 4.18. These resonators have been coiled into multiple layers to constrain their dimensions, also in anticipation of 3D prototyping, which involves limiting the print plate size. The resonators have a length $l_{n,3} = 258.08$ mm and a side of

the square section $a_{n,3} = 40$ mm. The geometrical dimensions of the resonators were optimized through numerical simulations on Comsol. The same happened for the number of resonators: employing more than one resonator per type aims to enhance the absorption's Q-factor at each frequency. Furthermore, the position of the resonators' openings has been chosen in such a way as to maintain periodicity and symmetry when the unit cell is replicated. For the absorption unit cell, symmetry and periodicity must be maintained in both development directions, while the symmetry and periodicity of the unit cells for zero transmission must be maintained in the direction normal to the wave propagation. Two numerical models have been developed on Comsol to optimize the unit cells for absorption and zero transmission. A square

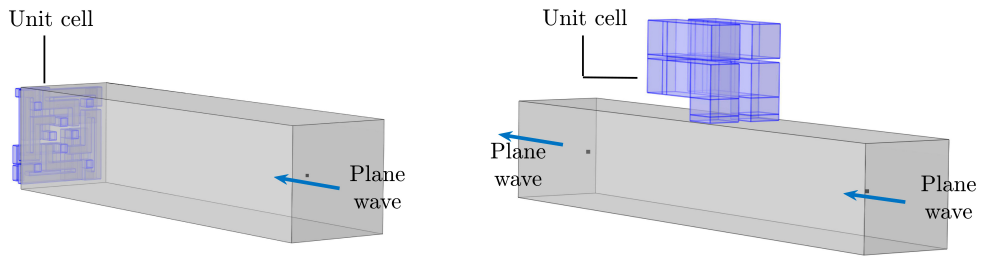


a) Numerical model for absorption b) Numerical model for zero transmission

Fig. 4.19 Numerical models used for simulating the absorption (a) and the tranmission (b) of the unite cells. The unit cells of metamaterials are highlighted in blue.

waveguide has been considered, with a side one-third the width of the cabinet cavity: $h_w = 11.5cm$, and a plane wave radiation surface has been located at one end of the waveguide. For the absorption problem, the unit cell has been placed in series at the other end of the waveguide, as shown in Figure 4.19a. For the transmission calculation, the QWRs have been placed in parallel with the main waveguide, and plane wave radiation has been considered at both ends of the waveguide (Figure 4.19b). Thermo-viscous losses of the resonators have been taken into account thanks to the use of the *narrow region acoustics*. Specifically, it considers losses due to viscous and thermal dissipation in the acoustic boundary layer, which are homogenized and distributed throughout the fluid. Furthermore, the *background pressure field* has been used to model a background/incident pressure wave to study the scattered pressure field and, consequently, to obtain absorption, reflection, and, when required, transmission coefficient values. The boundary condition of the models has been

assumed to be infinitely rigid using the Sound Hard Boundary for the waveguide and the inner walls of the cavity of the resonators.

#### Metamaterial panels

The metamaterial panel for the loudspeaker cavity is a 3x3 array of unit cells for absorption. The total size of the panel for absorption is thus a square with a side length of 34.5 cm. The metamaterial panel for the reflex port is a 3x1 array of unit cells for zero transmission. The overall size of the panel is 34.5 x 13, reflecting the length of the unit cell in which it was possible to fold the resonators.

Figure 4.20 shows the front panel of the absorption and zero-transmission metamaterials obtained by replicating the unit cells. Additionally, the accuracy of the unit cells replication was verified by analyzing the pressure distribution $|p|$ at the resonators' inlet. Noticeably, the pressure distribution at the resonators' resonance frequencies remains constant even when replicating the unit cells. This also demonstrates the absence of coupling and evanescent waves between resonators of different types that could affect the acoustic properties of the resonators.

### 4.2.5 Prototyping

The QWRs implemented in the unit cells have been coiled up to develop a compact design of the metamaterials. The unit cells optimized for absorption and quasi-zero transmission were 3D printed in two different manufacturing processes: one sample from each category was obtained through fused deposition modeling in PETG, while the others were printed using stereolithography in resin, as shown in Figure 4.21, 4.22.

#### Absorption unit cell

The unit cell designed to address the resonance absorption issue within the internal cavity of the subwoofer was fabricated using the two 3D printing techniques described in the methodology of this thesis. As shown in Figure 4.21, samples made of PET through FDM and resin through SLA were obtained for absorption measurements in the impedance tube. The two printing methods and materials were chosen based on previous work by the authors [32, 137], with optimized settings in terms of print speed and layer height as described in the method of this thesis. The external dimensions and weight of the 3D printed samples with the two production

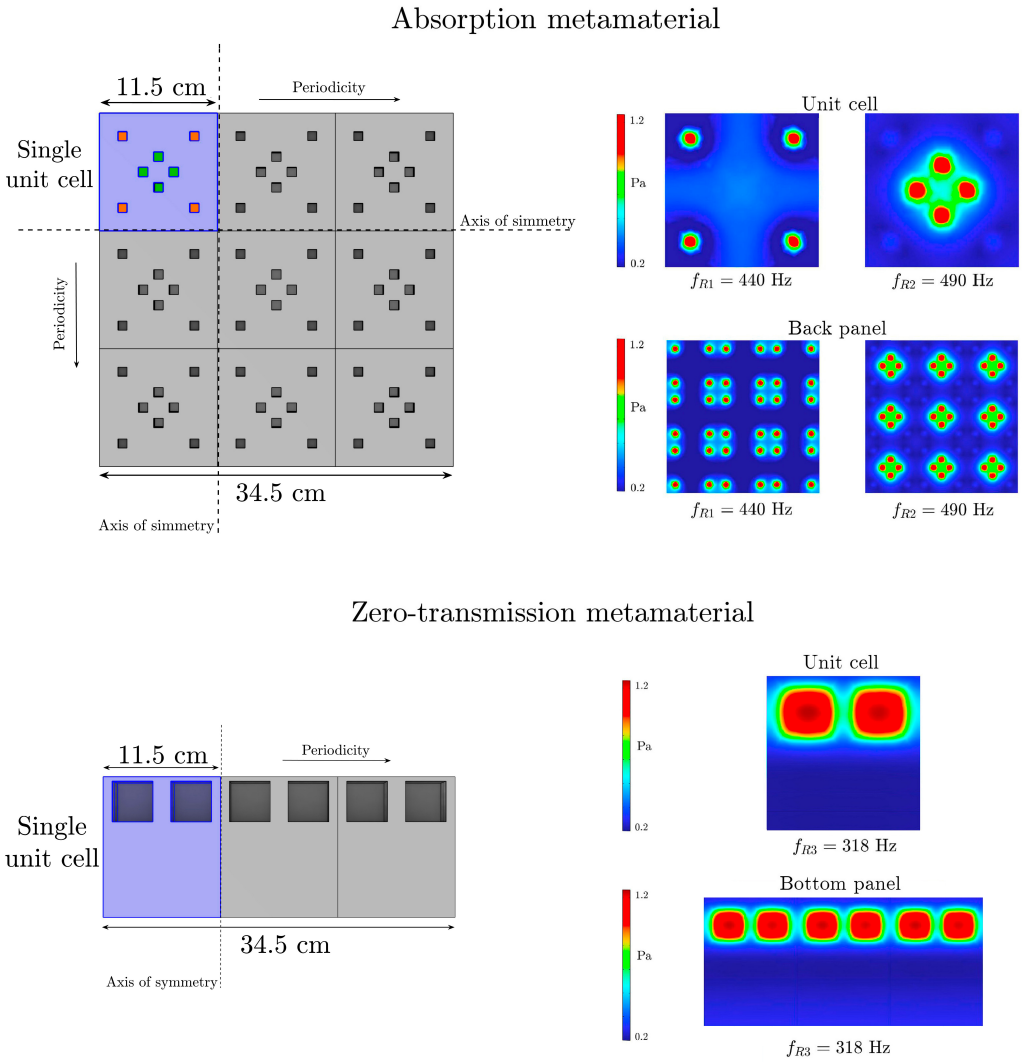


Fig. 4.20 Representation of the front panel of the metamaterial arrays: a 3x3 array of the unit cell designed for perfect absorption, covering the target surface inside the subwoofer cavity. Openings highlighted in orange are identical for absorbing frequency $f_{R1}$, while those in green are identical for absorbing resonance $f_{R2}$. Additionally, a 3x1 unit cell array is designed for zero transmission, covering the area of interest inside the subwoofer's reflex. On the right, a visualization of the distribution of the sound pressure at the resonance frequencies of the unit cells is shown: the pressure at the resonator openings remains unchanged whether analyzed within a single unit cell or across the entire metamaterial panels, and the two types of resonators are not coupled.

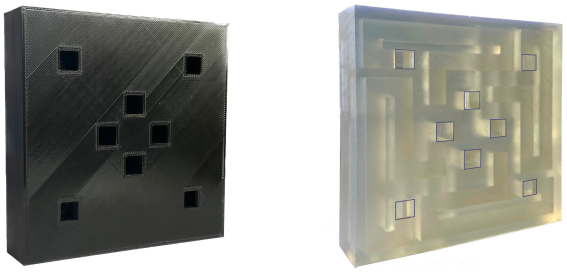

a) PET sample (FDM) b) Resin sample (SLA)

Fig. 4.21 Single unit cell sample, designed for perfect absorption at $f_{R1}$ and $f_{R2}$, printed through Fuse Deposition Modelling in PETg (a) and through Stereolitography in Resin (b).

processes are summarized in Table 4.5. The compact thickness was achieved by

Table 4.5 External dimensions and weight of the 3D printed samples for absorption.

| Printing method | Side (cm) | Thickness (cm) | Weight (g) |
|---|---|---|---|
| FDM | 11.5 | 2.56 | 240 |
| SLA | 11.5 | 2.56 | 400 |

appropriately folding the QWRs. There are a total of eight resonators, four identical ones for each type. Each resonator type is arranged on one level, and a 2 mm layer separates the two levels. The front panel layer measures 3 mm, and the final layer of the sample measures 3 mm.

### Zero-transmission unit cell

Like the previous one, the unit cell designed for zero transmission of the resonance generated within the bass reflex has been manufactured in PET using FDM and in resin using SLA (Figure 4.22). The settings are the same as those used for the absorption samples. The external dimensions of the unit cell are summarized in Table 4.6 In this case, the internal spiral has a side of 4 cm and has been folded twice to fit the space. The resulting final parallelepiped was obtained to fit the size of the printing plate of the available 3D printers. Although not optimized for a real-world application with the goal of minimizing thickness as much as possible, this geometry allowed for obtaining measurable unit cells in the square-base impedance tube, used for transmission loss measurements. The samples have a front panel of 4 mm to

Table 4.6 External dimensions and weight of the 3D printed samples for zero-transmission.

| Printing method | Side (cm) | Thickness (cm) | Weight (g) |
|---|---|---|---|
| FDM | 11.5 | 12.6 | 520 |
| SLA | 11.5 | 12.6 | 850 |

avoid front panel fragility. All internal walls dividing the cavities are at least 3 mm thick.

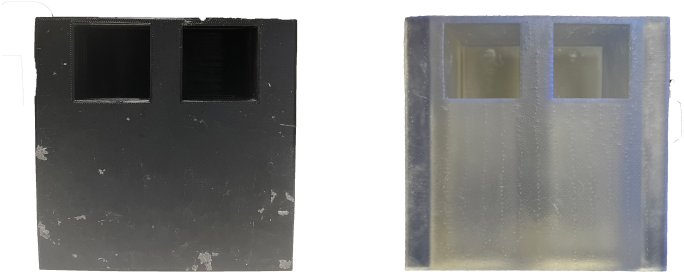

a) PET sample (FDM) b) Resin sample (SLA)

Fig. 4.22 a) Single unit cell sample, designed for quasi-zero transmission at $f_{R3}$, printed through Fuse Deposition Modelling in PETg. b) Single unit cell sample, designed for quasi-zero transmission at $f_{R3}$, printed through Stereolitography in Resin.

### Metapanels

For the realization of metamaterial panels to be inserted into the cabinet, nine unit cells for absorption and three unit cells for zero transmission were produced using SLA. A 3x3 array in the first case and a 3x1 array in the second were manufactured to be directly installed in the cabinet, as shown in Figure 4.23 . The unit cells were glued together to create a uniform surface, avoiding leakage and potential imperfections through careful post-processing. Noticeably, one unit cell for zero transmission differs in color; this does not entail any acoustic changes. Only a different non-transparent resin was used for the other two unit cells, but the manufacturing process remained unchanged. The choice to print individual unit cells was driven by the fact that producing pre-measured unit cells ensured having a panel of elements whose

acoustic characteristics were already tested through measurements in the impedance tube.

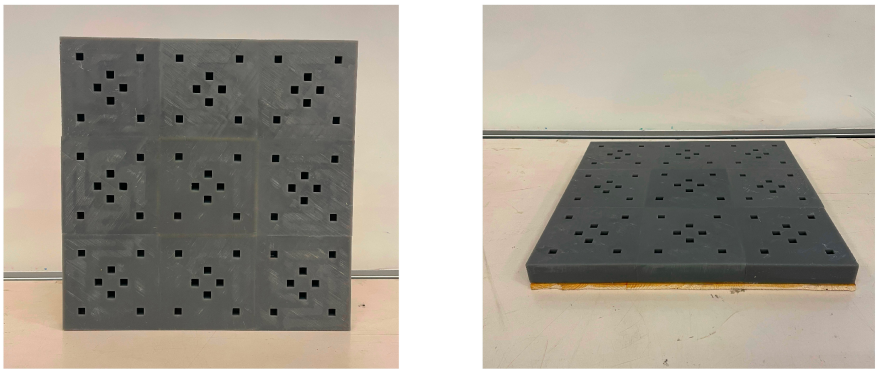

a) Metamaterial panel for absorption

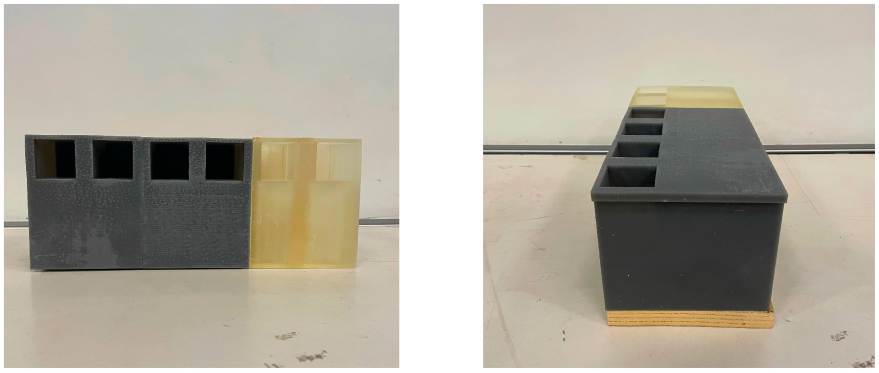

b) Metamaterial panel for zero-transmission

Fig. 4.23 (Top) Photographs of the metamaterial panel for the absorption. The panel is the array 3x3 of the single unit cell for absorption. (Bottom) Photographs of the metamaterial panel for the zero transmission. The panel is a 3x1 array of the single unit cell for zero transmission.

### 4.2.6 Impedance tube measurements

The experimental part of this study is based on impedance tube measurements of the single unit cell for the absorption and zero transmission problems and the experimental measurements of the loudspeaker's frequency response. The impedance tube measurements have been performed on a squared impedance tube with a $\approx 12cm$ side and two microphone locations, according to ISO 10534-2 [87]. The collected

pressures at the microphones' locations have been explored to apply the transfer function method to obtain values of sound absorption coefficient, reflection, and transmission coefficient of the metamaterial unit cells developed analytically and optimized through numerical models. The software Matlab has been used to post-process the collected data.

Figure 4.24 illustrates the results of experimental measurements in the impedance tube, in terms of the acoustic absorption coefficient, for two samples obtained through Fused Deposition Modeling (FDM) and Stereolithography (SLA). These results are compared to the analytical and numerical models used to develop the unit cells. Perfect absorption is maintained for the two frequencies of interest, and the absorption curve matches the predictive models.

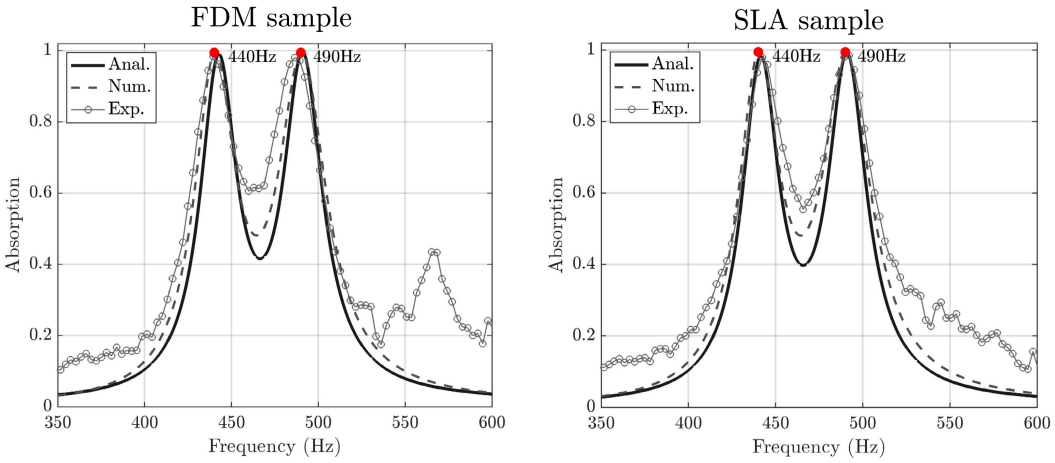


Fig. 4.24 Sound absorption coefficient of the measured unit cell: The results of the measurements are compared with the analytical and numerical models.

Figure 4.25 presents the absorption, reflection, and transmission coefficients of the two unit cells developed for zero transmission, manufactured through FDM and SLA. For both, the transmission coefficient is not equal to 0 but reaches values of 0.2. The discrepancy between the predictive models and the measured value is attributed to real-world scenario factors, introducing losses that increase the transmission coefficient, increasing the absorption of the printed cavity. Specifically, the portion absorbed by the sample as the sound wave passes is greater than the model's predicted one. This behavior is directly linked to the internal roughness and imperfections of the sample's internal conduits, which were assumed to be perfectly rigid in the predictive models, i.e., lossless.

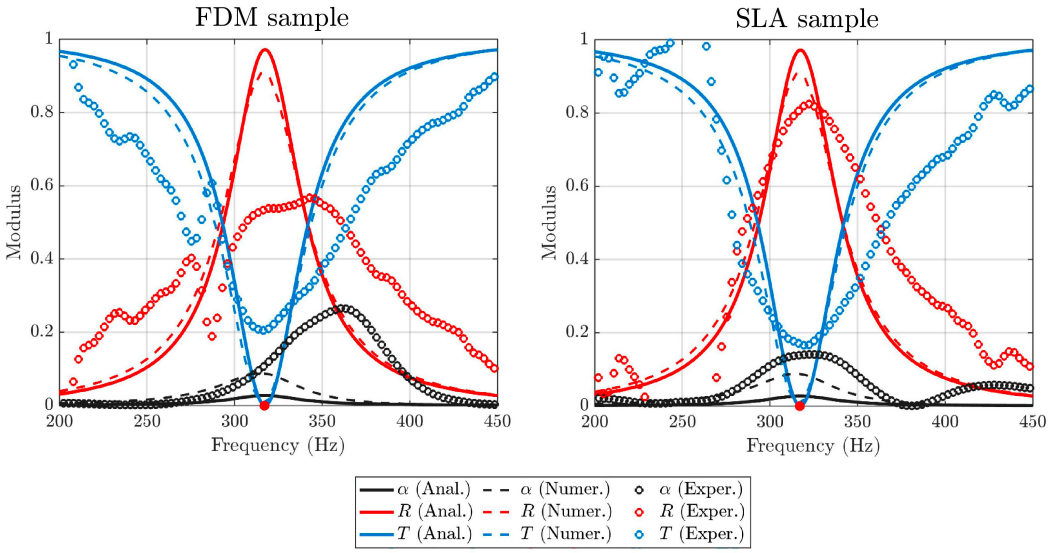


Fig. 4.25 Absorption, reflection, and transmission coefficients of the single unit cells made through FDM and SLA: the results of the measurements are compared with the analytical and numerical models.

### 4.2.7 Frequency response measurements

The samples formed by the arrays of single-unit cells were printed through Stereolithography in resin and assembled. The 3x3 array for absorption, shown in Figure 4.23, was placed at the back of the cabinet cavity, and the 3x1 array consisting of 3 unit cells (Figure 4.26) for zero transmission was positioned on the lower surface of the reflex. The samples were sealed to adhere perfectly to the cabinet walls, preventing any joint leakage (Figure 4.26).

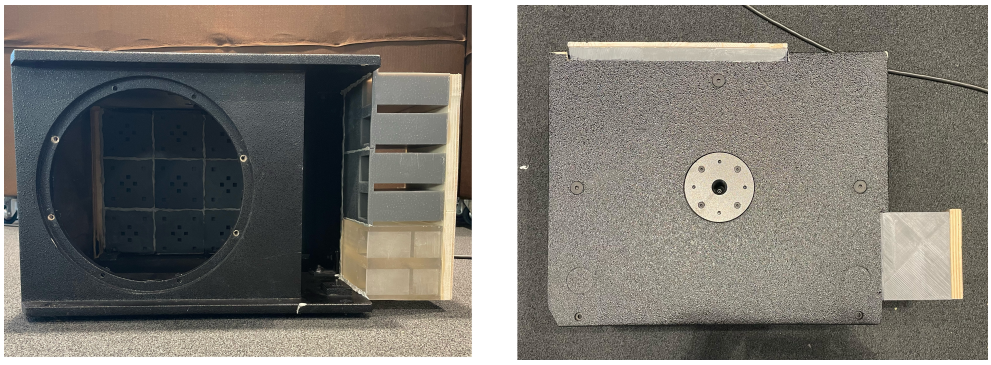

Fig. 4.26 Photographs of the metamaterial panel for the zero transmission. The panel is the array 3x1 of the single unit cell for absorption located in the bottom panel of the reflex.

The experimental measurement on the cabinet have been performed according to the suggestions expressed in [138, 139]. An exponential sweep has been used to excite the system in a frequency range between 20 - 2000 Hz and a microphone has been used to record the response of the subwoofer in three different locations: in front of the driver to record the direct radiation of the driver, at the opening of the reflex duct to record the contribution of the rear radiation in near-field, and at a distance of 25 cm from the driver to record the overall response of the subwoofer, as already mention in the previous section. The CLIO software has been used to generate the excitation signal and record the system's response.

The results of the measurements are shown in Figure 4.27. The frequency response of the loudspeaker was measured and compared in three different configurations:

- Measurement with the empty cabinet, so no damping material is installed inside the box (Black lines);

- Measurement with the metamaterial panel for absorption installed on the rear panel of the cavity and the metamaterial panel for zero-transmission installed on the lower surface of the reflex (Blue lines);

- Measurement with both metamaterial panels installed within the cabinet and a 1 cm layer of polyester foam inserted into the openings of the resonator of the reflex for zero-transmission (Red lines);

This choice was made because, as shown in Figure 4.27 (blue lines), the resonators in the reflex produced a big absorption at the target frequency $f_{R3}$ but, on the other hand, they generated a new resonance at a slightly lower frequency than $f_{R3}$. This effect is attributed to the fact that the effective volume of the reflex is increased by inserting the resonator cavities, causing the resonance frequency of the open duct to decrease. To overcome this issue, the polyester fiber placed in series with the resonators has the effect of increasing the losses of the resonators, reducing the Q-factor, and broadening the absorption band [140]. In the frequency response, a significant flattening of the frequency response can be observed, noticeable both in the reflex's direct response and in the subwoofer's overall response (Figure 4.27 (red lines)).

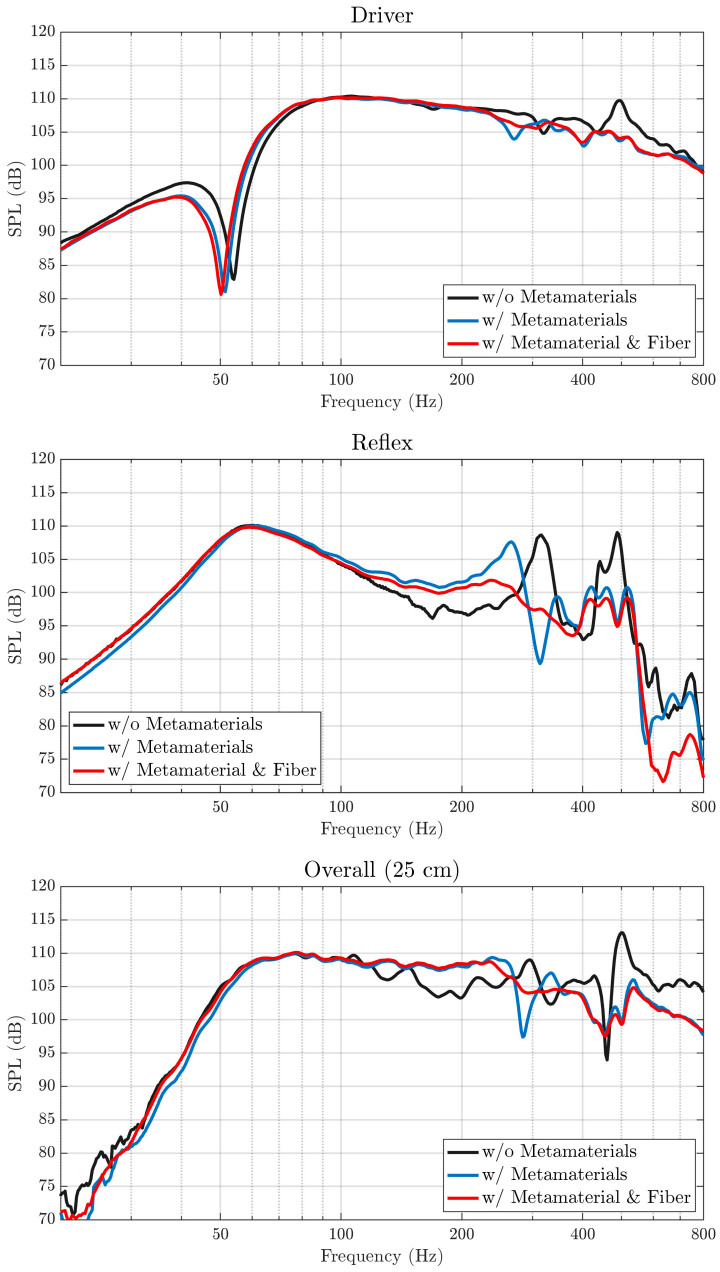


Fig. 4.27 Comparison of the frequency response of the subwoofer in three configurations: without the metamaterial (black lines), with the metamaterial inside the cabinet (blue lines), and with the metamaterial and a 1 cm of polyester fiber (red lines).

Specifically, in the frequency response measured at the reflex opening, a decrease of 10 dB in resonance $f_{R3}$ and a significant reduction in resonances $f_{R1}$ and $f_{R2}$, at least 5 dB and 8dB, respectively, can be noticed. In the total response of the subwoofer at 25 cm, in addition to the reduction of all resonances, it is noticeable that, thanks to the use of metamaterials, the frequency response is higher by at least 3 dB in the frequency range of 100-280 Hz. These reductions can be evaluated better on the near-field measurement of the reflex, focusing on the frequency range where the resonances lie. Figure 4.28 shows the three configurations' measurements compared with the results of the numerical simulations.

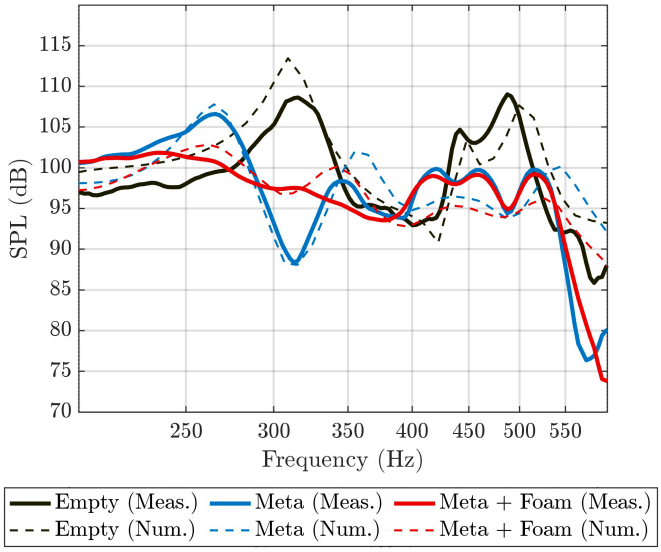


Fig. 4.28 Photographs of the metamaterial panel for the zero transmission. The panel is the array 3x1 of the single unit cell for absorption located in the bottom panel of the reflex.

Moreover, Figure 4.29 visually depicts the time-domain characteristic of the speaker's frequency response, measured at the opening of the reflex. This plot is particularly valuable for analyzing and understanding the decay of the resonances over time. This waterfall plot offers insight into the dynamic behavior of the speaker at the resonances: in the configuration with the metamaterial and fiber, there is a reduction in the resonance decay time of at least 20 ms for the frequency $f_{R3}$ and 14 ms for the two resonances $f_{R1}$ and $f_{R2}$.

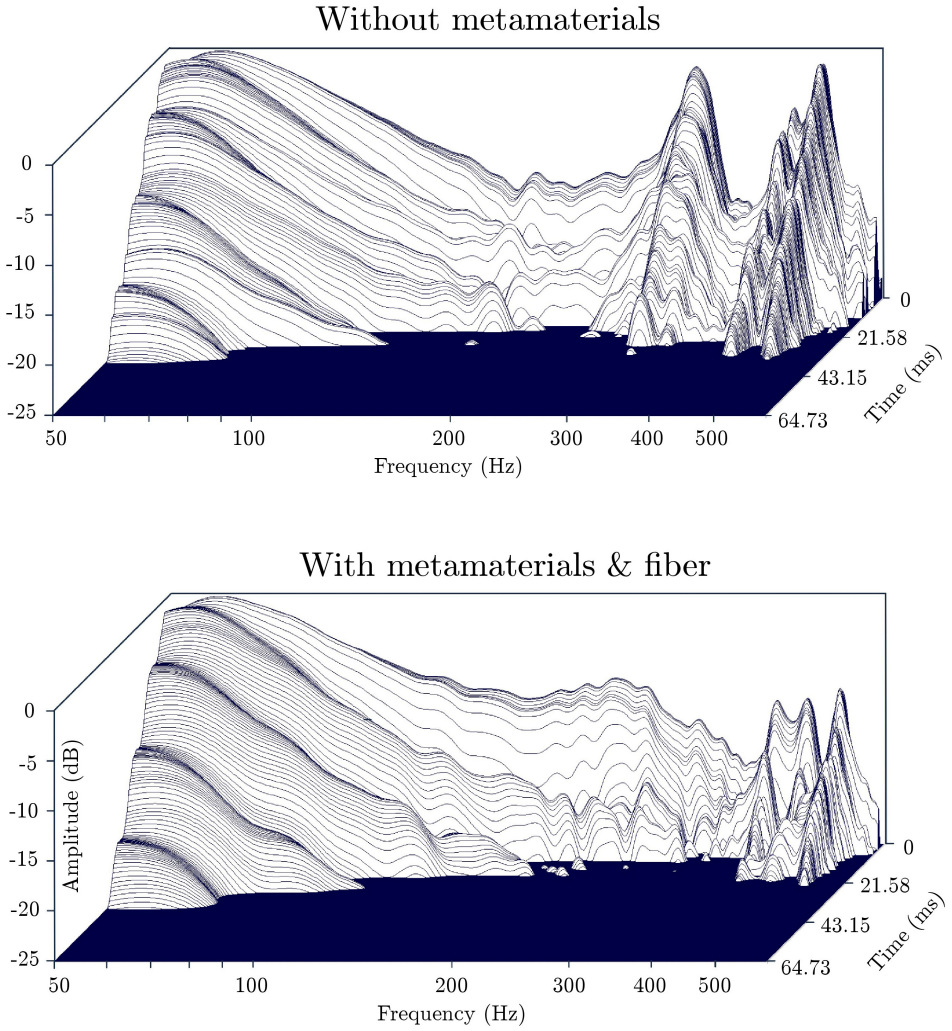


Fig. 4.29 Waterfall visualization of the frequency response of the subwoofer, measured at the opening of the reflex:

### 4.2.8 Discussions

The installation of metamaterials in the subwoofer's enclosure and reflex port contributes significantly to the flattening of the frequency response. Moreover, they also contribute to higher sound pressure levels in the frequency range below the resonance frequency $f_{R3}$. The addition of fiber to the openings of the resonators placed in the reflex port increases the losses of the cavities and decreases the Q-factor of the resonators, helping to broaden and extend the absorption bandwidth of the QWRs [141]. In this way, no new resonance appears in the frequency response at the extremes of the frequency $f_{R3}$, maintaining a flat response across the entire range.

#### Impedance

Further consideration of the insertion of the resonators must be approached from another perspective. It is well-known that the electrical impedance is an important parameter in designing vented-port systems [142]. The cone excursion can be predicted if the impedance of the total system is known. Referring to the acoustical part of the circuit shown in Figure 4.30, the general Thiele-Small model with lumped parameters typically considers losses due to the dissipation inside enclosures and the vented port. Terms such as $R_{AB}$, $R_{AP}$, and $R_{AL}$ are introduced, accounting for

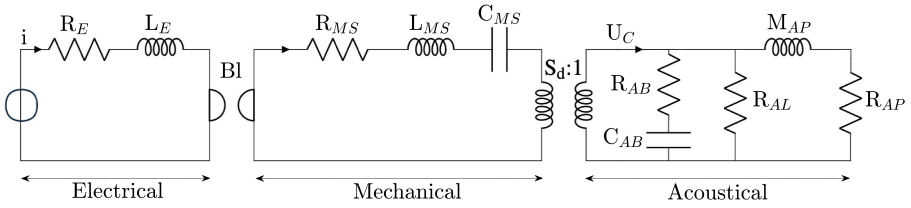


Fig. 4.30 Equivalent Thiele-Small circuit for a vented-port loudspeaker. The cabinet losses are represented in the acoustical part of the circuit as resistive terms: the cavity losses $R_{AB}$, the port losses $R_{AP}$, and the system leakage $R_{AL}$.

losses related to the enclosure, port, and system leakage, respectively. Adding porous material to the enclosure has a dual effect: on one hand, it increases the equivalent volume due to the effective compressibility of the material, and on the other hand, it increases the value of the resistive term $R_{AB}$, effectively increasing the value of flow resistivity. In very low frequencies, when wavelengths are much longer than the enclosure size, reactive effects of the combination of air in the enclosure and the fiber are still present, and the resistive terms can be omitted.[130].

The QWR-based metamaterials developed for the present applications are reactive elements. As shown in Figure 4.31, they can be modeled into the operational mechanism of the loudspeaker as the sum of a resistive term due to the thermal and viscous losses($R_{M\alpha}$, $R_{MT}$ ), and inductance which modeled the acoustic mass of the resonators cavity ($L_{M\alpha}$, $L_{MT}$). QWRs can induce changes not only in the frequency response to mitigate resonances but also, consequently, in the speaker's impedance. The total impedance of the box $Z_{box}$ is the series of the compliance of the air and the

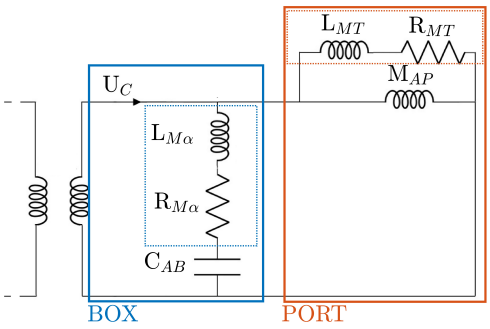


Fig. 4.31 Equivalent Thiele-Small acoustical part, for a vented-port loudspeaker with the metamaterials installed within the enclosure ($R_{M\alpha}$, $L_{M\alpha}$), and within the port ($R_{MT}$, $L_{MT}$).

impedance of the metamaterial:

$$Z_{\text{box}} = R_{M\alpha} + j\omega\left(M_{M\alpha} - \frac{1}{C_{\text{AB}}}\right) \tag{4.5}$$

In the same way, it is possible to define the total impedance of the port $Z_{port,}$ as the parallel combination of the port impedance and the impedance of the inserted metamaterial:

$$Z_{\text{port}} = \frac{(R_{\text{MT}} + j\omega M_{\text{MT}}) \cdot j\omega M_{\text{AP}}}{R_{\text{MT}} + j\omega(M_{\text{MT}} + M_{\text{AP}})} \tag{4.6}$$

Figure4.32 compares the impedance values of the systems with an empty cabinet, a foam-filled cabinet, and a metamaterial cabinet. According to Thiele's notations [124], the lower frequency peak in the impedance curve represents the resonance of the vent $F_l$; the second peak represents the driver's resonance for the air-load mass presented by the enclosure ($F_{sb}$). The minima between these two resonances represent the entire system resonance frequency $F_b$. Simulations showed that the installation of AMMs has a different effect on the foam inside the cabinet. The introduction of metamaterial into the enclosure results in an increase in enclosure

absorption and damping, affecting the $F_{sb}$ peak by reducing its amplitude and shifting the frequency. A similar phenomenon occurs with the insertion of a foam layer, but just on the amplitude of the peak [143]. On the other hand, inserting metamaterial into the port lowers the impedance of the reflex port, as it forms a parallel circuit, leading to a slight increase in the equivalent impedance of the circuit in $F_l$.

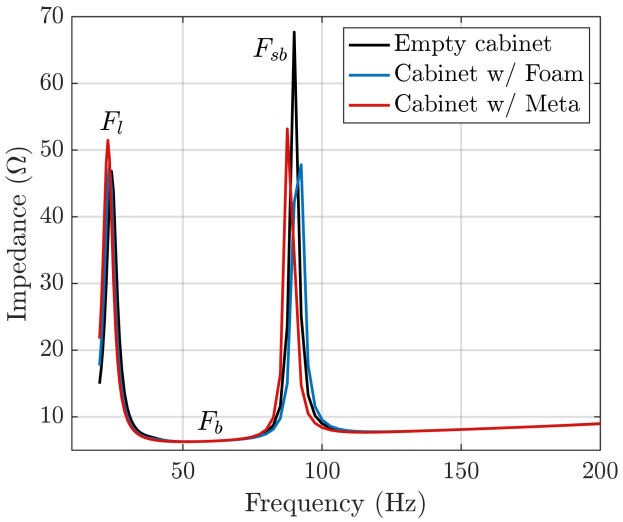


Fig. 4.32 A comparison of numerical values of the impedance of the subwoofer systems, simulated with the normal cabinet and with the metacabinet.

### Voice coil displacement

Considerations can be made regarding the voice coil. As shown in Figure 4.33, the increase in impedance at the frequency $F_l$ contributes to achieving a lower level of displacement of the voice coil with metamaterials. The area where improvement is observed is the critical operating area of the speaker, i.e., below its working frequency. Simulations conducted with metamaterials in the cabinet demonstrate a 10 % reduction in displacement compared to the empty cabinet and even to the foam-filled configuration. Reduced displacement means less strain on the voice coil and the entire driver assembly. Moreover, this decrease in displacement does not lead to a significant reduction in the velocity of the voice coil, which maintains the same value as the configurations with the empty cabinet and with the fiber. This allows for the possibility of keeping transients in line with the measurements of the traditional cabinet. In other words, the installation of metamaterial does not influence the velocity of the voice coil across the entire operating range.

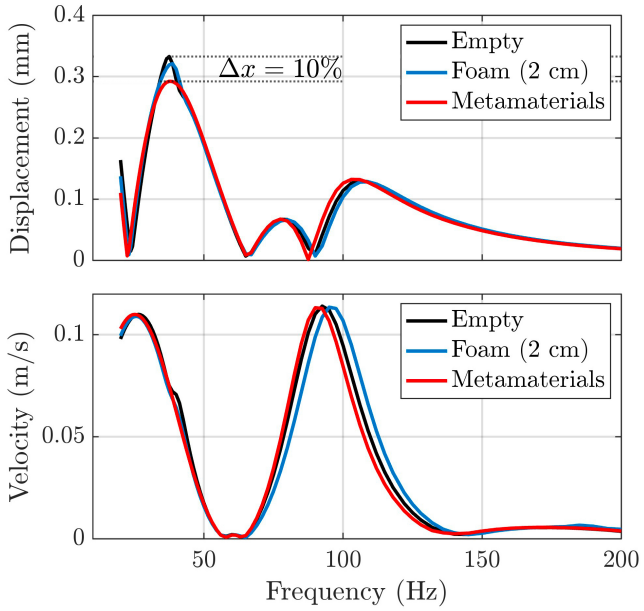


Fig. 4.33 Displacement (Top) and velocity (Bottom) of the voice coil of the driver.

### Efficiency

The last important point to address concerns the loudspeaker's efficiency: it is evident that adding metamaterials inside the cabinet may negatively impact the speaker's efficiency. This is a consequence of lowering the resonance peaks and reducing the system's impedance. Certainly, a more detailed analysis is necessary to quantify the actual change in loudspeaker efficiency because the general efficiency refers to the driver, and no acoustics are involved in the calculation [144]. However, it can be asserted that even a slight reduction in efficiency can still justify the installation of metamaterials compared to porous materials, which would have significantly decreased efficiency and would not have ensured the remarkable reduction in resonances and improvement in emission linearity.

## Summary

The present chapter shows two distinct applications of acoustic metamaterials in speakers and audio systems. The first one is developing a broadband metamaterial to be applied on the back enclosure of a dome tweeter. The back radiation of the tweeter is generally reflected by the enclosure and the reflected portion of sound energy may generate interferences with the direct radiation of the speaker. A metamaterial

made by 14 distinct QWRs has been developed to assure broadband absorption in the frequency range between 700 and 2000 Hz. The frequency response of the tweeter with the metamaterial showed a reduction of resonances, contributing to an increase in the linearity of the tweeter emission. Specifically, there is a reduction in sound pressure level below 800 Hz, accompanied by a simultaneous increase of at least 4 dB around 1300 Hz. Furthermore, a general flattening of the frequency response has been achieved with the metamaterial in the enclosure, demonstrating how the QWR-based metamaterial acts more significantly than polyester fiber, commonly used for such applications. The positive results are also the result of a compromise between the available space to engineer the metamaterial, i.e., the existing enclosure, and the required absorption properties.

The second application involves the development of a metamaterial for a reflex-ported subwoofer. In particular, the goal was to remove or at least reduce the resonances generated by the standing waves resulting from the shapes of the subwoofer cabinet. These resonances contribute to deteriorating the frequency response of the subwoofer and are generally independent of the speaker's emission range. A detailed study of the origin of these resonances was conducted to design two different metamaterials: one for absorbing two resonances generated in the subwoofer's cavity and another for zero-transmission of resonance in the reflex port. An analytical, numerical, and prototyping approach was pursued, allowing for the creation of elementary unit cells characterized in the impedance tube. Ultimately, panels of metamaterials formed by these unit cells were installed in the subwoofer, and the frequency response was measured and compared with that of the classical subwoofer. A clear reduction in both resonances was achieved, with an 8-10 dB reduction for frequencies generated in the cabinet cavity and a 10 dB improvement in the resonance frequency due to the reflex port. This improvement was aided by adding porous material to the openings of the resonators, contributing to increased losses in the resonant cavities. The enhancements are evident in near-field measurements conducted at the opening of the reflex port, and more broadly, improvements are noticeable in the overall subwoofer response, measured at a distance of 25 cm from the driver. While these results are significant for the case study, they also serve as an important benchmark for applying the method to all loudspeaker models equipped with a reflex port.

# Conclusions

Control of noise has become a central and challenging topic of interest. The study of innovative materials for noise control has been evolving for decades, with the advent of acoustic metamaterials providing an attractive and alternative solution to traditional absorbent materials, which show significant limitations in various contexts. This thesis proposed the investigation of a robust method for the development of acoustic metamaterials based on resonant elements, aiming to find practical applications in two distinct fields: as sound-absorbing material for noise control in hospital environments and as an absorptive material in speakers and audio systems. The common thread lies in the goal of controlling desired noise or eliminating unwanted noise.

The thesis started with an overview of fundamental topics to provide a framework for the entire work. Specifically, a general description of the fundamental physics equations of waves in fluids has been provided. This was followed by a review of the concept of acoustic absorption and traditional materials used for this purpose, introducing fundamental concepts for understanding their mechanisms and limitations. An introduction to acoustic metamaterials was presented, highlighting the differences, possible alternative solutions, and advantages over traditional materials. Special attention has been given to a particular class of metamaterials at the core of this work, namely resonator-based metamaterials. The two types of resonators focused on in this work were the Quarter Wavelength Resonator (QWR) and the Helmholtz Resonator (HR). The mechanisms for sound absorption and wave control have been explained for both, providing general definitions for their understanding.

The Transfer Matrix Method (TMM) has been introduced as a necessary analytical tool for understanding acoustic problems. The TMM simplified the treatment of sound wave propagation to one-dimensional cases by assuming the propagation of plane waves. This tool has been used in this thesis to address reflection problems when a sound wave hits a surface and transmission problems, i.e., when a material is

surrounded by a fluid on both sides, simplifying the description of incident, reflected, and transmitted waves in various contexts. The focus then shifted to the use of TMM in ducts, waveguides, and cavities, which is particularly relevant for applications of acoustic resonators.

The method for the development and design of metamaterials has been introduced, starting with the study of analytical models of QWR and HR and parallel resonant systems for broadband absorption. Matlab has been used to develop predictive models of resonators as a starting point for fixed target absorption frequencies required by various contexts. Simultaneously, COMSOL Multiphysics has been employed for numerical characterization. Finite Element Method (FEM) numerical models were developed to optimize shapes, geometries, and dimensions of resonators, introducing challenges from real cases not considered by analytical models.

Simulations of waveguides were developed for both absorption and transmission cases, assuming plane wave propagation to characterize metamaterials. A significant part of this work dealt with prototyping acoustic metamaterial samples. The goal was to study various 3D printing methods, printing settings, and materials to recreate prototypes with acoustic properties predicted by analytical and numerical models. Two methods, Fuse Deposition Modeling and Stereolithography, were considered for this study, analyzing their advantages, disadvantages, and the best printing setups from the perspectives of prototyping simplicity, cost, and sustainability. Additionally, an analysis of the effects of temperature on various 3D-printed samples has been conducted to evaluate the impact of temperature changes on the acoustic properties of the prototypes.

The characterization of real samples was done using the impedance tube, allowing the calculation of absorption, reflection, and, if necessary, transmission coefficients under ideal conditions, assuming normal incidence of plane waves. Calibration between analytical models, numerical models, and experimental tube measurements was performed to characterize metamaterials' design and physical realization.

The thesis then transitioned to the applications, where the method has been applied to develop metamaterial absorbers using QWR and HR. The first application, which was related to the hospital environment, was introduced. Initially, noise characterization in such environments was conducted through sound level monitoring, an experimental reverberation time campaign, and clustering analysis to separate sources to quantify the contributions of various sources of different natures. The intervention target was defined within the frequency range of 400 and 1000 Hz, aim-

ing to reduce the absorption time in the typical speech frequency range, enhancing intelligibility and facilitating communication. A multi-resonant metamaterial for broadband absorption consisting of twenty Helmholtz resonators was developed analytically, numerically, 3D printed, and measured in the impedance tube. The results of experimental measurements have been used as input to develop a further FDTD/GA hybrid numerical model of the treated hospital environment. The metamaterial was introduced into the model as a ceiling to reduce the reverberation time inside the hospital room.

The post-treatment results showed a 30 % reduction in reverberation time within the considered range compared to pre-treatment values. A greater reduction could be expected to fulfill room acoustics recommendations in hospitals. Still, the study has demonstrated that metamaterials may be a valid solution compared to traditional materials, which are challenging to install in critical environments such as healthcare facilities. The final part of the thesis addressed two different applications of acoustic metamaterials in speakers and audio systems. In the first application, a broadband metamaterial was developed and designed to absorb the rearward radiation of a high-frequency transducer tweeter. The rearward radiation produces reflections on the tweeter's enclosure, causing destructive and constructive interferences with the forward radiation, disrupting the device's linearity. The metamaterial, consisting of fourteen QWRs in parallel, allowed significant absorption of the rearward radiation, limiting reflections and improving the tweeter's frequency response. In particular, around the tweeter cutoff frequency, the metamaterial reduces enclosure reflections that cause destructive interference, increasing the SPL of the frequency response by around 4 dB. The second application was in a subwoofer with a vented port. The subwoofer exhibits several resonances resulting from standing waves generated due to volumes inside the cabinet, visible in the frequency response. The resonances have been investigated, and two different metamaterials have been developed. The first metamaterial has been designed to absorb two resonances generated inside the cabinet's internal cavity and the second to reduce the resonance generated by the reflex port. The resonances have been attenuated by values ranging from 5 to 10 dB, improving the subwoofer's frequency response and confirming how metamaterials can be a more effective solution than the traditional approaches currently adopted in electroacoustics.

In general, the applications in such different contexts have allowed the assessment of the developed method in different situations and for different purposes. The

method has proven to be robust and reliable in all applications and can be used in other contexts where the application of metamaterials is possible.

## Outlook and future work

At the end of the present dissertation, several topics are still debated and need further investigation. Indeed, despite the method appearing robust, and the applications of metamaterials in various contexts yielding positive results, there is still a need for a more in-depth analysis of more convenient manufacturing techniques than 3D printing. While 3D printing remains an essential tool for prototyping, it is not cost-effective for structures of considerable size and a large number of components. This study has not addressed the physical realization of metamaterials from the industrialization perspective, either in terms of production time or in terms of costs. On the other hand, it has confirmed the significant advantages of acoustic metamaterials over traditional materials, both in terms of performance and in the broad range of usable materials. This latter aspect is of central importance when factors such as hygiene, sustainability, low maintenance costs, cleanliness, and low susceptibility to deterioration are of interest. Whether for treating critical spaces like hospitals or improving audio systems, metamaterials have proven to be a robust technological solution. However, further studies will be needed to optimize development, large-scale production processes, and applications.

# References


[1] Frank J Fahy. *Foundations of engineering acoustics*. Elsevier, 2000.

[2] Francesco Aletta and Jian Kang. Promoting healthy and supportive acoustic environments: Going beyond the quietness, 2019.

[3] Mathias Basner, Wolfgang Babisch, Adrian Davis, Mark Brink, Charlotte Clark, Sabine Janssen, and Stephen Stansfeld. Auditory and non-auditory effects of noise on health. *The lancet*, 383(9925):1325–1332, 2014.

[4] Stephen Stansfeld, Mary Haines, and Bernadette Brown. Noise and health in the urban environment. *Reviews on environmental health*, 15(1-2):43–82, 2000.

[5] Peter Lercher, Dick Botteldooren, Ulrich Widmann, Ulrich Uhrner, and Ewald Kammeringer. Cardiovascular effects of environmental noise: Research in austria. *Noise & health*, 13(52):234–250, 2011.

[6] Erica E Ryherd, Selen Okcu, Jeremy Ackerman, Craig Zimring, and Kerstin Persson Waye. Noise pollution in hospitals: impacts on staff. *Journal of Clinical Outcomes Management*, 19(11):491–500, 2012.

[7] Anthony J Oleksy and Joseph J Schlesinger. What's all that noise—improving the hospital soundscape. *Journal of clinical monitoring and computing*, 33(4):557–562, 2019.

[8] Leitao Cao, Qiuxia Fu, Yang Si, Bin Ding, and Jianyong Yu. Porous materials for sound absorption. *Composites Communications*, 10:25–35, 2018.

[9] Xiaoning Tang and Xiong Yan. Acoustic energy absorption properties of fibrous materials: A review. *Composites Part A: Applied Science and Manufacturing*, 101:360–380, 2017.

[10] Jorge P Arenas and Kimihiro Sakagami. Sustainable acoustic materials, 2020.

[11] Mai-Britt Beldam and Erling Nilsson. Acoustic model for evaluation of hospital rooms with absorbent ceilings.

[12] Viggo Tarnow. Airflow resistivity of models of fibrous acoustic materials. *The Journal of the Acoustical Society of America*, 100(6):3706–3713, 1996.

[13] Yvan Champoux and Jean-F Allard. Dynamic tortuosity and bulk modulus in air-saturated porous media. *Journal of applied physics*, 70(4):1975–1979, 1991.

[14] Michael E Delany and EN Bazley. Acoustical properties of fibrous absorbent materials. *Applied acoustics*, 3(2):105–116, 1970.

[15] Jean-F Allard and Yvan Champoux. New empirical equations for sound propagation in rigid frame fibrous materials. *The Journal of the Acoustical Society of America*, 91(6):3346–3353, 1992.

[16] Massimo Garai and Francesco Pompoli. A simple empirical model of polyester fibre materials for acoustical applications. *Applied Acoustics*, 66(12):1383–1398, 2005.

[17] Olga Umnova, David Tsiklauri, and Rodolfo Venegas. Effect of boundary slip on the acoustical properties of microfibrous materials. *The Journal of the Acoustical Society of America*, 126(4):1850–1861, 2009.

[18] N Voronina. Acoustic properties of fibrous materials. *Applied Acoustics*, 42(2):165–174, 1994.

[19] R Dunne, D Desai, and R Sadiku. A review of the factors that influence sound absorption and the available empirical models for fibrous materials. *Acoustics Australia*, 45:453–469, 2017.

[20] Farzad Zangeneh-Nejad and Romain Fleury. Active times for acoustic metamaterials. *Reviews in Physics*, 4:100031, 2019.

[21] Guancong Ma and Ping Sheng. Acoustic metamaterials: From local resonances to broad horizons. *Science advances*, 2(2):e1501595, 2016.

[22] Michael R Haberman and Matthew D Guild. Acoustic metamaterials. *Physics Today*, 69(6):42–48, 2016.

[23] Muamer Kadic, Graeme W Milton, Martin van Hecke, and Martin Wegener. 3d metamaterials. *Nature Reviews Physics*, 1(3):198–210, 2019.

[24] Steven A Cummer, Johan Christensen, and Andrea Alù. Controlling sound with acoustic metamaterials. *Nature Reviews Materials*, 1(3):1–13, 2016.

[25] Arpan Gupta. A review on sonic crystal, its applications and numerical analysis techniques. *Acoustical Physics*, 60:223–234, 2014.

[26] Richard V Craster and Sébastien Guenneau. *Acoustic metamaterials: negative refraction, imaging, lensing and cloaking*, volume 166. Springer Science & Business Media, 2012.

[27] Uno Ingard. On the theory and design of acoustic resonators. *The Journal of the Acoustical Society of America*, 25(6):1037–1061, 1953.

[28] Vicente Romero-Garcia and Anne-Christine Hladky-Hennion. *Fundamentals and applications of acoustic metamaterials: from seismic to radio frequency*. John Wiley & Sons, 2019.

[29] Changru Chen, Zhibo Du, Gengkai Hu, and Jun Yang. A low-frequency sound absorbing material with subwavelength thickness. *Applied Physics Letters*, 110(22), 2017.

[30] Xiaobing Cai, Qiuquan Guo, Gengkai Hu, and Jun Yang. Ultrathin low-frequency sound absorbing panels based on coplanar spiral tubes or coplanar helmholtz resonators. *Applied Physics Letters*, 105(12), 2014.

[31] Vicente Romero-García, Georgios Theocharis, Olivier Richoux, and V Pagneux. Use of complex frequency plane to design broadband and subwavelength absorbers. *The Journal of the Acoustical Society of America*, 139(6):3395–3403, 2016.

[32] Matteo Cingolani, Gioia Fusaro, Giulia Fratoni, and Massimo Garai. Influence of thermal deformations on sound absorption of three-dimensional printed metamaterials. *The Journal of the Acoustical Society of America*, 151(6):3770–3779, 2022.

[33] Matteo Cingolani, Gioia Fusaro, and Massimo Garai. The influence of thermo-hygrometric conditions on metamaterials' acoustic performance: an investigation on a 3d printed coiled-up resonator. In *INTER-NOISE and NOISE-CON Congress and Conference Proceedings*, volume 265, pages 3045–3050. Institute of Noise Control Engineering, 2023.

[34] Jean Boulvert, Gwénaël Gabard, Vicente Romero-García, and Jean-Philippe Groby. Compact resonant systems for perfect and broadband sound absorption in wide waveguides in transmission problems. *Scientific Reports*, 12(1):10013, 2022.

[35] Paola Gori, Claudia Guattari, Francesco Asdrubali, Roberto de Lieto Vollaro, Alessio Monti, Davide Ramaccia, Filiberto Bilotti, and Alessandro Toscano. Sustainable acoustic metasurfaces for sound control. *Sustainability*, 8(2):107, 2016.

[36] Nansha Gao, Zhicheng Zhang, Jie Deng, Xinyu Guo, Baozhu Cheng, and Hong Hou. Acoustic metamaterials for noise reduction: a review. *Advanced Materials Technologies*, 7(6):2100698, 2022.

[37] Guangxin Liao, Congcong Luan, Zhenwei Wang, Jiapeng Liu, Xinhua Yao, and Jianzhong Fu. Acoustic metamaterials: A review of theories, structures, fabrication approaches, and applications. *Advanced Materials Technologies*, 6(5):2000787, 2021.

[38] Min Yang and Ping Sheng. Acoustic metamaterial absorbers: The path to commercialization. *Applied Physics Letters*, 122(26), 2023.

[39] Matteo Cingolani, Giulia Fratoni, Luca Barbaresi, Dario D'orazio, Brian Hamilton, and Massimo Garai. A trial acoustic improvement in a lecture hall with mpp sound absorbers and fdtd acoustic simulations. *Applied Sciences*, 11(6):2445, 2021.

[40] Sanjay Kumar and Heow Pueh Lee. The present and future role of acoustic metamaterials for architectural and urban noise mitigations. In *Acoustics*, volume 1, pages 590–607. MDPI, 2019.

[41] Arun Arjunan, Ahmad Baroutaji, John Robinson, Aaron Vance, and Abul Arafat. Acoustic metamaterials for sound absorption and insulation in buildings. *Building and Environment*, page 111250, 2024.

[42] Sebastien Degraeve and Jack Oclee-Brown. Metamaterial absorber for loudspeaker enclosures. In *Audio Engineering Society Convention 148*. Audio Engineering Society, 2020.

[43] Cecilia Casarini, James FC Windmill, and Joseph C Jackson. 3d printed small-scale acoustic metamaterials based on helmholtz resonators with tuned overtones. In *2017 IEEE SENSORS*, pages 1–3. IEEE, 2017.

[44] Letizia Chisari, Mario Di Cola, and Paolo Martignon. Acoustic metamaterials in loudspeaker systems design. In *Audio Engineering Society Convention 147*. Audio Engineering Society, 2019.

[45] Michael Barron. *Auditorium acoustics and architectural design*. Routledge, 2009.

[46] Lawrence E Kinsler, Austin R Frey, Alan B Coppens, and James V Sanders. *Fundamentals of acoustics*. John wiley & sons, 2000.

[47] Philip McCord Morse and K Uno Ingard. *Theoretical acoustics*. Princeton university press, 1986.

[48] Philip M Morse and K Uno Ingard. Theoretical acoustics mcgraw-hill. *New York*, 4, 1968.

[49] Harry Ferdinand Olson. Elements of acoustical engineering. 1940.

[50] Keith Attenborough. Acoustical characteristics of porous materials. *Physics Reports*, 82(3):179–227, 1982.

[51] Jorge P Arenas and Malcolm J Crocker. Recent trends in porous sound-absorbing materials. *Sound & vibration*, 44(7):12–18, 2010.

[52] Jean-Philippe Groby, Noé Jiménez, and Vicent Romero-García. Acoustic metamaterial absorbers. *Acoustic Waves in Periodic Structures, Metamaterials, and Porous Media: From Fundamentals to Industrial Applications*, pages 167–204, 2021.

[53] Min Yang and Ping Sheng. Sound absorption structures: From porous media to acoustic metamaterials. *Annual Review of Materials Research*, 47:83–114, 2017.

[54] David Linton Johnson, Joel Koplik, and Roger Dashen. Theory of dynamic permeability and tortuosity in fluid-saturated porous media. *Journal of fluid mechanics*, 176:379–402, 1987.

[55] J-F Allard and Gilles Daigle. Propagation of sound in porous media: Modeling sound absorbing materials, 1994.

[56] Maurice A Biot. Theory of propagation of elastic waves in a fluid-saturated porous solid. ii. higher frequency range. *The Journal of the acoustical Society of america*, 28(2):179–191, 1956.

[57] Rakhesh S Kshetrimayum. A brief intro to metamaterials. *IEEE potentials*, 23(5):44–46, 2004.

[58] Ari Sihvola. Metamaterials in electromagnetics. *Metamaterials*, 1(1):2–11, 2007.

[59] Jensen Li and Che Ting Chan. Double-negative acoustic metamaterial. *Physical Review E*, 70(5):055602, 2004.

[60] Hui-Jie Shen, Ji-Hong Wen, Dian-Long Yu, Li Cai, and Xi-Sen Wen. Research on a cylindrical cloak with active acoustic metamaterial layers. 2012.

[61] Jiajun Zhao, Baowen Li, Zhining Chen, and Cheng-Wei Qiu. Manipulating acoustic wavefront by inhomogeneous impedance and steerable extraordinary reflection. *Scientific reports*, 3(1):2537, 2013.

[62] Shu Zhang, Chunguang Xia, and Nicholas Fang. Broadband acoustic cloak for ultrasound waves. *Physical review letters*, 106(2):024301, 2011.

[63] Jerome O Vasseur, Pierre A Deymier, B Chenni, B Djafari-Rouhani, L Dobrzynski, and D Prevost. Experimental and theoretical evidence for the existence of absolute acoustic band gaps in two-dimensional solid phononic crystals. *Physical Review Letters*, 86(14):3012, 2001.

[64] Hongwei Sun, Fei Yan, Hao Gu, and Ying Li. Acoustic metamaterial with negative parameter. In *Nondestructive Characterization for Composite Materials, Aerospace Engineering, Civil Infrastructure, and Homeland Security 2014*, volume 9063, pages 517–522. SPIE, 2014.

[65] Sam Hyeon Lee, Choon Mahn Park, Yong Mun Seo, Zhi Guo Wang, and Chul Koo Kim. Acoustic metamaterial with negative density. *Physics letters A*, 373(48):4464–4469, 2009.

[66] Sam Hyeon Lee, Choon Mahn Park, Yong Mun Seo, Zhi Guo Wang, and Chul Koo Kim. Acoustic metamaterial with negative modulus. *Journal of Physics: Condensed Matter*, 21(17):175704, 2009.

[67] Marc Dubois, Chengzhi Shi, Xuefeng Zhu, Yuan Wang, and Xiang Zhang. Observation of acoustic dirac-like cone and double zero refractive index. *Nature communications*, 8(1):14871, 2017.

[68] Leo Leroy Beranek and Tim Mellow. *Acoustics: sound fields and transducers*. Academic Press, 2012.

[69] Noé Jiménez, Jean-Philippe Groby, and Vicent Romero-García. The transfer matrix method in acoustics: Modelling one-dimensional acoustic systems, phononic crystals and acoustic metamaterials. *Acoustic Waves in Periodic Structures, Metamaterials, and Porous Media: From Fundamentals to Industrial Applications*, pages 103–164, 2021.

[70] Michael R Stinson. The propagation of plane sound waves in narrow and wide circular tubes, and generalization to uniform tubes of arbitrary cross-sectional shape. *The Journal of the Acoustical Society of America*, 89(2):550–558, 1991.

[71] Jean Kergomard and A Garcia. Simple discontinuities in acoustic waveguides at low frequencies: critical analysis and formulae. *Journal of Sound and Vibration*, 114(3):465–479, 1987.

[72] Hyeonbin Ryoo and Wonju Jeon. Broadband sound absorption using multiple hybrid resonances of acoustic metasurfaces. *International Journal of Mechanical Sciences*, 229:107508, 2022.

[73] Min Yang, Shuyu Chen, Caixing Fu, and Ping Sheng. Optimal sound-absorbing structures. *Materials Horizons*, 4(4):673–680, 2017.

[74] *COMSOL Multiphysics® v. 6.1. COMSOL AB, Stockholm, Sweden.* www.comsol.com.

[75] Wim Ronald Kampinga. Viscothermal acoustics using finite elements-analysis tools for engineers. 2010.

[76] H Tijdeman. On the propagation of sound waves in cylindrical tubes. *Journal of Sound and Vibration*, 39(1):1–33, 1975.

[77] Meisam Askari, David A Hutchins, Peter J Thomas, Lorenzo Astolfi, Richard L Watson, Meisam Abdi, Marco Ricci, Stefano Laureti, Luzhen Nie, Steven Freear, et al. Additive manufacturing of metamaterials: A review. *Additive Manufacturing*, 36:101562, 2020.

[78] Omar A Mohamed, Syed H Masood, and Jahar L Bhowmik. Optimization of fused deposition modeling process parameters: a review of current research and future prospects. *Advances in manufacturing*, 3:42–53, 2015.

[79] Gioia Fusaro, Luca Barbaresi, Matteo Cingolani, Massimo Garai, Edoardo Ida, Andrea Prato, and Alessandro Schiavi. Investigation of the impact of additive manufacturing techniques on the acoustic performance of a coiled-up

resonator. *The Journal of the Acoustical Society of America*, 153(5):2921, may 2023.

[80] Syed H Masood. Intelligent rapid prototyping with fused deposition modelling. *Rapid Prototyping Journal*, 2(1):24–33, 1996.

[81] Alberto Boschetto and Luana Bottini. Accuracy prediction in fused deposition modeling. *The international journal of advanced manufacturing technology*, 73:913–928, 2014.

[82] Jigang Huang, Qin Qin, and Jie Wang. A review of stereolithography: Processes and systems. *Processes*, 8(9):1138, 2020.

[83] Nicholas Rodriguez, Samantha Ruelas, Jean-Baptiste Forien, Nikola Dudukovic, Josh DeOtte, Jennifer Rodriguez, Bryan Moran, James P Lewicki, Eric B Duoss, and James S Oakdale. 3d printing of high viscosity reinforced silicone elastomers. *Polymers*, 13(14):2239, 2021.

[84] Ferry PW Melchels, Jan Feijen, and Dirk W Grijpma. A review on stereolithography and its applications in biomedical engineering. *Biomaterials*, 31(24):6121–6130, 2010.

[85] Stefan Dzionk. Surface structure of components created by stereolitography. *Solid State Phenomena*, 199:338–343, 2013.

[86] R Bernasconi, C Credi, M Tironi, M Levi, and L Magagnin. Electroless metallization of stereolithographic photocurable resins for 3d printing of functional microdevices. *Journal of The Electrochemical Society*, 164(5):B3059, 2017.

[87] ISO 10534-2:1998. *Acoustics Determination of sound absorption coefficient and impedance in impedance tubes.*, 1998.

[88] The Mathworks Inc. *MATLAB version: 23.2.0 (R2023b)*. Natick, Massachussets, United States, the mathworks inc. edition, 2023.

[89] JY Chung and DA Blaser. Transfer function method of measuring acoustic intensity in a duct system with flow. *The Journal of the Acoustical Society of America*, 68(6):1570–1577, 1980.

[90] Bryan H Song and J Stuart Bolton. A transfer-matrix approach for estimating the characteristic impedance and wave numbers of limp and rigid porous materials. *The Journal of the Acoustical Society of America*, 107(3):1131–1152, 2000.

[91] Yuanwei Yao, Fugen Wu, Xin Zhang, and Zhilin Hou. Thermal tuning of lamb wave band structure in a two-dimensional phononic crystal plate. *Journal of Applied Physics*, 110(12), 2011.

[92] Baizhan Xia, Ning Chen, Longxiang Xie, Yuan Qin, and Dejie Yu. Temperature-controlled tunable acoustic metamaterial with active band gap and negative bulk modulus. *Applied Acoustics*, 112:1–9, 2016.

[93] RF Clash Jr and LM Rynkiewicz. Thermal expansion properties of plastic materials. *Industrial & Engineering Chemistry*, 36(3):279–282, 1944.

[94] Matteo Cingolani, Domenico De Salvio, Dario D'Orazio, and Massimo Garai. Clustering analysis of noise sources in healthcare facilities. *Applied Acoustics*, 214:109660, 2023.

[95] Birgitta Berglund, Thomas Lindvall, Dietrich H Schwela, World Health Organization, et al. *Guidelines for community noise*, 1999.

[96] Ilene J Busch-Vishniac, James E West, Colin Barnhill, Tyrone Hunter, Douglas Orellana, and Ram Chivukula. Noise levels in johns hopkins hospital. *The Journal of the Acoustical Society of America*, 118(6):3629–3645, 2005.

[97] Douglas Orellana, Ilene J Busch-Vishniac, and James E West. Noise in the adult emergency department of johns hopkins hospital. *The Journal of the Acoustical Society of America*, 121(4):1996–1999, 2007.

[98] Julie L Darbyshire and J Duncan Young. An investigation of sound levels on intensive care units with reference to the who guidelines. *Critical Care*, 17:1–8, 2013.

[99] ISO 3382-1 (2009). *Acoustics - Measurement of room acoustic parameters. Part 2: Part 2: Reverberation time in ordinary rooms.*, 2009.

[100] Domenico De Salvio and Dario D'Orazio. Effectiveness of acoustic treatments and pa redesign by means of student activity and speech levels. *Applied Acoustics*, 194:108783, 2022.

[101] Domenico De Salvio, Dario D'Orazio, and Massimo Garai. Unsupervised analysis of background noise sources in active offices. *The Journal of the Acoustical Society of America*, 149(6):4049–4060, 2021.

[102] Paul Kendrick, Nicola Shiers, Robert Conetta, Trevor J Cox, Bridget M Shield, and Charlie Mydlarz. Blind estimation of reverberation time in classrooms and hospital wards. *Applied acoustics*, 73(8):770–780, 2012.

[103] Domenico De Salvio, Michael J Bianco, Peter Gerstoft, Dario D'Orazio, and Massimo Garai. Blind source separation by long-term monitoring: A variational autoencoder to validate the clustering analysis. *The Journal of the Acoustical Society of America*, 153(1):738–750, 2023.

[104] Arthur P Dempster, Nan M Laird, and Donald B Rubin. Maximum likelihood from incomplete data via the em algorithm. *Journal of the royal statistical society: series B (methodological)*, 39(1):1–22, 1977.

[105] Scott McLachlan, Kudakwashe Dube, Graham A Hitman, Norman E Fenton, and Evangelia Kyrimi. Bayesian networks in healthcare: Distribution by medical condition. *Artificial intelligence in medicine*, 107:101912, 2020.

[106] Pasquale Bottalico and Arianna Astolfi. Investigations into vocal doses and parameters pertaining to primary school teachers in classrooms. *The Journal of the Acoustical Society of America*, 131(4):2817–2827, 2012.

[107] P Leonard and A Chilton. The lombard effect in open plan offices. *Proceedings of the Institute of Acoustics, Milton Keynes, United Kingdom*, 2019.

[108] Wayne O Olsen. Average speech levels and spectra in various speaking/listening conditions. ., 1998.

[109] Munhum Park, Armin Kohlrausch, Werner de Bruijn, Peter de Jager, and Koen Simons. Analysis of the soundscape in an intensive care unit based on the annotation of an audio recording. *The Journal of the Acoustical Society of America*, 135(4):1875–1886, 2014.

[110] ISO 3382-3 (2012). *Acoustics - Measurement of Room Acoustic Parameters. Part 3: Open plan offices*, 2012.

[111] Glenn Leembruggen, J Verhave, S Feistel, L Holtzem, P Mapp, H Sato, T Steinbrecher, and S Van Wijngaarden. The effect on sti results of changes to the male test-signal spectrum. *Proc. IOA*, 38:78–87, 2016.

[112] Finnur Pind, Cheol-Ho Jeong, Allan P Engsig-Karup, Jan S Hesthaven, and Jakob Strømann-Andersen. Time-domain room acoustic simulations with extended-reacting porous absorbers using the discontinuous galerkin method. *The Journal of the Acoustical Society of America*, 148(5):2851–2863, 2020.

[113] Takeshi Okuzono, Takumi Yoshida, and Kimihiro Sakagami. Efficiency of room acoustic simulations with time-domain fem including frequency-dependent absorbing boundary conditions: Comparison with frequency-domain fem. *Applied Acoustics*, 182:108212, 2021.

[114] Tobias Thydal, Finnur Pind, Cheol-Ho Jeong, and Allan P Engsig-Karup. Experimental validation and uncertainty quantification in wave-based computational room acoustics. *Applied Acoustics*, 178:107939, 2021.

[115] Giulia Fratoni, Brian Hamilton, and Dario D'Orazio. Feasibility of a finite-difference time-domain model in large-scale acoustic simulations. *The Journal of the Acoustical Society of America*, 152(1):330–341, 2022.

[116] Trevor Cox and Peter d'Antonio. *Acoustic absorbers and diffusers: theory, design and application*. CRC press, 2016.

[117] Michael Vorländer and Eckard Mommertz. Definition and measurement of random-incidence scattering coefficients. *Applied acoustics*, 60(2):187–199, 2000.

[118] Boris Mondet, Jonas Brunskog, Cheol-Ho Jeong, and Jens Holger Rindel. From absorption to impedance: Enhancing boundary conditions in room acoustic simulations. *Applied Acoustics*, 157:106884, 2020.

[119] Martin Colloms. *High performance loudspeakers: optimising high fidelity loudspeaker systems*. John Wiley & Sons, 2018.

[120] Doug Button, Russ Lambert, Pascal Brunet, and James Bunning. Characterization of nonlinear port parameters in loudspeaker modeling. In *Audio Engineering Society Convention 145*. Audio Engineering Society, 2018.

[121] Letizia Chisari, Mario Di Cola, Paolo Martignon, and Gianluca Memoli. Preliminary studies for metamaterial-based audio systems. In *Proceedings of Euronoise*, 2021.

[122] Jie Huang, Xing Tian, Xuelei Feng, and Yong Shen. Tuning the nonlinear acoustic damping of helmholtz resonators used in loudspeaker systems. *Journal of the Audio Engineering Society*, 70(7/8):634–641, 2022.

[123] Massimiliano Rossi, Enrico Esposito, and Enrico Primo Tomasini. Piv application to fluid dynamics of bass reflex ports. *Particle Image Velocimetry: New Developments and Recent Applications*, pages 259–270, 2008.

[124] Neville Thiele. Loudspeakers in vented boxes: Part 1. *Journal of the Audio Engineering Society*, 19(5):382–392, 1971.

[125] Richard H Small. Vented-box loudspeaker systems–part 1: Small-signal analysis. *Journal of the Audio Engineering Society*, 21(5):363–372, 1973.

[126] WP Putrie, S Indrawati, G Prajitno, et al. The vented-box effect on thiele-small parameter loudspeaker. In *Journal of Physics: Conference Series*, volume 1825, page 012002. IOP Publishing, 2021.

[127] Juha Backman. The nonlinear behavior of reflex ports. In *Audio Engineering Society Convention 98*. Audio Engineering Society, 1995.

[128] Jaakko Nisula, Juha Holm, and Aki Mäkivirta. Calculating sound radiation from loudspeaker enclosures using the finite element analysis. In *Audio Engineering Society Conference: 51st International Conference: Loudspeakers and Headphones*. Audio Engineering Society, 2013.

[129] Yves Pene, Yoachim Horyn, and Christophe Combet. Non-linear acoustic losses prediction in vented loudspeaker using computational fluid dynamic simulation. In *Audio Engineering Society Convention 148*. Audio Engineering Society, 2020.

[130] LJS Bradbury. The use of fibrous materials in loudspeaker enclosures. *Journal of the Audio Engineering Society*, 24(3):162–170, 1976.

[131] Juha Backman. Absorption materials in reflex loudspeakers. In *Audio Engineering Society Convention 140*. Audio Engineering Society, 2016.

[132] John Borwick. *Loudspeaker and headphone handbook*. CRC Press, 2012.

[133] Xin Li, Zhigang Cao, Lijun Xu, and Bilong Liu. Sound absorption of the absorber composed of a shunt loudspeaker and porous materials in tandem. *Polymers*, 15(14):3051, 2023.

[134] Pierre A Deymier. *Acoustic metamaterials and phononic crystals*, volume 173. Springer Science & Business Media, 2013.

[135] N Bert Roozen, Marije Bockholts, Pascal van Eck, and A Hirschberg. Vortex sound in bass-reflex ports of loudspeakers. part i. observation of response to harmonic excitation and remedial measures. *The Journal of the Acoustical Society of America*, 104(4):1914–1918, 1998.

[136] NB Roozen, JEM Vael, and Joris A Nieuwendijk. Reduction of bass-reflex port nonlinearities by optimizing the port geometry. In *Audio Engineering Society Convention 104*. Audio Engineering Society, 1998.

[137] Gioia Fusaro, Luca Barbaresi, Matteo Cingolani, Massimo Garai, Edoardo Ida, Andrea Prato, and Alessandro Schiavi. Investigation of the impact of additive manufacturing techniques on the acoustic performance of a coiled-up resonator. *The Journal of the Acoustical Society of America*, 153(5):2921–2921, 2023.

[138] Don B Keele Jr. Low-frequency loudspeaker assessment by nearfield sound-pressure measurement. *Journal of the audio engineering society*, 22(3):154–162, 1974.

[139] Joe D'Appolito. Measuring loudspeaker low-frequency response. *Audiomatica, Available: http://www. audiomatica. com*, 2018.

[140] Ahmet Selamet, MB Xu, I-J Lee, and Norman T Huff. Helmholtz resonator lined with absorbing material. *The Journal of the Acoustical Society of America*, 117(2):725–733, 2005.

[141] Joris A Nieuwendijk. Band-pass loudspeaker enclosure with a long port. In *Audio Engineering Society Convention 94*. Audio Engineering Society, 1993.

[142] Arthur P Berkhoff. Impedance analysis of subwoofer systems. *Journal of the Audio Engineering Society*, 42(1/2):4–14, 1994.

[143] James Lazar and Glenn S Kubota. Analysis of a vented-box loudspeaker system via the impedance function. In *Audio Engineering Society Convention 147*. Audio Engineering Society, 2019.

[144] Solal Bouchet and Valentin Mouton. Quantifying loudspeakers' power consumption. *Journal of the Audio Engineering Society*, 70(7/8):601–610, 2022.

# Appendix A

# List of Publications

## Journal Papers

**Matteo Cingolani**, Giulia Fratoni, Luca Barbaresi, Dario D'Orazio, Brian Hamilton, and Massimo Garai. A trial acoustic improvement in a lecture hall with MPP sound absorbers and FDTD acoustic simulations. *Applied Sciences*, 11(6), 2445, 2021.
DOI: doi.org/10.3390/app11062445

**Matteo Cingolani**, Gioia Fusaro, Giulia Fratoni, and Massimo Garai. Influence of thermal deformations on sound absorption of three-dimensional printed metamaterials. *The Journal of the Acoustical Society of America*, 151(6):3770– 3779, 2022.
DOI: doi.org/10.1121/10.0011552

Gioia Fusaro, Luca Barbaresi, **Matteo Cingolani**, Massimo Garai, Edoardo Ida, Andrea Prato, and Alessandro Schiavi. Investigation of the impact of additive manufacturing techniques on the acoustic performance of a coiled-up resonator. *The Journal of the Acoustical Society of America*, 153(5):2921–2931, 2023.
DOI: doi.org/10.1121/10.0019474

**Matteo Cingolani**, Domenico De Salvio, Dario D'Orazio, and Massimo Garai. Clustering analysis of noise sources in healthcare facilities. *Applied Acoustics*, 214:109660, 2023.
DOI: doi.org/10.1016/j.apacoust.2023.109660

**Matteo Cingolani**, Vicente Romero Garcia, Dario D'Orazio, and Massimo Garai. Improving the frequency response of a vented-port loudspeaker with acoustic metamaterials. Submitted to *The Journal of the Acoustical Society of America*, 2024.

## Conference Papers

**Matteo Cingolani**, Gioia Fusaro, Massimo Garai, Giulia Fratoni, Dario D'Orazio, and Luca Barbaresi. MPP sound absorbers investigation to optimize a lecture hall speech intelligibility. *In proceeding of 24th International Congress on Acoustics*, volume 3, pages 267-273. Korea, 2022.

Gioia Fusaro, **Matteo Cingolani** , Giulia Fratoni, Massimo Garai, and Luca Barbaresi. Implementazione Multi-fisica FEM per prototipazione di metamateriali acustici. *In Atti AIA (Associazione Italiana Acustica)*, pp. 1-2, 2022.

**Matteo Cingolani**, Gioia Fusaro, and Massimo Garai. The influence of thermo-hygrometric conditions on metamaterials' acoustic performance: an investigation on a 3d printed coiled-up resonator. *In INTER-NOISE and NOISE-CON Congress and Conference Proceedings*, volume 265, pages 3045–3050. Institute of Noise Control Engineering, 2023.
DOI: doi.org/10.3397/IN_2022_0428

Gioia Fusaro, Luca Barbaresi, **Matteo Cingolani**, Massimo Garai, Edoardo Idà, Andrea Prato, and Alessandro Schiavi. Influence of additive manufacturing on acoustic metamaterials performance: a case study, *Forum Acusticum 2023*, 10-14 September 2023, Turin, Italy.

**Matteo Cingolani**, Domenico De Salvio, Dario D'Orazio, and Massimo Garai. Preliminary clustering of noise in a hospital room, *Forum Acusticum 2023*, 10-14 September 2023, Turin, Italy.